

Charles University in Prague  
Faculty of Mathematics and Physics

## DIPLOMA THESIS



Martin Rybář

## **Jets in $pp$ and $PbPb$ collisions at LHC**

Institute of Particle and Nuclear Physics

Supervisor: RNDr. Jiří Dolejší, CSc.

Consultant: Mgr. Martin Spousta, Ph.D.

Study field: Nuclear and Subnuclear Physics

2010



Univerzita Karlova v Praze  
Matematicko-fyzikální fakulta

## DIPLOMOVÁ PRÁCE



Martin Rybář

### Jety v $pp$ a $PbPb$ srážkách na LHC

Ústav částicové a jaderné fyziky

Vedoucí diplomové práce: RNDr. Jiří Dolejší, CSc.

Konzultant: Mgr. Martin Spousta, Ph.D.

Studijní program: Jaderná a subjaderná fyzika

2010



**Acknowledgement:** I would like to thank my supervisor Dr. Jiří Dolejší for his valuable advice, leading of my diploma thesis, encouragement and support, as well as to Martin Spousta who gave me a lot of advice, discussions and introducing me to the ATLAS software. I also thank the members of the ATLAS heavy ion jet subgroup: Brian Cole, Nathan Grau and Aaron Angerami for their suggestions on our group meetings and also all other members of ATLAS heavy ion group. I am also grateful to Alan Watson for his patient discussions and advices about trigger system and Tomáš Kosek for discussions about heavy ion collisions. Last but not least I would like to thank my family, girlfriend Eva for her help with English and friends for their support during my studies.

Prohlašuji, že jsem svou diplomovou práci napsal samostatně a výhradně s použitím citovaných pramenů. Souhlasím se zapůjčováním práce a jejím zveřejňováním.

I declare that I wrote my diploma thesis independently and exclusively with the use of the cited sources. I agree with lending and publishing the thesis.

In Prague, April 15, 2010

Martin Rybář



Název práce: Jety v pp a PbPb srážkách na LHC

Autor: Martin Rybář

Katedra (ústav): Ústav částicové a jaderné fyziky

Vedoucí diplomové práce: RNDr. Jiří Dolejší, CSc.

e-mail vedoucího: dolejsi@ipnp.troja.mff.cuni.cz

Abstrakt: Detektor ATLAS je mnohoúčelový detektor, který je primárně navržen pro proton-protonové srážky. Zajímavé srážky jsou vybírány třístupňovým triggerem. Tato práce předkládá studii využití tohoto systému ve srážkách těžkých iontů. První dvě kapitoly obsahují stručný úvod do fyziky srážek těžkých iontů, především pak se zaměřením na fyziku jetů, obsahují rovněž některé výsledky z experimentu RHIC. V dalších dvou kapitolách je popsán detektor ATLAS a jeho trigrovací systém, opět se zaměřením na jety. Druhá polovina práce pak obsahuje vlastní výsledky. Je zde navrženo několik strategií pro kalorimetrický trigger na první úrovni triggeru a jejich výsledky. Další kapitola je věnována druhému stupni jetového triggeru. Je popsán současný stav jetového algoritmu a algoritmus vyvinutý pro běh v těžkoiontových srážkách. Rovněž jsou ukázány výsledky tohoto algoritmu.

Klíčová slova: srážky těžkých iontů, detektor ATLAS, trigger, jet, kvark-gluonové plasma.

Title: Jets in pp and PbPb collisions at LHC

Author: Martin Rybář

Department: Institute of Particle and Nuclear Physics

Supervisor: RNDr. Jiří Dolejší, CSc.

Supervisor's e-mail address: dolejsi@ipnp.troja.mff.cuni.cz

Abstract: The ATLAS detector is designed primarily for proton-proton collisions, and potentially interesting events are selected by a three-level trigger system. We have studied the performance of the ATLAS trigger system for Pb+Pb collisions. A brief introduction to the heavy ion physics with focus on jets and some results from RHIC experiments are presented in first three chapters. Then we describe the ATLAS detector, its trigger system and three strategies for L1 trigger. We focus on the first level calorimeter trigger and propose modest changes to the default trigger strategy to address specific characteristics of heavy ion collisions at the LHC. Results from performance studies of proposed strategies are presented. We describe current status of L2 jet trigger algorithm designed for p+p collisions. Then we present developed algorithm with background subtraction adapted to heavy ion collisions and its performance.

Keywords: Heavy Ions Collisions, ATLAS detector, Trigger, Jet, Quark-Gluon Plasma.



# Contents

<b>Introduction</b>	<b>3</b>
<b>1 Introduction to Heavy Ion Physics</b>	<b>4</b>
1.1 The Standard Model . . . . .	4
1.2 Basics of Quantum Chromodynamics . . . . .	6
1.3 Quark Gluon Plasma . . . . .	9
1.4 Heavy Ion Collisions . . . . .	12
1.4.1 Space Time Evolution . . . . .	13
1.4.2 Glauber Model . . . . .	17
<b>2 Signatures of QGP</b>	<b>20</b>
2.1 High $p_T$ Suppression . . . . .	20
2.2 Flow . . . . .	21
2.3 Hadron Production Cross Section . . . . .	22
2.4 Electromagnetic Probes . . . . .	23
<b>3 Jets and Jet Quenching</b>	<b>26</b>
3.1 Jets in Hadronic Collision . . . . .	26
3.2 Jets in Detector . . . . .	27
3.2.1 Jet Parameters . . . . .	27
3.2.2 Cone Algorithm . . . . .	29
3.3 Jet Quenching . . . . .	29
<b>4 The ATLAS Detector</b>	<b>34</b>
4.1 Inner Detector . . . . .	35
4.2 Calorimeter System . . . . .	36
4.3 Muon System . . . . .	37
<b>5 The ATLAS Trigger System in Heavy Ion Collisions</b>	<b>38</b>
5.1 Level-1 Trigger . . . . .	39
5.2 The Level-2 Trigger . . . . .	42
5.3 Event Filter . . . . .	43
<b>6 Tuning the L1 calorimeter Trigger System in Simulations for HI Collisions</b>	<b>44</b>
6.1 $e/\gamma$ and $\tau$ /hadron L1 Trigger . . . . .	47

6.2	Forward and Endcap Region . . . . .	48
6.3	Strategy no.1: Centrality-Dependent Thresholds . . . . .	49
6.3.1	L1 Jet Trigger Performance . . . . .	51
6.3.2	Limits for Total $E_T$ . . . . .	54
6.4	Strategy no.2: Background Subtraction . . . . .	56
6.4.1	L1 Jet Trigger Performance . . . . .	57
6.4.2	Forward Region . . . . .	59
6.5	Strategy for the First Heavy Ion Run: Simple Trigger Menu	60
<b>7</b>	<b>Testing the L2 Jet Trigger Algorithm in Simulations</b>	<b>62</b>
7.1	L2 Jet Algorithm for Heavy Ions . . . . .	64
7.2	L2 Jet Trigger Performance . . . . .	65
7.3	Timing Performance of L2 Jet Trigger . . . . .	70
<b>8</b>	<b>Conclusion</b>	<b>73</b>
	<b>References</b>	<b>75</b>
	<b>Appendix A</b>	<b>79</b>
	<b>Appendix B</b>	<b>82</b>
	<b>Appendix C</b>	<b>83</b>

# Introduction

The purpose of heavy-ion physics is to study nuclear matter under extreme conditions in nucleus-nucleus collisions. Quantum Chromodynamics predicts a new phase of matter called quark-gluon plasma where quarks and gluons are deconfined from hadrons. This state of matter probably existed also a few  $\mu\text{s}$  after Big Bang. Thus, relativistic heavy-ion collisions provide the experimental information on the fundamental prediction of the Standard Model. They explore the physics of this new state of matter and give an information about the beginning of our Universe and also about global features of our Universe which are believed to be connected with characteristic properties of this early evolution.

Objectives for heavy ion experiments are to find out what are the properties of matter formed in heavy-ion collision. We expect that the detector ATLAS (and all other LHC experiments) will bring a lot of new information and insight into properties and behaviour of quark-gluon plasma. Although the ATLAS detector is designed primarily for proton-proton collisions it can be well used to study the collisions of heavy ions. This thesis is concerned with the performance of the ATLAS trigger system for Pb+Pb collisions.

First, we give a brief introduction to the heavy ion physics and we present some results from RHIC experiments. Then we describe ATLAS detector and ATLAS trigger system. Finally, several triggering strategies are proposed for ATLAS heavy ion programme and their performance is also illustrated. Thesis is focused mainly on calorimeter trigger, especially jets.

In the whole thesis the system of natural units<sup>1</sup> is used.

---

<sup>1</sup>speed of light  $c = 1$ , Planck constant  $\hbar = 1$

# Chapter 1

## Introduction to Heavy Ion Physics

### 1.1 The Standard Model

The Standard Model (SM), fundamental theory of modern particle physics, is a quantum field theory describing three of the four fundamental interactions: strong, weak and electromagnetic. The last interaction, gravity, is described by Einstein's general relativity and has no generally accepted quantum description. The basic entities of the Standard model are fermions and bosons.

#### Fermions

Fermions are half-integer spin elementary particles that make up all matter, they obey Fermi-Dirac statistics. They are divided into two groups: quarks (q) and leptons (l). There are six flavours (types) of quarks (see table 1.1) and leptons (see table 1.2) and for each quark/lepton there is an anti-particle - anti-quark ( $\bar{u}$ ) and anti-lepton ( $\bar{l}$ ).

particle	mass[GeV/c <sup>2</sup> ]	spin	parity	charge	another quantum numbers
<i>u</i>	0.003	1/2	+1	2/3	$I_3 = 1/2$
<i>d</i>	0,006	1/2	+1	-1/3	$I_3 = 1/2$
<i>s</i>	0,1	1/2	+1	-1/3	$S = -1$
<i>c</i>	1,3	1/2	+1	2/3	$C = 1$
<i>b</i>	4,3	1/2	+1	-1/3	$B = -1$
<i>t</i>	175	1/2	+1	2/3	$T = 1$

Table 1.1: Quarks [1]

particle	mass[MeV/c <sup>2</sup> ]	spin	charge
$e$	0.511	1/2	-1
$\nu_e$	$< 10^{-5}$	1/2	0
$\mu$	106	1/2	-1
$\nu_\mu$	$< 0.2$	1/2	0
$\tau$	1777	1/2	-1
$\nu_{\tau}$	$< 20$	1/2	0

Table 1.2: Leptons [1]

particle	mass[GeV/c <sup>2</sup> ]	spin	parity
$\gamma$	0	1	-1
$W^+, W^-$	80.4	1	$\times$
$Z^0$	91.2	1	$\times$
$g$	0	1	-1

Table 1.3: Intermediate bosons [1]

## Intermediate Bosons

The standard model explains forces between particles through exchange of mediating particles - intermediate bosons. All bosons have integer spin, they obey Bose-Einstein statistic. Three kinds of bosons mediating three different interactions exist, see Table 1.3:

Photons mediate **the electromagnetic interaction** between electrically charged particles. The electromagnetic force is described by quantum electrodynamics (QED).

**The weak nuclear force**, interaction between different flavour particles is mediated by  $W^+$ ,  $W^-$  and  $Z^0$ . It is the only interaction which can change particle flavour and it is in charge of most particle decays, for example  $\beta$ -decay of neutron. In fact, the weak force is unified with the electromagnetic force within the electroweak theory, see [2].

**The strong interaction**, force between color-charged particles (quarks and gluons) is mediated by eight gluons. Gluons, in addition to other gauge bosons, have also a color charge, so they are able to interact with themselves. The strong interaction is described by quantum chromodynamics (QCD). A short introduction to QCD is given in the next section, for details see [7].

The last boson predicted by SM is a massive scalar Higgs boson which has not yet been observed. The role of Higgs boson in SM is explanation of generation of masses. Together with gluons and  $W^+$  Higgs boson is capable of self interaction. More information about Higgs boson can be also found in [2].

The last interaction, gravity, is mediated by a hypothetical particle called

graviton but it has not been successfully incorporated into SM yet.

A schematic overview of fermion and boson interactions is shown in Fig. 1.1.

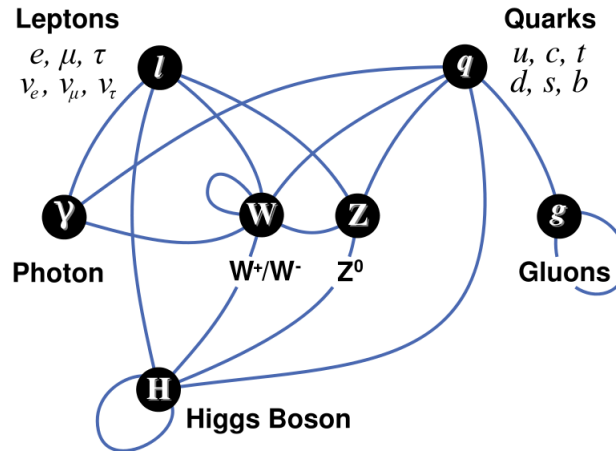


Figure 1.1: Overview of all possible interactions between particles in the SM. Figure taken from [3].

## 1.2 Basics of Quantum Chromodynamics

QCD is a non-abelian gauge quantum field theory of interactions between color-charged fermions and gluons. There are three colours: red, green and blue and "anti-colours" of anti-fermions. There is not similarity to the macroscopic colours, colour is just a new quantum number. The experimental observation that no free quarks and gluons are observed leads to the assumption that only colour neutral particles exist. This extraordinary behaviour of the nature is described inside the QCD theory where the coupling constant  $\alpha_S$  significantly differs compared to electromagnetic coupling. A perturbative approach (pQCD) can not be used in some cases and we have to use the non-perburbative approach, lattice QCD for example, which describes space as a set of discrete points and solve problems numerically on computers. QCD has two main peculiar properties:

- **Asymptotic freedom** is a specific property of QCD related to the dependence of the "interaction strength" on the momentum transfer. This property is usually expressed in term of so called *running* strong coupling "constant" which depends on transferred momentum  $Q^2$  [7] as follows:

$$\alpha_S(Q^2) = \frac{\alpha_S(\mu^2)}{1 + \alpha_S(\mu^2) \frac{33-2n_f}{12\pi} \ln(-\frac{Q^2}{\mu^2})}, \quad (1.1)$$

$$\alpha_S(Q^2 \rightarrow 0) \rightarrow 0, \quad (1.2)$$

where  $n_f$  is the number of flavours,  $\mu^2$  is renormalization scale. Dependence of the coupling constant on the momentum transfer from measurement is shown in Fig. 1.2.

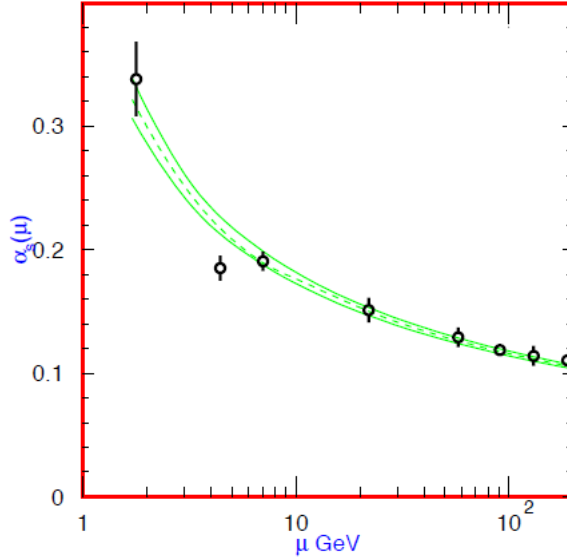


Figure 1.2: Summary of values of  $\alpha_S$  from  $e^+e^-$  measurements as a function of  $\mu = \sqrt{\mu^2} \equiv \sqrt{Q^2}$ . Figure taken from [1].

The formula 1.1 can be rewritten as:

$$\alpha_S(Q^2) \approx \frac{12\pi}{(33 - 2N_f) \ln \frac{Q^2}{\Lambda^2}}, \quad (1.3)$$

where  $\Lambda \approx 200$  MeV is the momentum scale at which the QCD coupling constant is infinite and where the perturbation calculation is clearly meaningless. For a high- $Q^2$  process<sup>1</sup> (above 2-3 GeV), the coupling constant becomes small enough for a pQCD framework. Formulas 1.1 and 1.3 are valid in next-to-leading order calculation (NLO).

- **Confinement** means that the force between quarks does not vanish during their separation (it would take an infinite amount of energy), only colour neutral objects exist. Quarks and gluons are confined in composite particles called hadrons<sup>2</sup>. This effect is due to the gluons self interaction and it is illustrated in Fig. 1.3 with phenomenological potential of strong interaction obtained by lattice calculation [5]:

$$V_S(r) = -\frac{4}{3} \frac{\alpha_S}{r} + kr, \quad (1.4)$$

<sup>1</sup>hard QCD process

<sup>2</sup>Baryons (proton, neutron, hyperons) consist of three quarks of different colours and mesons (pions, kaons,...) consist of quark anti-quark pair

where the first part is similar to Coulomb potential and dominates at small distances  $r$ , the second term, where  $k \approx 1\text{GeV}/\text{fm}$  is the color string tension, dominates at large distance and it is responsible for confinement. When trying to separate quarks, the energy of color field between them grows up and new quark anti-quark pair is created when it is energetically more favourable.

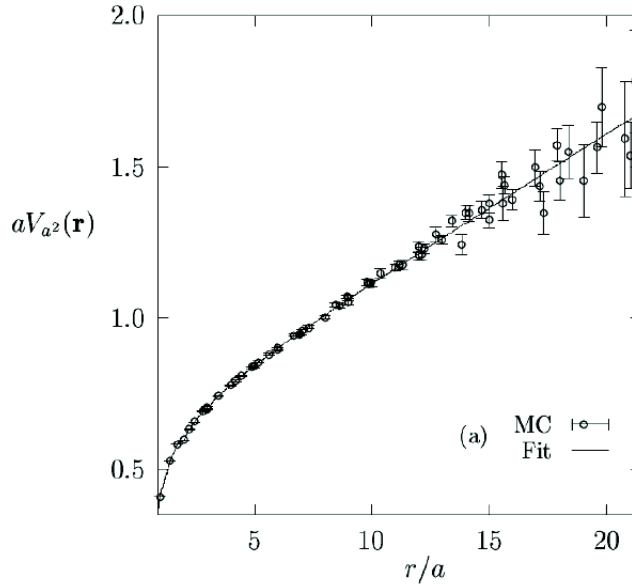


Figure 1.3: The QCD potential as a function of distance between quarks obtained by lattice QCD,  $a$  is a lattice constant (i.e. distance between lattice points). Figure taken from [4].

The dynamics of the quarks and gluons are controlled by the QCD Lagrangian [7]

$$\mathcal{L} = \bar{\psi}_f [i\gamma^\mu \partial_\mu - m_f] \psi_f - \frac{1}{4} F_a^{\mu\nu} F_{\mu\nu}^a, \quad (1.5)$$

where  $\psi_f$  represents bispinor of quark flavour  $f$  and the field strength tensor  $F_{\mu\nu}^A$  is defined as:

$$F_{\mu\nu}^a = \partial_\mu A_\nu^a - \partial_\nu A_\mu^a - \sqrt{4\pi\alpha_S} f^{abc} A_\mu^b A_\nu^c, \quad (1.6)$$

where  $A_\mu^a$  is one of eight ( $a, b, c = 1..8$ ) vector gluon fields,  $f^{abc}$  are structure constants of the  $SU(3)$  symmetry group. If we use the standard quantum field theory framework, the Feynman diagrams, the Lagrangian 1.5 gives us three basic diagrams, see Fig. 1.4. The first one shows emission or absorption of a gluon, the next two show three and four gluons interactions which are present in QCD in contrast to QED, where only the first kind of interaction is possible, because photons have no charge. An introduction to QCD is presented in lecture notes [7].

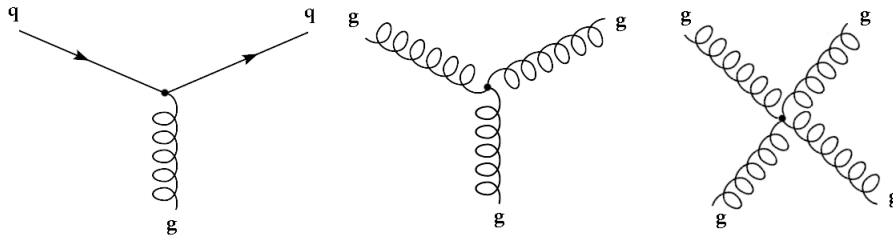


Figure 1.4: Basic Feynman diagram of QCD. Figure taken from [6].

### 1.3 Quark Gluon Plasma

In contrast to confinement, QCD also predicts a phase of matter, where quarks are not confined inside hadrons. It is only necessary to use the finite temperature field theory (for an introduction see e.g. [8]) to describe the system of interacting quarks and gluons. This is the new state of matter - **Quark Gluon Plasma**. Equation 1.4 can be rewritten according to lattice simulations to

$$V_S(r, T) = -\frac{4}{3} \frac{\alpha_S}{r} e\left(-\frac{r}{\lambda_D(T)}\right) + k(T)r, \quad (1.7)$$

where parameter  $k$  now depends on temperature  $T$ . The second confining term ( $k(T)r$ ) vanishes above temperature  $T_c \approx 150 - 170$  GeV. An exponential dependence appears in the first term and it has the similar role as Debye charge screening effect ( $\lambda_D$  is Debye screening length,  $\lambda_D \sim 1/T$ ) in ordinary plasma physics: The Coulomb potential of two charges changes significantly if these charges are placed to an environment which contains charges of both signs  $\equiv$  plasma.

According to the Big Bang theory which describes development of our Universe from an exploding initial singularity, this state of matter also existed a few  $\mu s$  after the Big Bang. As Universe expanded and cooled down, it evolved through several phase transitions, one of them being transition into QGP and later the transition of QGP to hadrons.

The idea of deconfinement is presented in Fig. 1.5, where the transition into QGP is presented as a compression of hadronic matter by increasing temperature, pressure or by adding more hadrons into fixed volume. After phase transition, quarks are not longer confined inside hadrons but they are still confined inside the volume of QGP.

There are several possibilities how to describe this transition: thermodynamics and statistical physics, lattice QCD, string theory or AdS/CFT.

We will follow some calculation with simple phenomenological MIT bag model taken from [11][12][13]. This model can describe some basic features of QGP: energy density and pressure are calculated by using partition function. This model describe QGP as an ideal gas with an outside vacuum pressure

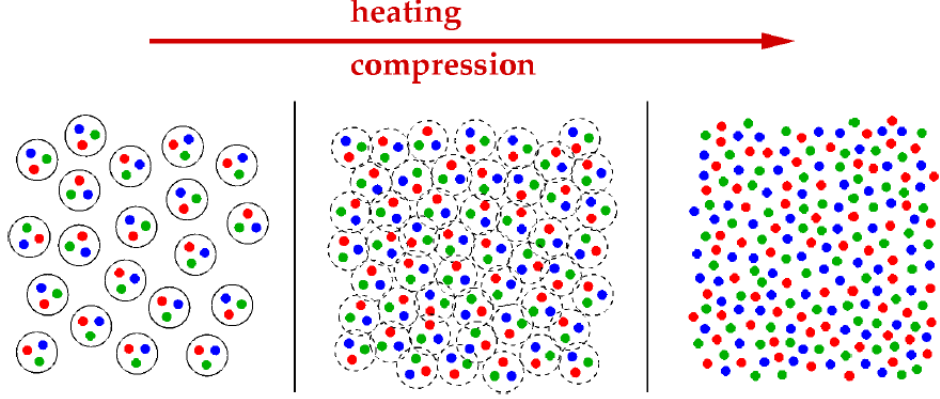


Figure 1.5: Transition from hadron matter into QGP. Figure taken from [9].

bag constant  $B$ . Gluon energy density can be calculated using boson momentum distribution:

$$\epsilon_g = \frac{4\pi d_g}{(2\pi)^3} \int p^3 \frac{1}{e^{\frac{p}{T}} - 1} dp = \frac{d_g \pi^2 T^4}{30}, \quad (1.8)$$

where  $d_g$  is the gluon number of degrees of freedom given by

$$d_g = 2(\text{helicity}) \times 8(\text{colours}) = 16. \quad (1.9)$$

The energy density of quarks and anti-quarks can be written similarly with Fermi-Dirac statistics as

$$\epsilon_{\bar{q}} = \frac{4\pi d_{\bar{q}}}{(2\pi)^3} \int p^3 \frac{1}{e^{\frac{p+\mu}{T}} + 1} dp \quad (1.10)$$

The energy density of quarks (minus sign) with Fermi-Dirac statistics can not be solved analytically. However, the formula for anti-quark energy density differs with opposite sign of chemical potential can be solved analytically. The total energy density of quarks and anti-quarks can be calculated and it is given by

$$\epsilon_{\bar{q}} + \epsilon_q = d_q \left( \frac{7\pi^2 T^4}{120} + \frac{\mu^2 T^2}{4} + \frac{\mu^4}{8\pi^2} \right), \quad (1.11)$$

where  $\mu$  is the chemical potential and  $d_q$  is the number of degrees of freedom for quarks which is for two flavours given by

$$d_{quark} = 2(\text{spin}) \times 3(\text{colours}) \times 2(\text{flavours}) = 12. \quad (1.12)$$

If we consider bag pressure  $B$ , the total energy density of the QGP becomes

$$\epsilon_{QGP} = 37 \frac{\pi^2}{30} T^4 + 3\mu^2 T^2 + \frac{3}{2\pi^2} \mu^4 + B. \quad (1.13)$$

The energy density of ordinary hadronic matter (HM) can be calculated by the same way in a hot pion gas approach.

$$\epsilon_{HM} = d_{pions} \frac{\pi^2}{30} T^4 = \frac{\pi^2}{10} T^4, \quad (1.14)$$

where  $d_{pions} = 3$  is the number of isospin degrees of freedom of pions.

We can derive formulae for pressure of QGP and hadronic matter by the similar way

$$P_{QGP} = 37 \frac{\pi^2}{90} T^4 + \mu^2 T^2 + \frac{1}{2\pi^2} \mu^4 - B, \quad (1.15)$$

$$P_{HM} = d_{pions} \frac{\pi^2}{90} T^4 = \frac{\pi^2}{30} T^4. \quad (1.16)$$

The transition should occur when the pressure of the hadronic phase is equal to pressure of the QGP phase.

Now we can describe two extreme situations:

1. Baryon-free QGP - the chemical potential will be zero which means that the number of quarks is equal to the number of anti-quarks. We can calculate bag constant from the QCD scale parameter:  $\Lambda_{QCD} \approx B^{1/4} \approx 217 \text{ MeV}/c$  [14] the critical temperature  $T_C$

$$T_C = \left( \frac{90B}{34\pi^2} \right)^{\frac{1}{4}} \approx 160 \text{ MeV}. \quad (1.17)$$

and density for the QGP  $\epsilon_{QGP} \approx 1.6 \text{ GeV}/\text{fm}^3$ .

2. Baryonic QGP at zero temperature and finite chemical potential and the energy density and pressure can be again derived. The critical chemical potential  $\mu_C$  is given by

$$\mu_C = \left( \frac{24\pi^2}{d_q} \right)^{1/4} \quad (1.18)$$

which leads to the critical baryon number density

$$n_C = \frac{d_q \mu_C^2}{6\pi^2} = 0.72/\text{fm}^3 \quad (1.19)$$

which is approximately five times more than density of normal nuclear matter.

Fig. 1.6 shows lattice QCD calculation of energy density and one can see sharp rise of the energy density at a critical temperature  $T_c \approx 170 \text{ GeV}$ . This can be interpreted as the phase transition into QGP. There is also shown the massless non-interacting quarks approach - Stefan-Boltzmann limit. This limit is not reached and it indicates that this description may not be applicable at these temperatures, the system is not ideal gas and there are still significant interactions among QGP constituents.

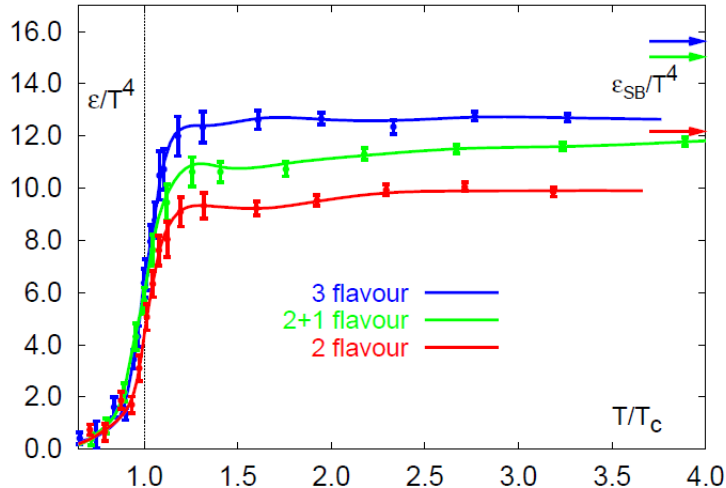


Figure 1.6: The energy density in QCD from lattice calculation as a function of the temperature scaled by the  $T_C$ . The arrows on the top left corner indicate Stefan-Boltzmann limit. Figure taken from [15].

Fig. 1.7 shows a QCD phase diagram based on lattice QCD (lQCD) calculations and it is clear that there are two ways how to reach phase transition into QGP - by raising temperature or chemical potential (cold QGP). It seems that the cold QGP exists in neutron stars and the transition into QGP by raising temperature can be reached in heavy ion collisions.

## 1.4 Heavy Ion Collisions

One of the methods how to create extremely hot and dense matter for QCD transition from ordinary hadronic matter into QGP is the method of collisions of heavy ions. Heavy ions are used because many of constituent nucleons collide at the same time and large interaction region is created.

Fig. 1.8 presents an illustration of the heavy ion collision. We can imagine heavy ion collision as two pancakes<sup>3</sup> of nuclear matter passing through each other with impact parameter  $b$  which is the transverse distance between centres of colliding nuclei, see Fig. 1.8. Small impact parameters correspond to central collisions and large impact parameters to peripheral collisions. It is clear that direct measurement of impact parameter  $b$  is practically impossible, thus several methods based on the particle multiplicity of events were developed.

Constituent nucleons of the nucleus can be divided into two groups, the first group called participants interacts strongly and creates a high density

---

<sup>3</sup>The longitudinal length in the motion direction becomes less than 1 fm because of significant Lorentz contraction.

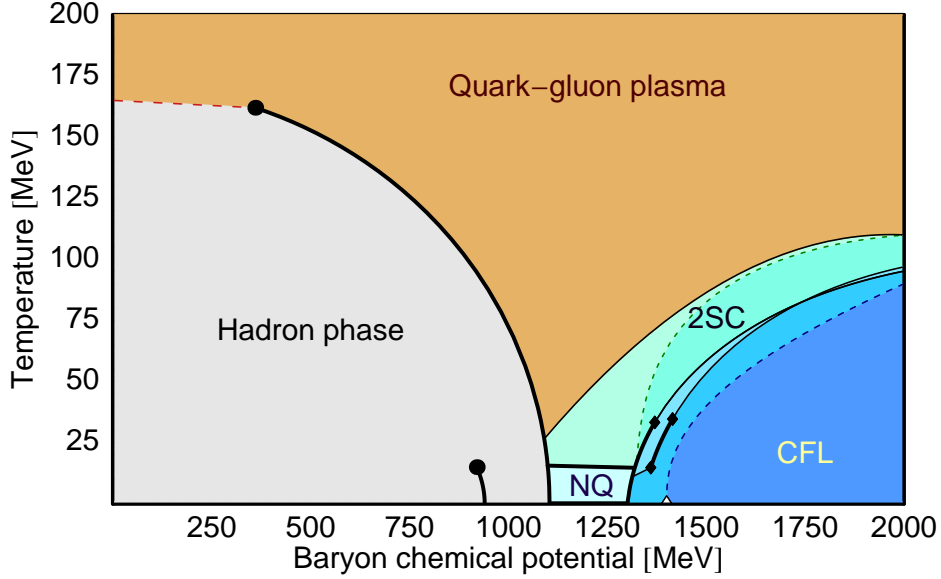


Figure 1.7: QCD phase diagram. Figure taken from [10].

volume - fireball. Members of the second group are called spectators. Spectators remain almost unaffected by the collision.

Geometric parameters of nucleus-nucleus collision can be calculated by the Glauber model, which is described in section 1.4.2.

### 1.4.1 Space Time Evolution

Heavy ion collision is a complicated process which is difficult to describe because various phases are expected to exist from initial collision to final hadron matter. The space time evolution of heavy ion collision was first described by Bjorken [16]. This Bjorken's evolution model of the matter created in HI collisions with values of some variables is shown in Fig. 1.9.

Two nucleus collide at time  $t = 0$  and longitudinal position  $z = 0$  and free partons, mainly gluons, are produced. This system is not in a thermal equilibrium and the dynamics can be described by series of colliding partons which leads finally to local equilibrium. If the critical energy density is reached, the QGP might be formed at proper time  $\tau_0$ . Due to the expansion the system cools down. The system is evolving like a perfect fluid from this time and dynamics of interesting variables such as energy density, pressure, entropy and temperature can be described in hydrodynamics by equations of motion [19]

$$\frac{\partial \epsilon}{\partial \tau} + \frac{\epsilon + p}{\tau} = 0 \quad (1.20)$$

following from the energy momentum conservation of the perfect fluid

$$\frac{\delta T_{\mu\nu}}{\delta x_\mu} = 0, \quad (1.21)$$

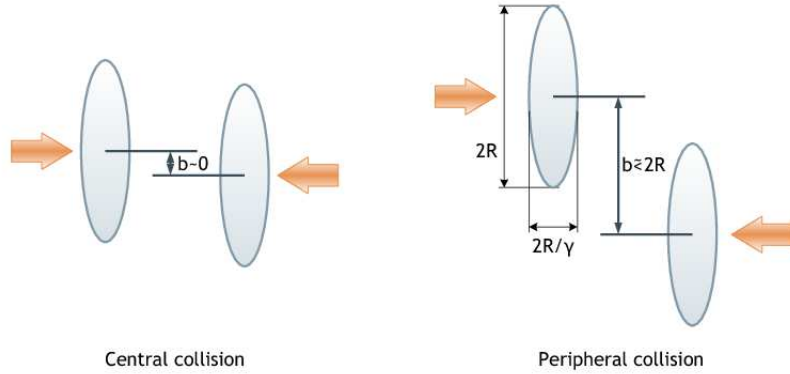


Figure 1.8: Geometry of heavy ion collision.

where  $T_{\mu\nu}$  is the energy-momentum tensor given by

$$T_{\mu\nu} = (\epsilon + p)u_\mu u_\nu - g_{\mu\nu}p, \quad (1.22)$$

where  $g_{\mu\nu}$  is the metric tensor and  $u_\mu$  is the four velocity.

At  $\tau_C$  the system reaches a critical temperature  $T_C$  and quarks recombine into hadrons. Between  $\tau_C$  and  $\tau_H$  there is a coexistence of two phases and after  $\tau_H$  the system consists of interacting hadrons. Final step, called freeze out, takes place at  $\tau_F$  when hadrons stop to interact and produced particles move away.

There are two basic classes of models aiming to describe HI collisions:

## Microscopic models

These models are based on superposition of elementary processes - nucleon-nucleon collisions. They use additional condition and phenomenological interaction to affect the effect of heavy ion collision. But they do not take into account the phase transition into QGP and only particular signatures of QGP are incorporated as free parameters. For example MC simulator HIJING [17][18] is based on superposition of PYTHIA events and additional free parameters such as the mean free path and energy loss  $dE/dx$  that are used for simulation of hot and cold matter effects and jet quenching (see section 3.3) for example. The description of one microscopic model which can estimate some basic properties of HI collisions is described in section 1.4.2.

## Hydrodynamical models

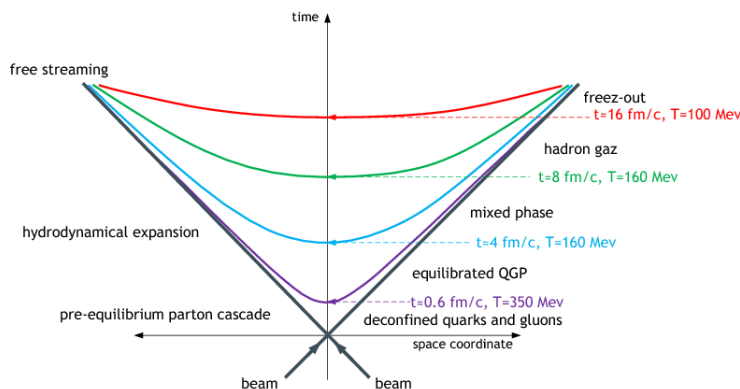


Figure 1.9: Space-time picture of a nucleus-nucleus collision. Hyperbola shows constant proper time  $\tau = \frac{t}{\gamma} = \sqrt{t^2 - z^2}$  and also temperatures. Energy and entropy density are also constant on hyperbola.

According to these models the system in thermal equilibrium would be described as an ideal fluid. In hydrodynamical models the energy, momentum, entropy and baryon number are conserved in the solution of equations of state.

Two simple models are introduced here. Fermi-Landau model is different from Bjorken model in the amount of stopping of the participants in the collision area. The amount of stopping is equivalent to loss of kinetic energy in a collision and it is defined in [33] as

$$\langle \delta y \rangle = |y_b - \langle y \rangle|, \quad (1.23)$$

where  $\delta y$  is average rapidity loss,  $y_b$  is a beam rapidity and  $\langle y \rangle$  is in [34] defined as

$$\langle y \rangle = \frac{2}{N_{part}} \int_0^{y_b} y \frac{dN_{B-\bar{B}}}{dy} dy, \quad (1.24)$$

where  $y$  is a baryon rapidity,  $N_{B-\bar{B}}$  is called net-baryon number defined as  $N_{B-\bar{B}} = N_B - N_{\bar{B}}$  and  $N_{part}$  is the number of participants. The measurement of average rapidity loss is shown in Fig. 1.10 and one can see that a linear behaviour is broken at RHIC energies.

- **Fermi-Landau model** was proposed by Landau in [20]. In this model, nuclei are completely stopped and all their kinetic energy is deposited in the fireball. Material in fireball can be considered as an ideal fluid that expands adiabatically. This description might be appropriate in the case of a large baryon density  $\mu$  and low temperatures such as in neutron stars for example.

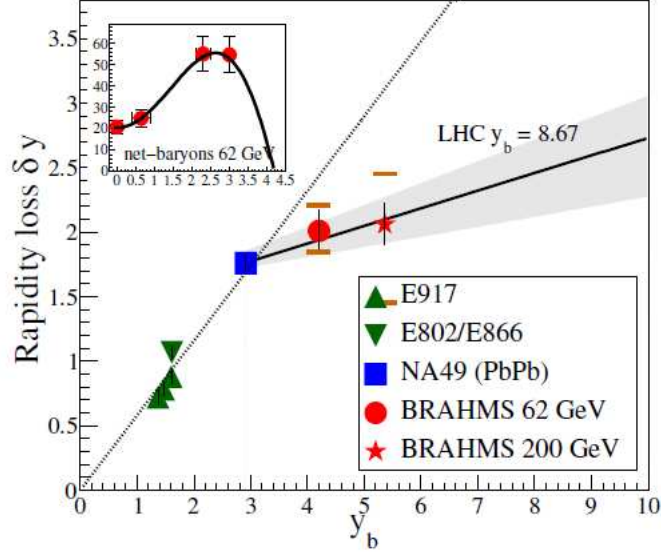


Figure 1.10: Average rapidity loss from AGS, SPS and RHIC as a function of beam rapidity. Figure taken from [35].

- **Bjorken model** proposed by Bjorken in [16] is based on partial transparency of nuclei. Stopping is limited, nuclei pass through each other and nucleons in overlap region might undergo several collisions. At very high energies (above 100 GeV per nucleon) the nucleons have still a lot of energy and move away from the collision region where they leave a highly excited colour field which is then available for production of new particles. If we describe this region (see Fig. 1.11) as cylinder (we can neglect transverse expansion) with an area  $S$  as thickness  $z$  at the formation time  $t = \tau_0 \approx 1\text{fm}/c$  we can estimate energy density  $\epsilon_B$  in this region [16]:

$$\epsilon_B = \lim_{\Delta z \rightarrow 0} \frac{E}{S \Delta z}. \quad (1.25)$$

Next, we consider similar relation for rapidity as in formula (13) in Appendix A derived in [40] and its derivative with respect to  $z$  with using relations for  $t$  and  $z$  analogical to formulas (18) and (15) in Appendix A

$$y = \frac{1}{2} \ln \left( \frac{t+z}{t-z} \right), \quad (1.26)$$

$$t = \tau \cosh y, \quad (1.27)$$

$$z = \tau \sinh y, \quad (1.28)$$

$$\frac{dy}{dz} = \frac{\cosh y}{\tau}, \quad (1.29)$$

where  $y$  is rapidity defined in Appendix A. After that, we can rewrite

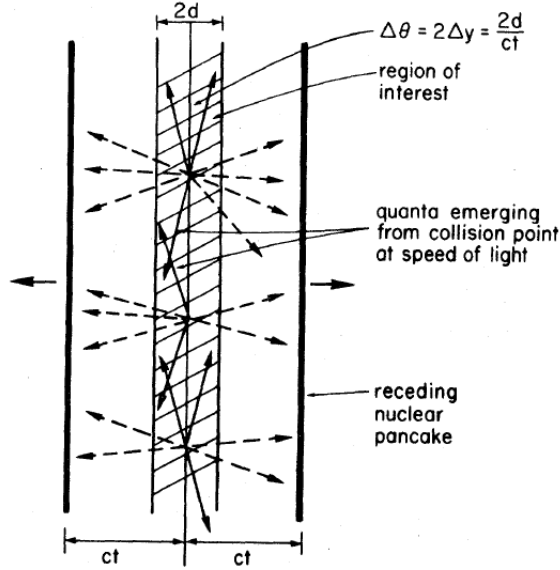


Figure 1.11: Geometry of the initial state in heavy ion collisions. Figure taken from [16].

formula (1.25) according [40] into

$$\epsilon_B = \frac{N}{S} \frac{d\langle E \rangle}{dy} \frac{dy}{dz} \Big|_{y=0} = \frac{N}{S} \frac{d\langle E \rangle}{dy} \frac{\cosh y}{\tau} \Big|_{y=0} = \frac{1}{\tau \pi r_0^2 N^{2/3}} \frac{dE_T}{dy} \Big|_{y=0} \quad (1.30)$$

where  $E_T$  is total transversal energy,  $\langle E \rangle$  is mean energy per nucleon and in the last term we express  $S$  with nuclear radius  $r$

$$r = r_0 N^{1/3} \quad (1.31)$$

with  $r_0 = 1.18$  fm. If we use concrete values  $\tau = \tau_0 = 1$  fm, the energy density at RHIC Au+Au experiment at  $\sqrt{s_{NN}} = 200$  GeV/nucleon is estimated to be  $\sim 5$  GeV/fm<sup>3</sup>. But this value is only approximative because this model is too simple. However, it can still provide basic control between experiment and theoretical predictions.

## 1.4.2 Glauber Model

This simple model of collisions of two nuclei, first proposed by R. J. Glauber in 1955 [21], is well described in [19] and in [22]. It assumes that inelastic collisions of two nuclei A and B (number of nucleons in nuclei is  $A$  and  $B$ ) can be described as superposition of an equivalent number of nucleon-nucleon collisions with the same inelastic cross section  $\sigma_{NN}^{in}$  as in vacuum. It is based only on a geometrical picture of the collision and nucleons are moving on straight lines which is a good approximation for high energies. However, a lot of variables such as cross section and event multiplicity can be calculated

in Glauber model and thus it provides basic description of many features of heavy ion collisions.

We usually use Wood-Saxon nucleons distribution

$$\rho(R) = \rho_0 \frac{1}{1 + e^{(r-R)/a}} \quad (1.32)$$

where  $r$  is nucleus radius defined by formula (1.31) and  $a \approx 0.5$  fm is surface diffuseness parameter. Now, we can define thickness function  $T_A$  which is the nuclear profile function in the plane perpendicular to the beam axis  $z$ .

$$T_A(\mathbf{b}_A) = \int_{-\infty}^{\infty} \rho(\mathbf{b}_A, z) dz \quad (1.33)$$

with normalisation

$$\int_{-\infty}^{\infty} T_A(\mathbf{b}_A) d\mathbf{b}_A = 1 \quad (1.34)$$

Then the probability of a nucleon-nucleon collision between the nuclei A and B at impact parameter  $\mathbf{b}$  is expressed by formula

$$T_{AB}(\mathbf{b})\sigma_{NN} = \int_{-\infty}^{\infty} \int_{-\infty}^{\infty} T_A(\mathbf{b}_A) T_B(\mathbf{b}_B) t(\mathbf{b} - \mathbf{b}_A - \mathbf{b}_B) \sigma_{NN} d\mathbf{b}_A d\mathbf{b}_B \quad (1.35)$$

which define the nuclear overlap function  $T_{AB}(\mathbf{b})$  and where  $t(\mathbf{b})$  is baryon-baryon thickness function, thus  $\sigma_{NN} t(\mathbf{b}) d\mathbf{b}$  is the probability for having the nucleon-nucleon collision within the transverse element  $d\mathbf{b}$ . If we neglect nucleon structure and we use delta function instead of  $t(\mathbf{b})$  we can rewrite formula 1.35 into

$$T_{AB}(\mathbf{b})\sigma_{NN} = \int_{-\infty}^{\infty} T_A(\mathbf{b}') T_B(\mathbf{b} - \mathbf{b}') \sigma_{NN} d\mathbf{b}'. \quad (1.36)$$

There can be maximal  $A \times B$  collisions and occurrence probability of  $n$  collisions is given by [22]

$$P(n, \mathbf{b}) = \binom{AB}{n} (T_{AB}(\mathbf{b})\sigma_{NN})^n (1 - T_{AB}(\mathbf{b})\sigma_{NN})^{AB-n} = \binom{AB}{n} (1-s)^n s^{AB-n}, \quad (1.37)$$

where  $s$  is defined as

$$s = 1 - T_{AB}(\mathbf{b})\sigma_{NN}. \quad (1.38)$$

Now, we can estimate the total probability for having at least one nucleon-nucleon collision in the A+B collision at an impact parameter  $\mathbf{b}$

$$\frac{d\sigma_{AB}}{d\mathbf{b}} = \sum_{n=1}^{AB} P(n, \mathbf{b}) = 1 - s^{AB} = 1 - (1 - T_{AB}(\mathbf{b})\sigma_{NN})^{AB} \quad (1.39)$$

The total inelastic cross section  $\sigma_{AB}$  can be then written as

$$\sigma_{AB} = \int_{-\infty}^{\infty} [1 - (1 - T_{AB}(\mathbf{b})\sigma_{NN})^{AB}] d\mathbf{b} \quad (1.40)$$

If we consider a collision of hadron ( $B = 1$ ) with heavy nucleus ( $A \gg B$ ), the relation for the total cross section can be rewritten as

$$\sigma_{Ah} = \int_{-\infty}^{\infty} \{1 - \exp[AT_B(\mathbf{b})\sigma_{NN}]\} d\mathbf{b} \quad (1.41)$$

The average number of inelastic nucleon-nucleon collisions can be also estimated

$$N_{coll}(\mathbf{b}) = \sum_{n=1}^{AB} nP(n, \mathbf{b}) = ABT_{AB}(\mathbf{b})\sigma_{NN}. \quad (1.42)$$

# Chapter 2

## Signatures of QGP

Properties of QGP, i.e. distributions of quarks and gluons are not directly measurable, one should look for measurable observables, based on observable particles. There are several observables which are sensitive to the collision dynamics. However, an explanation of these observables is difficult and disputable. It should be mentioned that heavy ion collisions need to be compared to p+p and p+A collisions as the reference for medium effects.

This chapter briefly discusses several observables that are expected to be measured at LHC. Some results from RHIC experiment are also shown. Jet quenching effect with brief overview to the jet physics is introduced in the next chapter *Jets and Jet Quenching*.

### 2.1 High $p_T$ Suppression

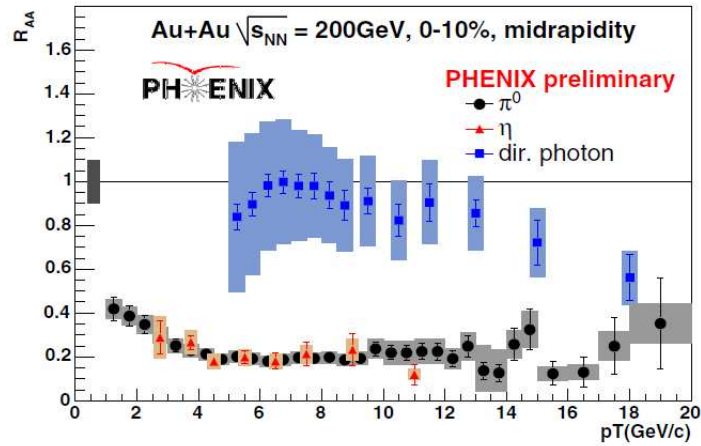


Figure 2.1: Nuclear modification factor for  $\pi^0$ ,  $\eta$ -mesons and direct photons in the most central Au+Au collisions at  $\sqrt{s_{NN}} = 200$  GeV from PHENIX experiment. Figure taken from [23].

Measured hadron spectra, especially protons, antiprotons, pions and kaons

are strongly influenced by interactions in a medium. High  $p_T$  suppression of hadrons might be caused by interacting partons with a medium by the gluon "bremsstrahlung". These partons later fragment into hadrons.

This effect is usually described by nuclear modification factor  $R_{AA}$  which is defined as

$$R_{AA} \equiv \frac{\frac{d^2 N^{AA}}{dp_T d\eta}}{N_{coll} \frac{d^2 N^{pp}}{dp_T d\eta}}. \quad (2.1)$$

It expresses a particle production of nucleus-nucleus collisions relative to p+p collisions. An example of a particle spectra affection is illustrated in Fig. 2.1, where the  $R_{AuAu}$  for direct photons, neutral pions and  $\eta$ -mesons from measurement at PHENIX experiment is shown. One can see a strong suppression of neutral pions and  $\eta$ -mesons and no suppression of direct photons which interact only electromagnetically. This is the signature of strongly interaction of the medium.

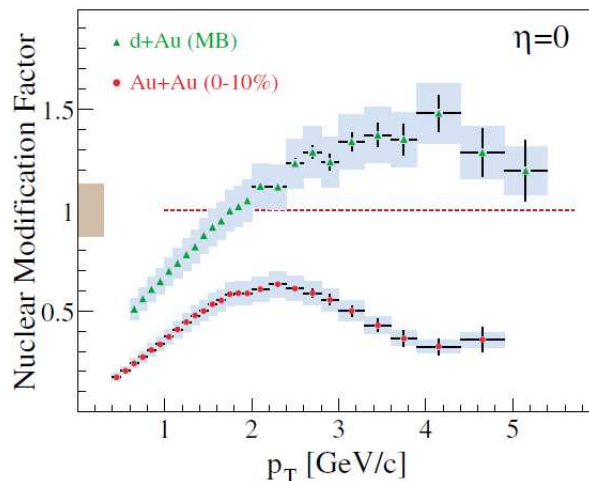


Figure 2.2: Nuclear modification factor in d+Au collisions at  $\sqrt{s_{NN}} = 200$  GeV compared to the nuclear modification factor in the most central Au+Au collisions, BRAHMS experiment. Figure taken from [24].

Another interesting  $p_T$  spectrum from experiment BRAHMS [24] is shown in Fig. 2.2 where high  $p_T$  spectra in d+Au and Au+Au collisions are compared. It is evident that there is a significant suppression in Au+Au collisions while d+Au collisions are not suppressed which is in agreement with our expectation.

## 2.2 Flow

The hydrodynamical models and equations of state can be studied through a group of effects called flow. Flow occurs more markedly in peripheral col-

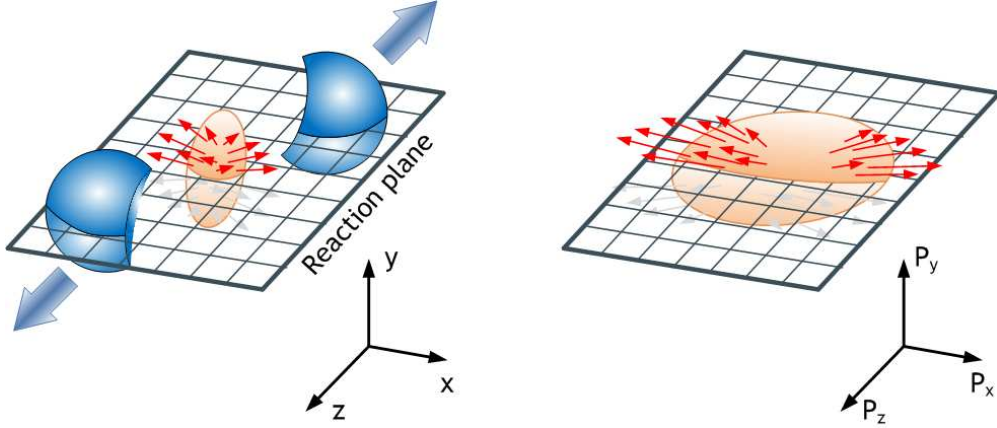


Figure 2.3: Illustration of the origin of the elliptic flow and a reaction plane definition. *Left*: geometric asymmetry of the reaction zone in peripheral collisions. *Right*: momentum anisotropy.

lisions as a consequence of asymmetry of the reaction zone and collective motions of particles in this area, see left Fig. 2.3. This initial geometric asymmetry generates pressure gradients which then generate flow, see right Fig. 2.3.

The flow is usually quantified by Fourier harmonic coefficients  $v_n$  as [26]

$$E \frac{d^3N}{dp^3} = \frac{1}{2\pi} \frac{d^2N}{p_T dp_T dy} \left( 1 + \sum_{n=1}^{\infty} 2v_n \cos[n(\phi - \Psi_r)] \right) \quad (2.2)$$

where  $\Psi_r$  is the azimuthal angle of the reaction plane defined in the left panel of Fig. 2.3 and  $\phi$  is an azimuthal angle from this plane. The first harmonic  $v_1$  is called directed flow and the largest observed harmonic is the second one  $v_2$ , called elliptic flow [26]

$$v_2 = \langle \cos[4(\phi - \Psi_r)] \rangle \quad (2.3)$$

Measured elliptic flow at RHIC experiment compared with hydrodynamical calculations is shown in Fig. 2.4. Figure 2.5 presents an elliptic flow scaled with the number of quarks.

## 2.3 Hadron Production Cross Section

Existence of QGP can be disclosed by increased production of strange hadrons or suppression of  $J/\Psi$  (bound state of  $c\bar{c}$ ) and other quarkonia state.  $J/\Psi$  are primarily produced in hard parton-parton scattering due to its large weight (see table 1.1). Its number might be reduced due to the Debye screening demonstrated in the formula 1.7, the strength between  $c$  and  $\bar{c}$  is reduced and probability for a bound state decreases. We can use quarkonia spectra as thermometer of the medium because the suppression of production different

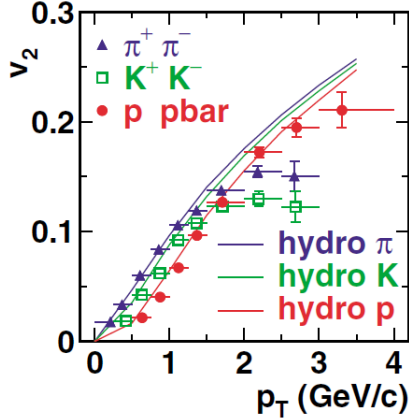


Figure 2.4: Transverse momentum dependence of  $v_2$  for various kinds of particles compared with hydrodynamical calculations. Figure taken from [25].

quarkonia state occurs if size of quarkonia is greater than color screening length which depends on temperature  $\Rightarrow$  different quarkonia states disassociate at different plasma temperatures, see Fig. 2.6.

Measurements of  $J/\Psi$  suppression from SPS experiment are shown in the left panel of Fig. 2.7 as an example. Comparison with effect in normal nuclear matter is also presented.

Another observable is ratio of  $K^+/\pi^+$  and  $K^-/\pi^-$  (or another strange hadron such as  $\Lambda$  or  $\Omega^-$  instead of  $K$ ). A production of strange hadrons<sup>1</sup> is significantly influenced in QGP by gluon fusion process  $gg \rightarrow s\bar{s}$ . This process with relatively small mass of  $s$  quark leads to an increased abundance of strange hadrons which can be seen in the right panel of Fig. 2.7.

## 2.4 Electromagnetic Probes

Electromagnetic probes include dileptons and direct<sup>2</sup> photons measurement. Advantage of electromagnetic probes is that they do not interact strongly and thus they are almost unaffected by the medium. This confirms Fig. 2.1 where a nuclear modification factor for direct photons is shown. Photons are emitted from the fireball during all stages of the collision so they provide a direct measurement of the medium properties.

There are three dominant processes of direct photons production described in NLO pQCD: quark-antiquark annihilation  $q+\bar{q} \rightarrow \gamma+g$ , Compton scattering  $g+q \rightarrow \gamma+q$  and bremsstrahlung  $q+g \rightarrow q+g+\gamma$ . More information can be found in [31]. Dileptons are mainly produced in Drell-Yan processes  $q+\bar{q} \rightarrow l^+ + l^-$ . More information can be found in [32].

<sup>1</sup>Hadrons containing strange quark  $s$  or  $\bar{s}$

<sup>2</sup>Photons not originating from  $\pi^0$  and  $\eta$  decays

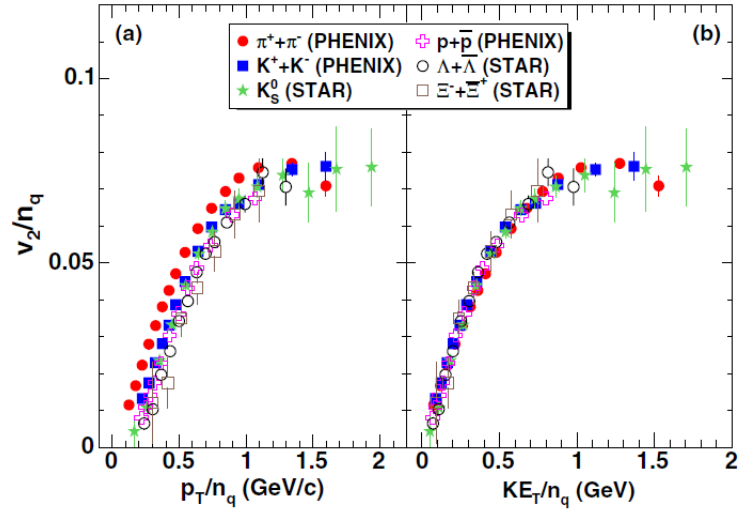


Figure 2.5: Elliptic flow scaled by the number of quarks  $n_q$  as a function of  $p_T$  (left) and  $KE_T = m_T - m$  (right) for several particle species obtained in minimum-bias Au+Au collisions. Figure taken from [27].

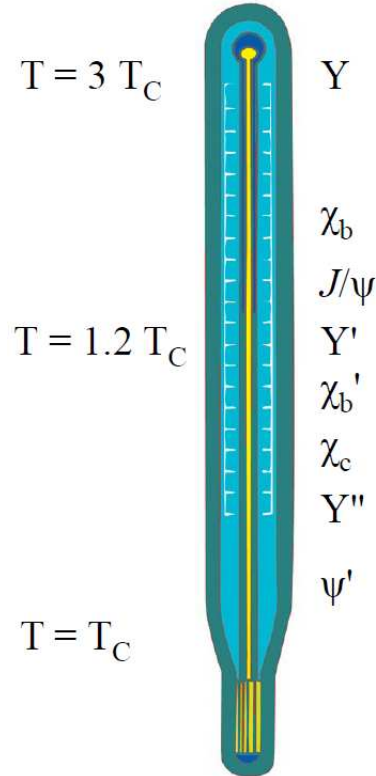


Figure 2.6: Quarkonia as a thermometer for QGP.

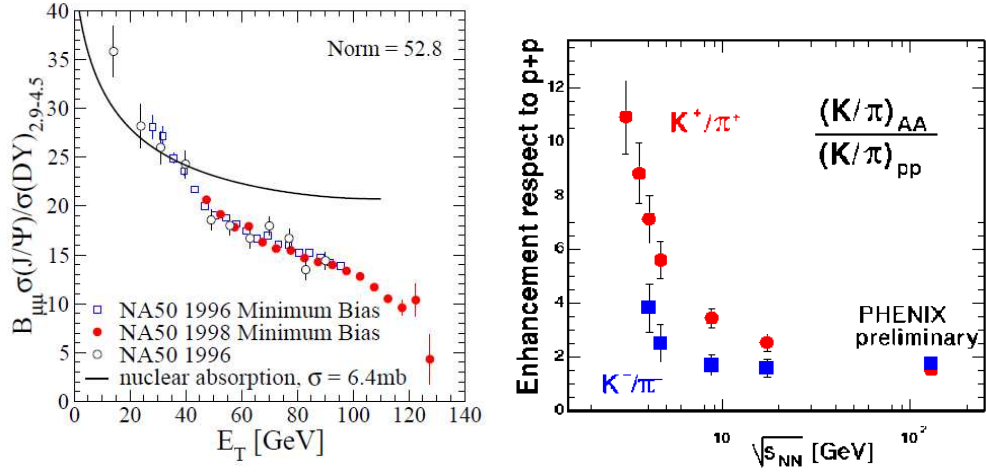


Figure 2.7: *Left* - Nuclear absorption calculations as a function of total  $E_T$  for the Pb+Pb collisions at  $\sqrt{s_{NN}}=158$  GeV at SPS, compared to measured data from NA38 and NA50 experiment. The normalization factor  $B_{\mu\mu}$  is fixed as  $B_{\mu\mu} \sigma_{pp}^{J/\Psi} / \sigma_{pp}^{DY} = 52.8$ , and  $\sigma^{DY}$  is Drell-Yan cross section (Drell-Yan process [28] is the annihilation of a quark-antiquark pair and the production of a dilepton pair via an intermediate  $Z$ -boson or virtual photon). Figure is taken from [29]. *Right* -  $K/\pi$  enhancement with respect to p+p collisions as a function of  $\sqrt{s_{NN}}$ . Figure taken from [30].

# Chapter 3

## Jets and Jet Quenching

### 3.1 Jets in Hadronic Collision

Jets are theoretically well understood and experimentally achievable probes of dense matter. Jets are created in a deep hadronic inelastic collisions where two partons undergo a large momentum transfer - hard scattering. From chapter 1.2 we know that free coloured partons do not exist in nature thus they evolve through gluons and soft quark radiation and fragmentation process into a narrow spray of colourless hadrons  $\equiv$  **jet**. These hadrons are then detected in detectors. Creation of jet is illustrated in Fig. 3.1.

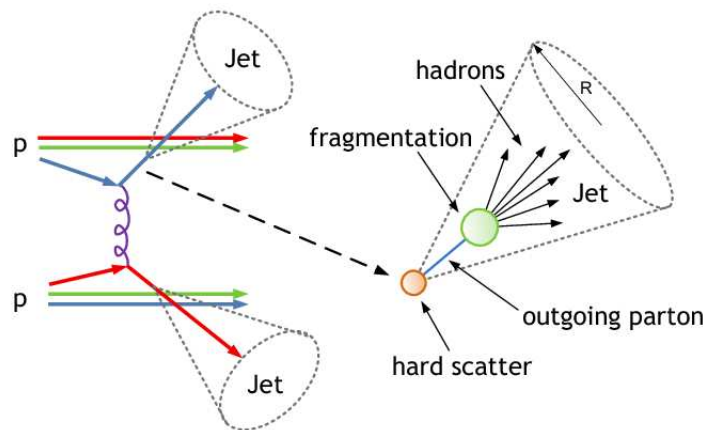


Figure 3.1: Jet on particle level.

Jet characteristics such as a total jet energy, jet shape<sup>1</sup> and others are

---

<sup>1</sup>Jet shape and another characteristics will be defined farther in this section

”footprints” of an properties of outgoing parton. It means that jets are experimental signatures of partons. Jet components have small transverse momenta relative to jet axis and parent parton momentum.

We distinguish jets on detector level which are more phenomenological and they are shortly described in subsection 3.2, and their parent (hardly scattered) partons which are well understood in QCD. These two views on jets are connected with fragmentation which is still not understood from first principles, thus we have to rely on models. Two main models exist, the string and the cluster fragmentation model. Details of these two models are described in [36].

In pQCD a cross section for the partonic process  $A + B \rightarrow C + D + X$  which leads to the most frequent dijet production is given by

$$\frac{d\sigma_{pp}}{dy} = \sum_{ab} \int f_{a/A}(x_a, Q^2) f_{b/B}(x_b, Q^2) \frac{D_{h/cd}(z_{cd}, Q^2)}{z_{cd}} \frac{d\sigma_{ab \rightarrow cd}}{dy} dx_a dx_b dz_c \quad (3.1)$$

where  $f_{a/A}(x_a, Q)$  and  $f_{b/B}(x_b, Q)$  are parton distribution functions (PDF) of the parton  $a$  and  $b$  in hadron  $A$  and  $B$ . PDF characterise a probability of finding parton with momentum fraction  $x$  in a initial hadron<sup>2</sup>.  $D_{h/cd}(z_{cd}, Q^2)$  is a fragmentation function (FF) of parton  $c$  and  $d$  into a hadron and  $\sigma_{ab \rightarrow cd}$  represents the parton-parton cross section. The PDF and FF can not be calculated by pQCD but they are parametrized by experimental data: PDF from proton structure functions  $F_2$  obtained in deep inelastic scattering and FF from  $e^+e^-$  interactions and hadronic collisions. More theoretical information about jets can be found in [41].

## 3.2 Jets in Detector

Jet consists of particles at this level. These particles are detected directly as tracks in trackers or their energy is detected in calorimeter. Now, we need to decide which tracks or cells of the calorimeter is a jet consisted of. This is a task of jet algorithms. There are various kinds of jet finding algorithms, every experiment has often its own version but these are just modified versions of one of the three basic types: cone algorithm<sup>3</sup>,  $k_{\perp}$  and anti- $k_{\perp}$ . When we have jet constituents we can define several jet parameters.

### 3.2.1 Jet Parameters

Basic parameters [37] are jet transverse energy  $E_T$  and position of the jet axis given by pseudorapidity  $\eta_{jet}$  and azimuth  $\phi_{jet}$  (see Appendix A):

---

<sup>2</sup> $x \equiv \frac{p_{parton}}{p_{hadron}}$

<sup>3</sup>This algorithm is described in next section in details

$$E_{Tjet} = \sum_{i \in jet} E_{Ti}, \quad (3.2)$$

$$\eta_{jet} = \sum_{i \in jet} E_{Ti} \eta_i / E_{Tjet}, \quad (3.3)$$

$$\phi_{jet} = \sum_{i \in jet} E_{Ti} \phi_i / E_{Tjet}, \quad (3.4)$$

These variables are boost-invariant and summation is over all particles in a jet. Next, we define a Lorentz-invariant opening "angle" in  $\eta$  and  $\phi$  space between two objects as

$$R_{ij} = \sqrt{(\eta_i - \eta_j)^2 + (\phi_i - \phi_j)^2}. \quad (3.5)$$

Another often used variable is  $j_T$ , which is a component of fragment's  $p_T$  orthogonal to the direction of the jet axis. It is defined as

$$j_T = \frac{|\vec{p}_{jet} \times \vec{p}_{frag}|}{|\vec{p}_{jet}|} \approx p_T^{frag} \sin R \quad (3.6)$$

where  $R$  is the angle between fragment and the jet axis with direction  $\vec{p}_{jet}$ .

Momentum fraction  $z$ , the ratio between the fragment's  $p_T$  along the jet axis and jets  $p_T^{jet}$ , is defined as

$$z = \frac{\vec{p}_{jet} \cdot \vec{p}_{frag}}{|\vec{p}_{jet}|^2} \approx \frac{p_T^{frag}}{E_T^{jet}} \cos R \quad (3.7)$$

If we want to describe the internal jet structure of a jet we can use variable called jet shape given by

$$\Psi(r; R) = \frac{\sum_i E_{Ti} \Theta(r - R_{iJet})}{\sum_i E_{Ti} \Theta(R - R_{iJet})}, \quad (3.8)$$

where summation is over all jet constituents and  $\Theta(x)$  is Heaviside function defined as

$$\Theta(x) = \begin{cases} 0, & x < 0 \\ 1, & x \geq 0. \end{cases} \quad (3.9)$$

We can express this definition in words: the jet shape is a fraction of the jet transverse energy given by the formula (3.2) and transverse energy of jet constituents inside a smaller cone of size  $r$  around the jet axis. We can also use differential jet shape defined as

$$\rho(r; R) = \frac{1}{\Delta r} \frac{\sum_i E_{Ti} \Theta(\Delta r - |r - R_i|)}{\sum_i E_{Ti} \Theta(R - R_{iJet})}, \quad (3.10)$$

or in the limit of  $\Delta r \rightarrow 0$  as

$$\rho(r; R) = \frac{d\Psi(r; R)}{dr}. \quad (3.11)$$

### 3.2.2 Cone Algorithm

In this section we present a description of cone jet algorithm with the same parameters as we use for jet analysis in heavy ion collisions at the ATLAS experiment. An underlying event background in heavy ion collision must be subtracted before jets reconstruction, for more information about heavy ion jet software see [39]. The cone algorithm is based on the iterative-cone concept, with cone radius  $R$  [37]. A result of this algorithm is a cone where particles or cells within the cone are jet constituents, a jet axis is the same as cone axis and jet parameters are defined by formulas (3.2) - (3.4). The algorithm uses a calorimeter tower with tower size  $0.1 \times 0.1$  in  $\eta$  and  $\phi$  for heavy ion collisions at the ATLAS experiment. A jet is found according to the following steps [37]:

1. Calorimeter towers with  $E_T > E_0 = 1$  GeV (this value is used in p+p ATLAS jet reconstruction) are considered as a seed towers for a jet candidates in the next step.
2. A jet is then defined by all towers within an angle  $R = 0.4$  (this value is used in heavy ion ATLAS experiment) from the seed tower according to equation 3.2-3.4.
3. If the jet direction does not coincide with the seed direction, previous step is reiterated, replacing the seed tower by the current jet direction, until a stable jet direction is achieved.
4. This process is repeated for all seed towers.
5. Now we have a long list of jets, one for each seed tower. Duplicates jets are thrown away.
6. Some jets could be overlapping. Any jet sharing at least 50% of its energy with a higher-energy jet is merged with this jet. Jets that have less than 50% of its energy in common with a higher-energy jet is splitted from that jet. Parameters of these jets are than again recalculated according to equations (3.2) - (3.4).

Cone algorithm has two problems - collinear and infrared safety. These problems can be reduced by modification of cone algorithm by adding a midpoint for each jets pair, more can be found in [42] and [43].

### 3.3 Jet Quenching

The main idea of jet quenching is based on the same assumption as hadron high  $p_T$  suppression in the section 2.1. A hard scattered parton traversing through high energy density matter (QGP) may lose energy before it fragments into a jet. If we compare jets in heavy ion collisions with jets in p+p

collisions it could allow us to study the properties of the medium. Fig. 3.2 shows the difference in the fragmentation process in vacuum and QCD medium - QGP.

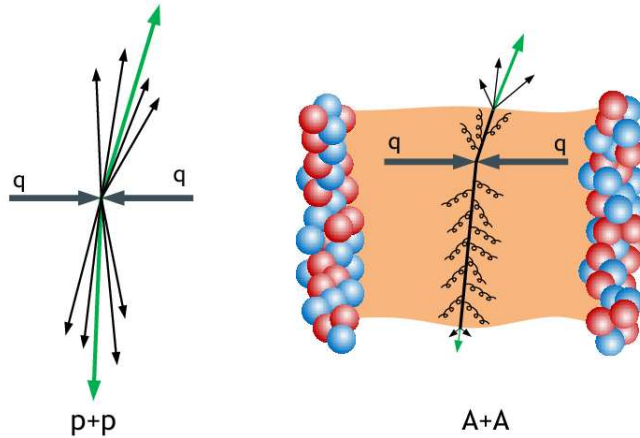


Figure 3.2: Comparison of fragmentation in vacuum (*left*) and QGP (*right*).

First evidence for jet quenching comes from RHIC experiment from studying nuclear modification factor (see section 2.1) and from studying back-to-back correlation of hadrons from STAR experiment shown in Fig. 3.3. In this figure one can see a peak at  $\Delta\phi=0$  called a near-side peak, formed by pairs from the same jet and an away-side peak (for d-Au and p+p collisions) at  $\Delta\phi = \pi$  formed by one particle from a first jet and one from an opposite jet. The away-side peak is reduced in heavy ion collisions. This effect can be explained if one jet is emitted from the surface away from the fireball and the second in the opposite direction, through the fireball.

QCD calculations predict energy loss of partons via gluon radiation<sup>4</sup> in the presence of a dense color medium as illustrated in the right part of Fig. 3.2. A collisional energy loss is negligible.

Since the energy loss depends on the characteristics of the particle traversing the medium [45] (energy  $E$ , mass  $m$ , and charge) and on the QGP properties ( $T$ , particle-medium interaction coupling  $a$ , and thickness  $L$ ) a measurement of energy loss is extremely useful. There are several formalisms and approaches for different scenarios and it is difficult to determine which formalism is more realistic. However, in all formalisms there are several variables that are commonly used [45]:

The **mean free path** defined as

---

<sup>4</sup>It is a similar effect such as bremsstrahlung for electrically charged particles in the presence of electromagnetic fields

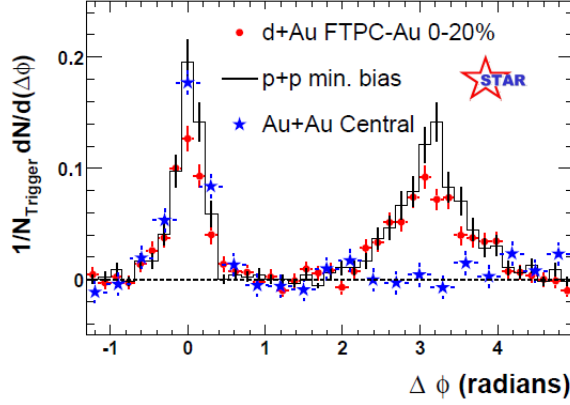


Figure 3.3: Dihadron azimuthal correlations at high  $p_T$  for p+p, central d+Au and central Au+Au collisions. Figure taken from [44]

$$\lambda = \frac{1}{\rho\sigma}, \quad (3.12)$$

where  $\rho$  is the medium density<sup>5</sup> and  $\sigma$  is a total cross section of the particle-medium interaction.

The **opacity**, a number of scatterings of a particle, is defined as

$$N = \frac{L}{\lambda} \quad (3.13)$$

The **Debye mass** characterizes the typical momentum exchanges and gives the order of the “thermal masses” of the plasma constituents. It is given as

$$m_D(T) \sim gT, \quad (3.14)$$

where  $g$  is a coupling parameter.

The **transport coefficient**, it is an average transverse momentum squared transferred to the traversing particle per unit path-length by the medium. It is defined by

$$\hat{q} = \frac{m_D^2}{\lambda}. \quad (3.15)$$

Two theoretical calculations describing jet quenching are introduced in this section. These two approaches differ in medium thickness where they can be used. If medium is thin,  $\lambda \ll L$  we use Bethe-Heitler formula [45]:

$$\Delta E_{rad}^{BH} \approx \alpha_S \hat{q} L^2 \ln \frac{E}{m_D^2 L}. \quad (3.16)$$

The situation is more complicated for thick medium i.e.  $\lambda \gg L$  because destructive effects of emitted gluons have to be considered. Our consideration

---

<sup>5</sup> $\rho \sim T^3$  for an ideal gas

is analogue of the electromagnetic interaction where the bremsstrahlung is smaller for higher density medium - Landau-Pomeranchuk-Migdal (LPM) effect. However, in the LPM approach, one has to differ between the soft or hard gluon radiation. The formula for energy loss in the LPM region can be written as [45]

$$\Delta E_{rad}^{LPM} \approx \alpha_S \hat{q} L^2 \quad \text{for} \quad \omega < \omega_C, \quad (3.17)$$

$$\Delta E_{rad}^{LPM} \approx \alpha_S \hat{q} L^2 \ln \frac{E}{\hat{q} L^2} \quad \text{for} \quad \omega > \omega_C. \quad (3.18)$$

However, these formulas are valid only in an idealistic situation with a static and uniform medium (the real medium rapidly expands and color charge density decreases) and infinite parton energy. If we want to connect the QCD calculation with experiment we have to turn to phenomenology. Four phenomenological approaches have been developed: Path-integral approach to the opacity expansion (BDMPS-LCPI/ASW) which gives the same results as LPM approach, Reaction Operator approach to the opacity expansion (DGLV), Higher Twist (HT) and Finite temperature field theory approach (AMY). More information about these approaches can be found in [45].

Part of implementation of energy loss in BDMPS-LCPI/ASW and DGLV approach is a change of the fragmentation process in formula (3.1) for the cross section. This can be done by shifting the fractional parton energy  $z$

$$z^* = \frac{z}{1 - \varepsilon}, \quad \text{where} \quad \varepsilon = \frac{\Delta E}{E_q} \quad (3.19)$$

Also studying another jet properties defined in section 3.2.1, that can be modified by the medium, will provide us additional information to understand medium and fragmentation process.

Unfortunately, there is a group of effects called initial state effects that can lead to a modification of high  $p_T$  particle production. These so called cold nuclear effect can be measured in in d+A or p+A collisions.

The first known cold nuclear effect is **Cronin effect**. Cronin et al. [46] found that the cross section does not scale with number of target nucleons in p+A collisions. This effect is caused by multiple scattering of initial parton in nucleus. Cross section is then given by

$$E \frac{d^3\sigma}{dp^3}(p_T, A) = E \frac{d^3\sigma}{dp^3}(p_T, 1) A^{\alpha(p_T)}, \quad (3.20)$$

where dependence of parameter  $\alpha$  on  $p_T$  for various particles is shown in Fig. 3.4.

A next cold nuclear effect is **nuclear shadowing** - structure functions  $F_2(x, Q^2)$  per nucleon in nucleus differ from structure functions of free nucleons. This effect is quantified by ratio  $F_2^A(x, Q^2)/F_2^D(x, Q^2)$ , where structure function of deuteron is taken as a reference.

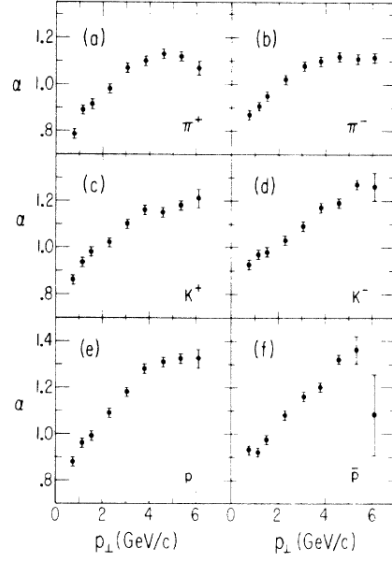


Figure 3.4: Plots of dependence parameter  $\alpha$  on  $p_T$  for a hadron production at 300GeV. Figure taken from [46]

Present-day promising theory which aims to describe effect of cold nuclear matter at early stage of the collision is **Colour Glass Condensate** (CGC). The basic idea is that the gluon (Colour) density in nucleus becomes high (Condensate) due to the Lorentz contraction, coupling  $\alpha_S$  becomes weak and gluons can start to fuse. Gluon fields evolve very slowly to time dilatation (Glass). CGC gives good predictions (for multiplicities for example). More can be found in [47].

# Chapter 4

## The ATLAS Detector

The ATLAS detector (**A Toroidal LHC ApparatuS**), shown in Fig.4.1, is one of the two general purpose detectors at the Large Hadron Collider (LHC). These two detectors are designed for p+p collisions at 14 TeV centre of mass energy and built to perform precision measurements of the Standard Model parameters, to search for the Higgs boson and to search for Supersymmetry and other physics beyond the Standard Model.

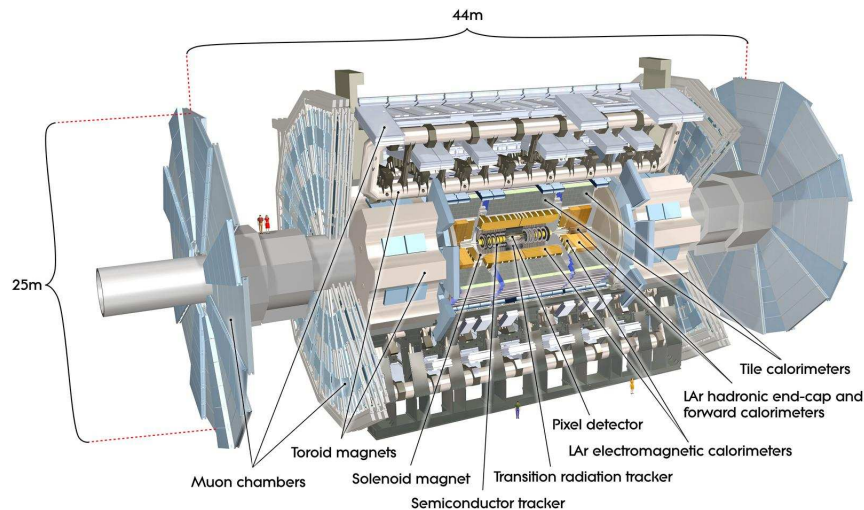


Figure 4.1: The ATLAS detector.

Although ATLAS is primarily designed for p+p collisions, it turns out to be well suited also for Pb+Pb collisions even at the extreme predicted particle multiplicities up to  $dN/d\eta = 3000$  in central events. The LHC will provide Pb+Pb collisions at  $\sqrt{s} = 5.5$  TeV per nucleon [38], energy density may exceed  $30 \text{ GeV}/\text{fm}^3$  which will significantly increase probability that new state of matter will be observed. The heavy ion programme of ATLAS detector is mainly aimed on global variables, heavy flavour physics, low-x physics and jet physics. There are several new possibilities in jet physics in

comparison with RHIC experiments, full jet reconstruction will be possible. Another advantage is significantly higher jet rate compared to RHIC.

There are other three experiments at LHC: ALICE, CMS and LHCb. ALICE is dedicated heavy ion experiment and CMC has also heavy ion programme.

The ATLAS detector consists of main four parts: inner detector, calorimeter system, muon system and magnet system. These parts cover the full  $2\pi$  in azimuth and  $\eta$  acceptance is shown in Fig 4.2.

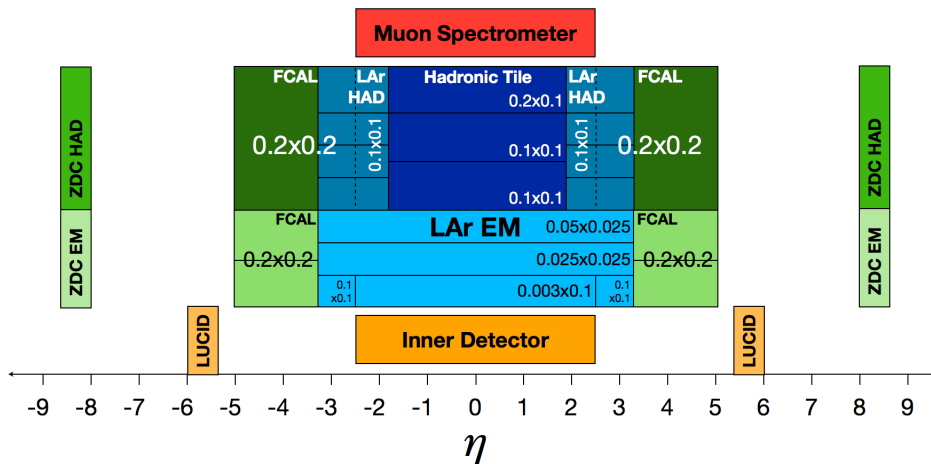


Figure 4.2:  $\eta$  acceptance of the ATLAS detector and all its subdetectors.

## 4.1 Inner Detector

The purpose of the inner detector is to measure tracks of particles in magnetic field  $B = 2$  T (peak 2.6 T). It covers  $|\eta| < 2.5$ . This measurement provides information about pseudorapidity, azimuth angle, transverse momentum and vertices position. Inner detector consists of three subsystems, two are based on silicon detectors and one on transition radiation detection.

- **Pixel detector** is the most inner part of the inner detector. Barrel is consisted of the 3 cylindrical layers with the radial positions of 50.5 mm, 88.5 mm and 122.5 mm and endcap is consisted of three disks on each side which are located 495 mm, 580 mm and 650 mm away from the interaction point. Each of 1744 pixel modules with size of  $50 \mu\text{m} \times 400 \mu\text{m}$  provides extremely precise measurement of two coordinates of the track. Pixel Detector has over 80 million readout channels, which is about 50% of the total number of readout channels. The intrinsic accuracies are  $10 \mu\text{m}$  ( $R - \phi$ ) and  $115 \mu\text{m}$  ( $z$ ). More can be found

in [48]. We have studied occupancy using the most central HIJING events and it should be less than 2% in HI collisions.

- **Semiconductor Tracker (SCT)** is the middle part of the inner detector. It is similar to the pixel detector but instead of pixels it uses two cross layers of  $80 \mu\text{m} \times 126 \text{mm}$  strips on each module. It is composed of four module layers in the barrel (radial positions 30.0, 37.3, 44.7, and 52.0 cm) and endcaps are consisted of nine disks each. The intrinsic accuracies are  $17 \mu\text{m}$  ( $R - \phi$ ) and  $580 \mu\text{m}$  ( $z$ ). More can be found in [48]. Occupancy should be less than 20% in the most central HIJING events.
- **Transition Radiation Tracker (TRT)** is outer part of the inner detector, it is based on transition radiation detection by gaseous straw tube elements interleaved with transition radiation material [48]. It can give about 36 hits for a particle. Each of 351000 straw tubes has diameter 4 mm and they are up to 144 cm long. An intrinsic accuracy is  $130 \mu\text{m}$  per straw. More can be found in [48]. However, the TRT can not be used for heavy ion physics due to the large occupancy.

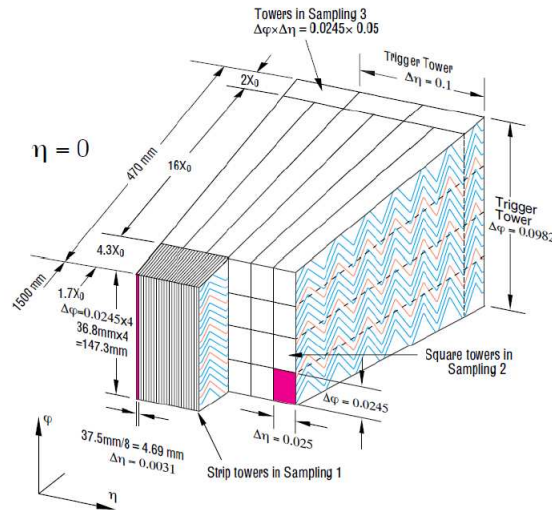


Figure 4.3: Schematic diagram of the ATLAS EM calorimeter.

## 4.2 Calorimeter System

Purpose of calorimeters is particle energy measurement. Calorimetry is destructive measurement because particles are absorbed in a calorimeter material. ATLAS calorimeter system surrounding the inner detector is divided into two parts which cover  $|\eta| < 4.9$ .

- **Liquid Argon Calorimeter (LAr)** is a sampling calorimeter where liquid argon is used as the sampling (detection) material. There are several parts of the ATLAS calorimeter that use this technology. Electromagnetic calorimeter with lead absorber in the barrel endcaps, a hadronic calorimeter with copper absorber in the endcaps, and a forward calorimeter absorber made from copper and tungsten. In the barrel region there is also a thin layer called presampler to measure energy loss in material in front of the calorimeter. More can be found in [48].

Liquid argon calorimeter has very fine segmentation especially in first layer that was designed for distinguishing of  $\gamma$  pairs from  $\pi^0$  and  $H$  decays. Granularity in different layers of barrel part LAr is shown in Fig. 4.3.

- **Tile Calorimeter** is composed from steel absorber and scintillators as an active medium that are read out by wavelength shifting fibres and photomultipliers. It covers the region  $\eta < 1.7$  with inner radius is 228 cm and an outer radius is 423 cm. Granularity is  $0.1 \times 0.1$  in  $\eta$  and  $\phi$ . More can be found in [48].

The ATLAS detector is also equipped with detectors in the very forward region for luminosity and elastic scattering measurements but they will be also used for heavy ion physics.

- **Zero Degree Calorimeter (ZDC)** is located at  $\eta = \pm 8$  and it consists of high segmented electromagnetic calorimeter followed by 2 hadronic calorimeter modules. It is designed for triggering and forward mesons measurement. It will be able also to detect neutrons from spectator fragments of heavy ion collisions.
- **The LUCID gas Cerenkov detector** with acceptance  $5.3 < |\eta| < 6$  is detector primarily designed for luminosity measurement.

### 4.3 Muon System

Muon spectrometer provides  $p_T$  muon measurement by magnetic field  $B = 0.5$  T in the barrel and  $B = 1$  T in endcaps. Monitored Drift Tubes (MDT) and Cathode Strip Chambers (CSC) at large pseudorapidities are used. It extends from the radius 4.25 m to the 11 m and it is divided into barrel covering  $|\eta| < 1$  and endcaps that cover region up to  $|\eta| < 2.7$ . Triggering on muons is possible in area  $|\eta| < 2.4$  with using Resistive Plate Chambers (RPC) in the barrel and Thin Gap Chambers (TGC) in endcap regions. More can be found again in [48].

## Chapter 5

# The ATLAS Trigger System in Heavy Ion Collisions

The bunch-crossing frequency of p+p collisions is 40 MHz, leading to an interaction rate of approximately 1 GHz at the nominal luminosity  $10^{34}\text{cm}^{-2}\text{s}^{-1}$ . The data flow is of an order of  $10^7$  MBs $^{-1}$ . This rate is too large for the existing archiving system. The solution is to have a trigger system which selects 200 Hz of potentially interesting events, reducing the data flow to approximately 300 MB/s for archiving.

Since p+p and Pb+Pb collisions differ significantly in event rates and event size (see table 5.1) it is clear that some modifications need to be made to the default trigger configuration.

	p+p	Pb+Pb
High designed luminosity	$10^{34}\text{ cm}^{-2}\text{s}^{-1}$	$10^{27}\text{ cm}^{-2}\text{s}^{-1}$
Charged particles multiplicity	200	3000
Interaction rate	1 GHz	7.7 kHz
Event size	1.5Mb	5Mb
Maximum archiving rate	200Hz	60Hz

Table 5.1: Comparison between expectations for p+p [48] and Pb+Pb collisions [38]

To achieve the desired reduction in trigger rate, ATLAS has a three-level trigger system. The First-Level Trigger (L1) is hardware based. The High-Level Trigger (HLT) is primarily implemented in software and is subdivided into Level-2 (L2) and the Event Filter (EF). An overview of the trigger system is shown in Fig. 5.1. After an event is accepted by the L1, the data from pipeline memories are transferred through the derandomizer to the read out Driver (ROD) out of the detector. The ROD is an interface to the data acquisition (DAQ) system that defines the data format of the event and provides error detection and recovery mechanisms. The data waiting for the L2 decision are temporarily stored in the read out buffers (ROB). Events

accepted by L2 are transferred to the event-building system and then to EF for a final selection.

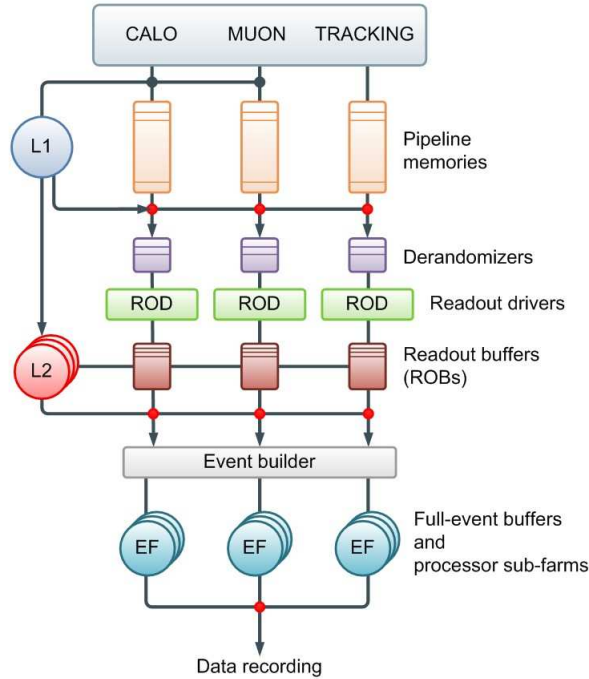


Figure 5.1: Overview of the ATLAS trigger system.

## 5.1 Level-1 Trigger

The L1 trigger is a hardware-based system which can use only simple algorithms because of its small latency limit<sup>1</sup> of  $2.5 \mu\text{s}$ . It is situated partly inside the detector mounted on the modules and partly outside. It uses only a subset of the ATLAS detectors, particularly the calorimeters and muon chambers with reduced granularity. The goal of L1 is to reduce the event rate to 75 kHz. However, since the maximum interaction rate of Pb+Pb collisions is 7.7 kHz [38] a rejection at L1 is not needed. Despite this fact we need an efficient L1 trigger because it provides region of interest (RoI) that are supplied to the L2 trigger. Events that pass the L1 selection conditions are transferred from the detector-specific front-end electronics to the data acquisition system.

The basic quantity for the calorimeter trigger is the "trigger tower", an example of which is shown in Fig. 4.3. The trigger tower combines cells of the actual calorimeter.

<sup>1</sup>L1 latency limit is given by the hardware specifications (size of pipelines, speed of read out).

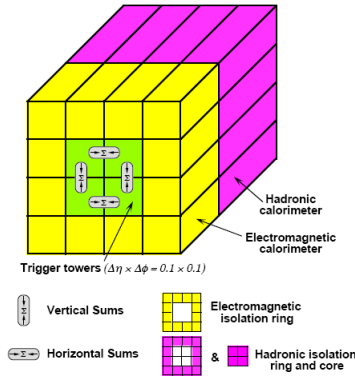


Figure 5.2: Description of the ATLAS trigger tower scheme for EM/Tau RoI's [48].

L1 creates the following types of trigger objects:

- **EM/Tau RoI:** electrons,  $\gamma$ ,  $\tau$  and single hadron candidates. These objects are reconstructed by the electromagnetic calorimeter (electron, photon) and hadronic calorimeter ( $\tau$  and hadrons). The EM/Tau RoI's can be restricted by setting up to 16 thresholds. These thresholds provide criteria for electrons and  $\gamma$  hadronic veto and for EM/Tau isolation. The electron/photon and  $\tau$ /hadron finding algorithms cover  $|\eta| < 2.5$  and are based on a sliding window of  $4 \times 4$  trigger towers with granularity  $0.1 \times 0.1$  in  $\eta$  and  $\varphi$  (see Fig. 5.2). Algorithms use six basic elements [50]:

1. Four overlapping EM clusters (green in Fig. 5.2), each summed over two electromagnetic towers. This element is used to measure the  $E_T$  of electromagnetic showers.
2. A hadronic core, four hadronic towers centred in the algorithm window behind the EM clusters. This sum is used for isolation tests in the hadronic calorimeters.
3. Four hadronic clusters, each summed in depth over the electromagnetic and hadronic calorimeters. These four hadronic clusters are formed by individually summing two-tower EM cluster (item 1) with the hadronic core (item 2). This element is used to measure the  $E_T$  of hadronic showers.
4. An electromagnetic isolation ring (yellow in Fig. 5.2) which consists of 12 electromagnetic towers surrounding clusters. This sum is used for isolation tests in the electromagnetic calorimeters.
5. A hadronic isolation ring (violet in Fig. 5.2) which consists of 12 hadronic towers behind the electromagnetic isolation ring. This sum is used for isolation tests in the hadronic calorimeters.

6. A  $2 \times 2$ -tower cluster RoI, summed in depth over the electromagnetic cluster regions and hadronic core (item 2). Its center is in a local maximum given by the sliding window algorithm.

The requirements for electron/photon RoI's are:

1. The most energetic of the four clusters in the electromagnetic calorimeter must be greater than one of the 16 thresholds.
2. The cluster RoI must be a local  $E_T$  maximum compared to its neighbours
3. Isolation requirements - the total  $E_T$  in the electromagnetic/hadronic isolation ring must be less than the corresponding electromagnetic/hadronic isolation ring threshold.
4. The total  $E_T$  in the hadronic core must be less than the chosen threshold.

The requirements for Tau/hadron objects:

1. The most energetic of the four clusters in the electromagnetic + had. calorimeter must be greater than a given threshold.
  2. The cluster RoI must be a local  $E_T$  maximum compared to its neighbours
  3. Isolation requirements, similar to that used for electron/photon RoI's.
- **Jet RoI:** hadronic jet candidate reconstructed by both hadronic and electromagnetic calorimeter. There are two sets of thresholds: 8 thresholds for central JET RoI's ( $|\eta| < 3.2$ ) and 4 thresholds for forward JET RoI's. The jet trigger algorithm is similar to the  $\tau$ /hadron trigger, but it uses a different granularity and a different cluster size. The basic units are the "jet elements", which are formed by summing over  $2 \times 2$  trigger towers, which means that the granularity is  $0.2 \times 0.2$ . Some jet elements in the forward region ( $|\eta| > 2.4$ ) have a different size which implies that the JET RoI's have also different size, as shown in Fig. 5.3.

The jet algorithm has two components [50]:

1. A  $2 \times 2$  JET RoI
2. Jet windows which are used to measure the jet  $E_T$ . The windows are summed over  $2 \times 2$ ,  $3 \times 3$ , or  $4 \times 4$  jet elements. The jet window slides in steps of one jet element. We use only the  $2 \times 2$  because of the large backgrounds in heavy ion collisions.

There are two requirements for JET RoI's:

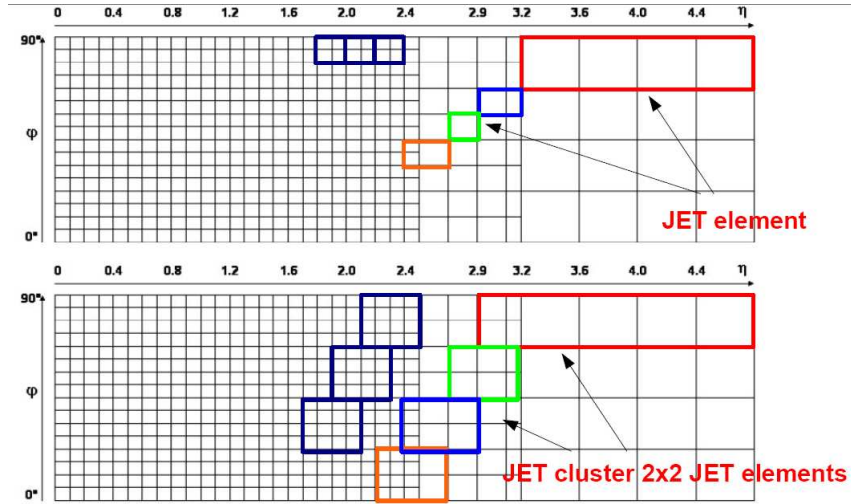


Figure 4: Trigger-tower granularity for  $\eta > 0$  and one quadrant in  $\phi$ .

Figure 5.3: Granularity for triggering in outer region [49].

1. The cluster RoI must be a local  $E_T$  maximum compared to its neighbours.
  2. The jet window  $E_T$  must be greater than the jet threshold.
- **Total  $E_T$ :** Total transverse energy. Four thresholds are available.
  - **Missing  $E_T$ :** Signature of neutral weakly interacting particles. A set of 8 thresholds is available.
  - **Muon RoI:** Muon candidate object reconstructed by the ATLAS muon spectrometer. There are 6 independently programmable  $p_T$  thresholds available.

There are several other conditions for candidate objects to avoid multiple counting of RoI's. More information about the specifications of the L1 trigger can be found in [48] and [49].

## 5.2 The Level-2 Trigger

The level-2 (L2) trigger is based on software selection algorithms running in the processor farms to reduce the rate coming from L1 to about 900 Hz (in p+p to  $\sim 3$  kHz). The L2 algorithms are seeded by L1 RoI's so that only a small fraction of the event is transferred to the L2.

The L2 can access data from all subdetectors with full granularity and latency limit<sup>2</sup> is 40 ms; thus, it can use more sophisticated algorithms. The L2 trigger refines the decision made by L1 and adds additional selection criteria.

The L2 trigger consists of several steps which are grouped together into a trigger "chain". Each trigger signature (e.g. a 60 GeV jet, or a 20 GeV muon) corresponds to a set of algorithms that are executed sequentially. There are two basic algorithm types:

1. **Feature extraction algorithms (FEX)** are used to access trigger objects (e.g. clusters, tracks) which are used to create physics objects (e.g. jets, electrons) to confirm the candidate RoI.
2. **Hypothesis algorithms** are used to reconstruct physics objects and apply cuts to them to reject events.

A description of L2 jet trigger for p+p collisions with modification to adapt it to heavy ion collisions can be found in chapter 7. More information about other L2 trigger algorithms can be found in Ref. [48] and [52].

## 5.3 Event Filter

The Event Filter (EF) is also software based. In contrast to L2 it runs after the event building, so it has access to the complete event. Its task is to reduce Pb+Pb rate to 60 Hz, with events accepted by the EF archived to mass storage. The EF first refines the L2 decision, and is seeded by L2 similarly to how L2 is seeded by L1 RoI's. However, the EF uses algorithms similar to those used for offline reconstruction, and we expect to adapt our current offline scheme to the trigger in the near future.

---

<sup>2</sup>L2 latency limit is given by performance of L2 computer farm (500 multi-core computers)

# Chapter 6

## Tuning the L1 calorimeter Trigger System in Simulations for HI Collisions

The main aim of this work, simulations of the ATLAS trigger system, starts in this chapter. We used PYTHIA [53] events with 70 – 140 GeV jets. The jets were embedded into unquenched HIJING [17] events. Beside these two collections we use minimum bias HIJING events. The full detector simulation for testing the L1 trigger system was used. HIJING is a standard software for generating underlying heavy ion events (further on called background) at the ATLAS experiment. We use the official software framework called Athena<sup>1</sup> [54], which provides the reconstruction, analysis algorithms and software needed for the HEP computing at the ATLAS experiment. We tested the influence of collision centrality on the trigger performance by using three samples of different impact parameter, which controls the background multiplicity. The analysis was carried out for three impact parameter selections,  $b=2, 6, 10$  fm, which have average multiplicity  $dN/d\eta = 2700, 1700, 460$ .

Although we do not need any rejection at L1, we can not simply skip L1 because it provides RoI's for L2. The trigger efficiency is strongly influenced by the number of RoI's that are transferred from L1 to L2. This number is limited by the trigger specifications - sizes of readout drivers (RODs). The limit for JET RoI's is 92 (coming from the fact that there are two RODs and 48 RoI words in each, 4 words have to be subtracted for MET + JE trigger). The limit for EM/Tau RoI's is 64 which is important for heavy ion collisions. If the number of RoI's reaches the limit, the recording stops. This implies that loose thresholds can cause an effective loss of a part of calorimeter. An illustration of this effect is in Fig. 6.1, where the asymmetry in  $\eta$  is caused by exceeding the maximum number of RoI's.

The left plot of Fig. 6.2 shows the number of EM/Tau RoI's for the

---

<sup>1</sup>We used versions 14.2.20 for our L1 trigger simulations

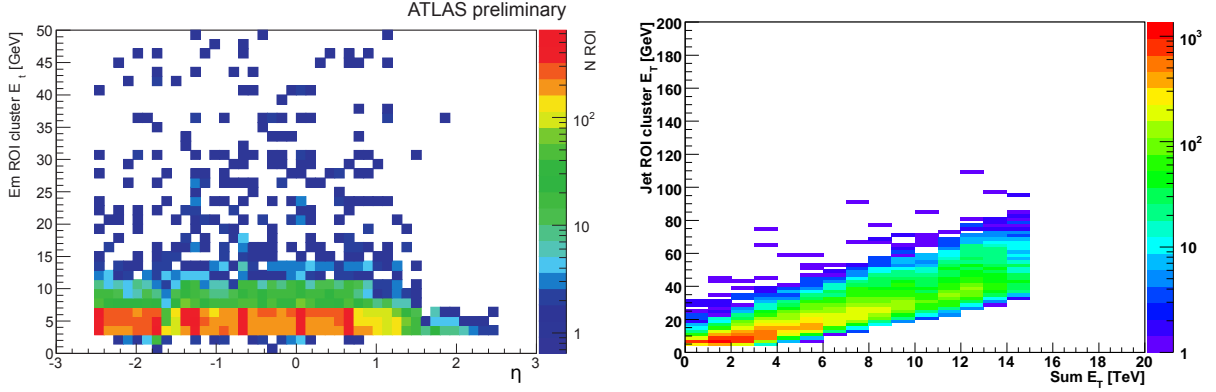


Figure 6.1: *Left*:  $E_T$  versus  $\eta$  distribution of EM/Tau RoI's in electromagnetic calorimeter for centrality  $b = 6$  fm. *Right*: Dependence of JET RoI  $E_T$  on total  $E_T$  in calorimeters for minimum bias HIJING events.

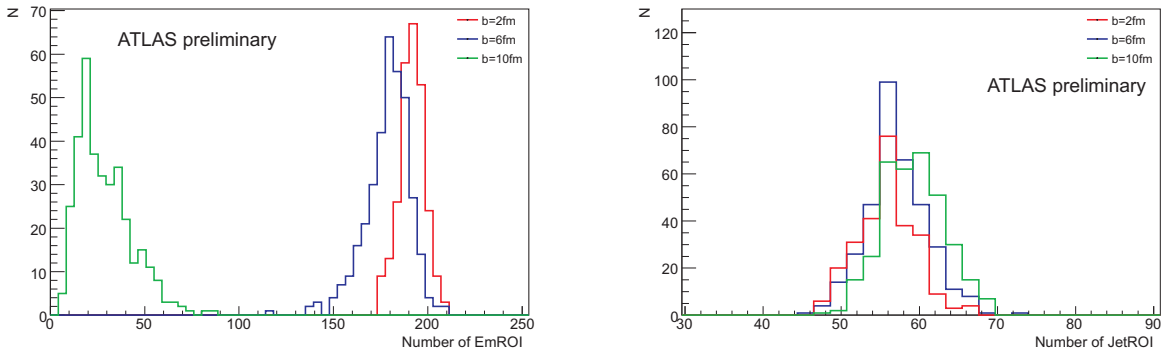


Figure 6.2: *Left*: Number of EM/Tau RoI's for a 3 GeV threshold for EM RoI's and 5 GeV for Tau RoI's. *Right*: Number of JET RoI's for a 5 GeV threshold.

lowest default p+p threshold. The right plot of Fig. 6.2 shows the number of JET RoI's for the lowest default threshold. Clearly we need to optimize thresholds for EM/Tau RoI in order to accept as many interesting RoI's as possible, but to stay below the maximum allowed. Although the maximum number of JET RoI's is still under the saturation limit we have to optimize these thresholds too, because of timing requirement at L2 (processing time per one RoI is in order of units of ms and the latency limit of L2 is 40 ms). L1 JET thresholds have to be set up as an optimal interplay between timing requirement and efficiency.

Optimal thresholds can be estimated from Figs. 6.3 and 6.4 showing differential and integral distributions of EM/Tau (left) and JET (right) RoI's for the different collision centralities. The broad peaks with the mean value approximately 10, 30 and 50 GeV for  $b=10$ , 6 and 2 fm in distributions are from HI background. It means that the background is  $\sim 0.5$ , 2 and 3

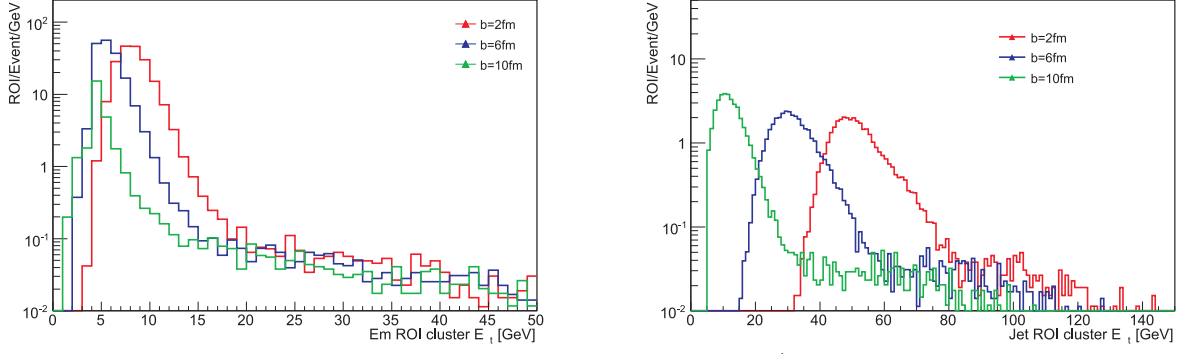


Figure 6.3: *Left*: Differential distribution for EM/Tau RoI  $E_T$ . *Right*: Differential distribution for JET RoI's  $E_T$  in  $|\eta < 2.4|$  for three centrality bins ( $b = 2, 6$  and  $10$  fm).

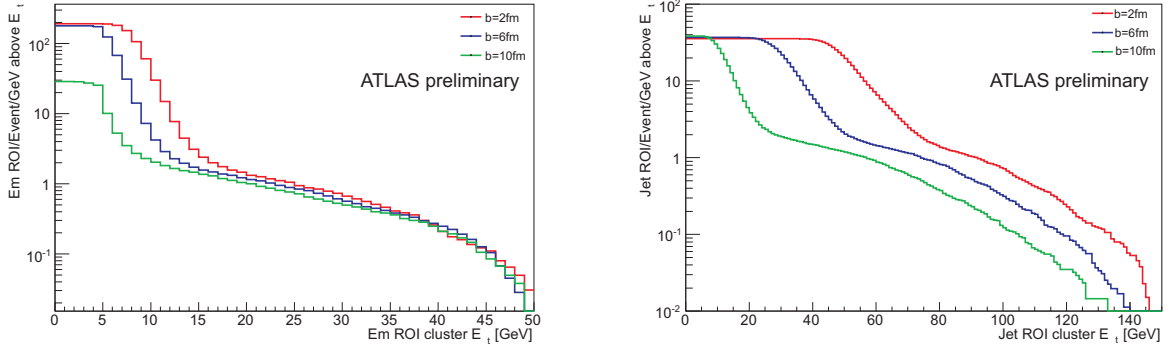


Figure 6.4: *Left*: Integral distribution for EM/Tau RoI's  $E_T$ . *Right*: Integral distribution for JET RoI's  $E_T$  in  $|\eta < 2.4|$  for three centrality bins ( $b = 2, 6$  and  $10$  fm).

GeV per tower ( $0.1 \times 0.1$ ). "Fluctuations" in tails of distributions are jets. Especially the integral distribution is very useful for threshold setting: the value on the y-axis is a number of RoI's per event satisfying a given threshold (value on the x-axis). However, these plots show distributions of RoI's only for  $|\eta < 2.4|$  because in outer region the situation is more complicated, more details can be found in the section 6.2.

It is evident that number of RoI's and its energy distribution significantly depends on the centrality. Centrality can be characterized by total transverse energy  $E_T$  in calorimeters. Dependence of the energy of JET RoI's on the total  $E_T$  is presented in right Fig. 6.1. This plot was obtained by reconstructing  $\sim 10000$  minimum bias HIJING events.

We have developed three strategies for L1 calorimeter trigger to avoid the saturation effect. Two of them are more sophisticated and designed for nominal luminosity, the third one is simple and suitable for the first run. These strategies differ in efficiency and in amount of modifications needed to be made to the default trigger configuration and will be discussed later in this chapter.

## 6.1 $e/\gamma$ and $\tau$ /hadron L1 Trigger

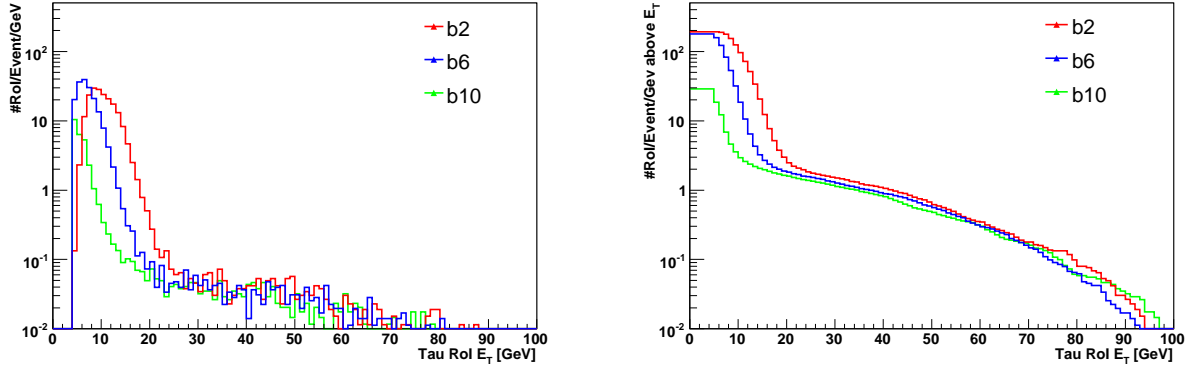


Figure 6.5: *Left*: Differential distribution for Tau RoI's  $E_T$ . *Right*: Integral distribution for Tau RoI's  $E_T$  for three centrality bins ( $b = 2, 6$  and  $10$  fm).

The  $e/\gamma$  and  $\tau$ /hadron trigger share the same "buffer" for RoI's and the reconstruction algorithm is very similar for both types of RoI. Algorithms differ only in isolation conditions and in the requirement on maximum energy of hadronic core which is for  $e/\gamma$  applied only if we require isolation. It implies that most of RoI's are  $e/\gamma$  and  $\tau$ /hadron RoI's together. Fig. 6.5 shows energy distribution of Tau RoI's only. The distribution only for EM RoI's is practically identical with these in Fig. 6.3 and 6.4 because almost every Tau RoI is also EM RoI.

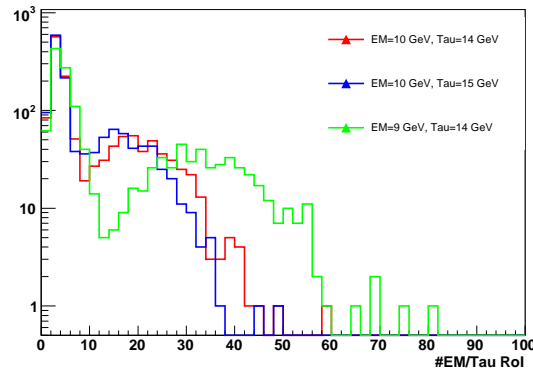


Figure 6.6: Distribution of number EM/Tau RoI's in minimum bias HIJING events for three different combination of thresholds.

In the case of one threshold for the whole centrality range, optimal thresholds were obtained from Fig. 6.6 where a distribution of number EM/Tau RoI's is presented from minimum bias HIJING events. Optimal thresholds are 14 GeV (16 GeV with current p+p menu) for Tau RoI's and 9 GeV (13 GeV with current p+p menu) for EM RoI's.

## 6.2 Forward and Endcap Region

It has been mentioned that the endcaps and forward calorimeters have a coarser granularity (see Fig. 5.3). This leads to the effect that JET RoI's in this region have larger size which implies higher energy than in the central region (as shown in left panel of Fig. 6.7). This can bias efficiency and increase the number of RoI's in the endcap and in an interface between endcaps and forward regions. There is no such problem with EM/Tau RoI's, the distribution for these RoI's shown in right panel of Fig. 6.7 is almost uniform.

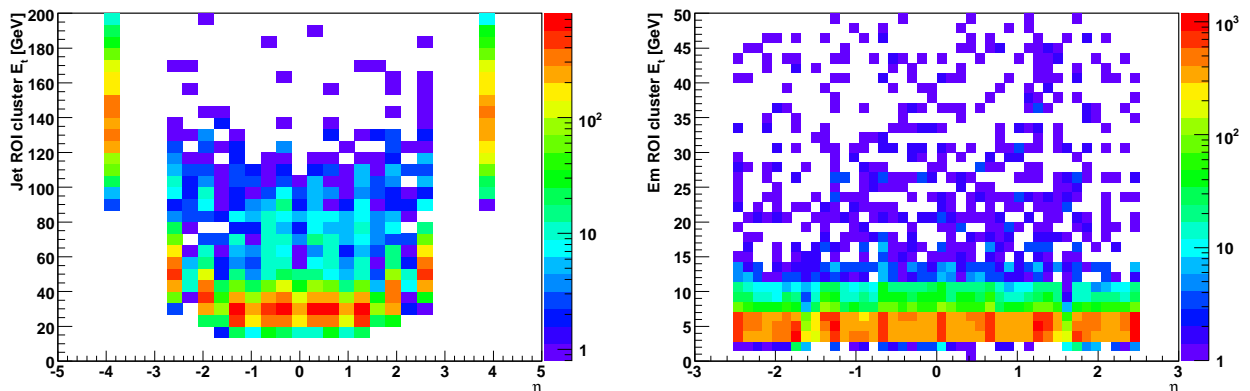


Figure 6.7: *Left*: JET's  $E_T$  versus  $\eta$  distribution for centrality  $b=6$  fm: strips at large pseudorapidity are forward JET RoI's. The "U-shape" is caused by coarser granularity in the endcaps. *Right*: EM/Tau's  $E_T$  versus  $\eta$  distribution for centrality  $b=6$  fm: uniform response in whole  $\eta$  range except near spikes caused by detector material.

Naturally, this "U-shape" significantly affects high  $E_T$  part of spectra in Fig. 6.3 and 6.4. Spectrum for full  $\eta$  range is shown in Fig. 6.8 where RoI's up to  $|\eta| < 3.2$  are included (i.e. endcaps are included). One can see increase of number of RoI's around 50 GeV for  $b = 6$  fm and around 90 GeV for  $b = 2$  fm which is caused just by RoI's in the region  $2.4 < |\eta| < 3.2$ . This leads to higher efficiency in this area because all thresholds suggested in the next chapters are below these values. If we than search for an optimal threshold we have to use distribution in Fig. 6.4 not in Fig. 6.8.

Forward jets are defined in  $3.2 < |\eta| < 4.9$ , they can be seen as strips at  $\eta=3.9$  in left panel of Fig. 6.7. Their energy distribution is shown in Fig. 6.9. HI events still have a significant average energy density per unit  $\Delta\eta\Delta\phi$  in this area and the jets being superimposed on top of this. The Forward RoI have more than 8 times the area of the JET RoI in central region and the mean background energy of these RoI's is approximately 250, 150 and 50 GeV for  $b = 2, 6$  and 10 fm events (left panel of Fig. 6.9). Thus, it make it difficult to estimate whether they contain jets at the trigger level. So we will probably automatically accept all forward JET RoI's (12 forward JET

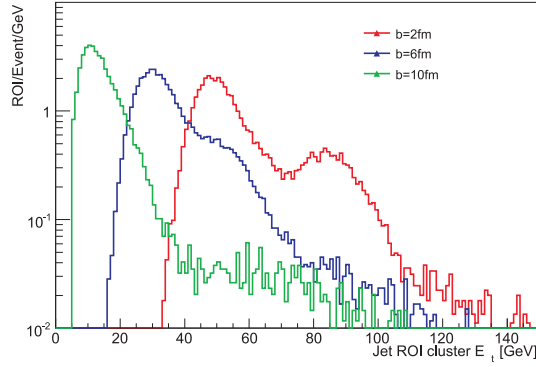


Figure 6.8: Distribution for JET RoI's for  $|\eta < 3.2|$  for three centrality bins ( $b = 2, 6$  and  $10$  fm).

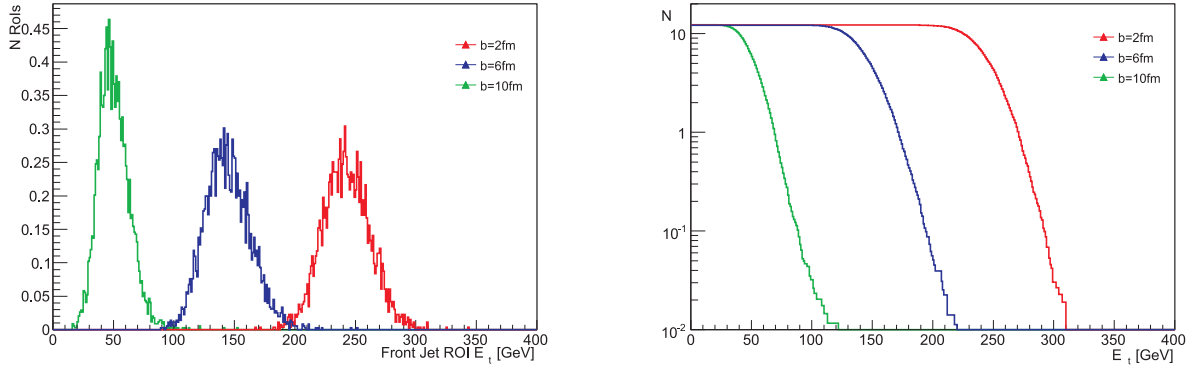


Figure 6.9: *Left*: Forward JET's  $E_T$  differential distribution for three centrality bins ( $b = 2, 6$  and  $10$  fm). *Right*: Forward JET's integral(*right*) distribution for three centrality bins ( $b = 2, 6$  and  $10$  fm).

RoI's in each event) and the limit for JET RoI's in central area will be then reduced to  $\sim 84$ .

### 6.3 Strategy no.1: Centrality-Dependent Thresholds

This strategy is based on a possibility of using different trigger thresholds for events with different centrality.

As a first attempt to optimize the L1 trigger, we use dijets to calculate thresholds in order to have an average of five RoI's per event that is comparable to the number expected in p+p collisions. We can not provide direct centrality measurement but event centrality can be determined using the total  $E_T$  trigger information as one can see in Fig. 6.10. Then we will require a coincidence in Central Trigger Processor (CTP) between the total  $E_T$  and the threshold for EM/JET RoI's:

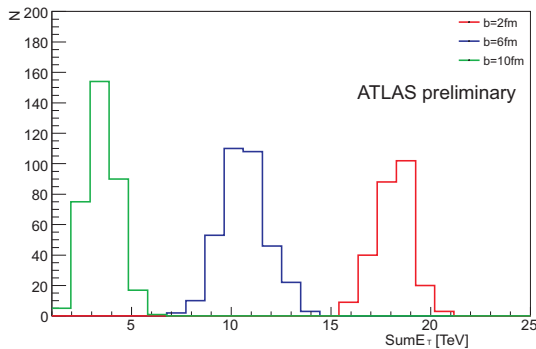


Figure 6.10: Distribution of total  $E_T$  for three centrality bins ( $b = 2,6$  and  $10$  fm).

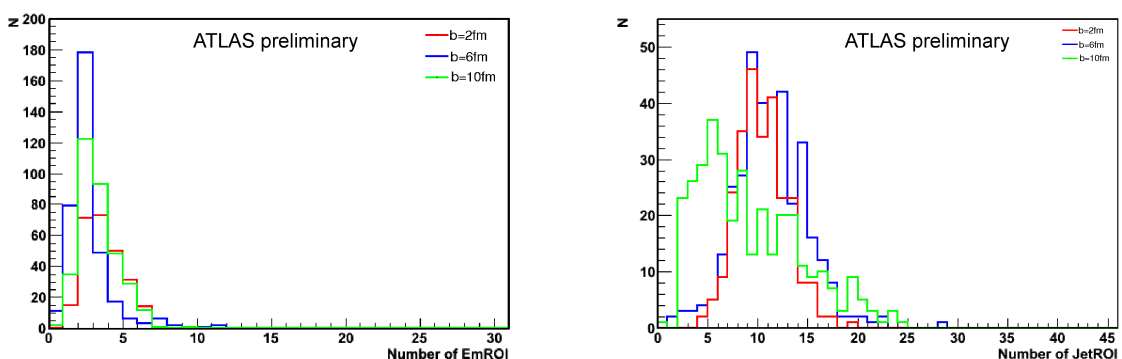


Figure 6.11: *Left*: Number of EM RoI's with suggested thresholds. *Right*: Number of JET RoI's with suggested thresholds.

$$total E_T < X \text{ TeV} \ \& \ RoI E_T > Y \text{ GeV}$$

We can use predefined thresholds for the EM/Tau and JET RoI's but certainly we will have to redefine the thresholds for total  $E_T$  because the current values in firmware, designed for p+p, are too low (the maximum value is presently 650 GeV, while the total energy in peripheral collisions is expected to be 2 TeV). All L1 p+p trigger thresholds can be found in Appendix B. The overall set of suggested thresholds obtained from distribution in Fig. 6.4 is presented in the table 6.1. These thresholds were chosen to provide good efficiency keeping reasonable RoI's multiplicity.

Fig. 6.11 shows the distributions of the number of trigger objects for three different centralities for suggested thresholds. One can see that distribution of EM/Tau RoI's (left panel of Fig. 6.11) is safely below the saturation limit. The right distribution in Fig. 6.11 shows number of JET RoI's in barrel and endcaps (without forward region) but according section 6.2 there is a significant increase of number of RoI's in the endcaps and forward regions. Numbers of RoI's in different calorimeter parts are shown in Fig. 6.12.

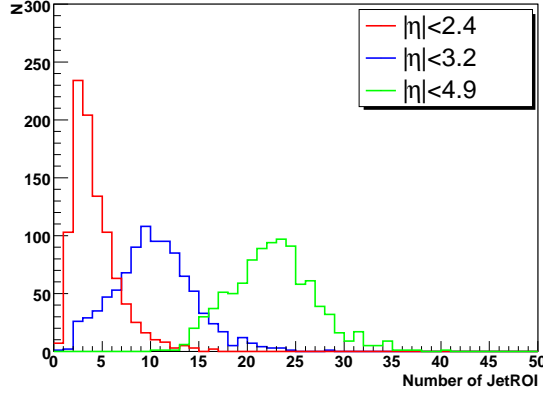


Figure 6.12: Number of JET RoI's with suggested thresholds depending on pseudorapidity position for centrality mix, i.e  $|\eta| < 2.4$  (central region),  $|\eta| < 3.2$  (central region plus endcaps) and  $|\eta| < 4.9$  (whole calorimeter).

Total ET [TeV]	JET threshold [GeV]	EM threshold [GeV]	Tau threshold [GeV]
0-5	18	3	5
5-9	35	7	9
9-13	42	7	11
13-16	70	13	16
> 16	70	13	16

Table 6.1: Suggested trigger menu

### 6.3.1 L1 Jet Trigger Performance

The resulting efficiency can be found in left panel of Fig. 6.13. Jet identified by the L1 trigger was matched to an offline reconstructed jet found by HIJetRec package with the cone algorithm with  $R = 0.4$  and background subtraction, for detail see [38]. The matching criterion is  $R_{ij} = \sqrt{(\eta_{L1} - \eta_{Rec.})^2 + (\phi_{L1} - \phi_{Rec.})^2} < 0.4$  and 0.5 in endcaps.

The efficiency can be further improved by optimizing thresholds for heavy ion collisions (as shown in Table 6.2), see right panel of Fig. 6.13 and by running jet-finding algorithms at L2, not only on JET RoI's but also on EM or Tau/hadron RoI's. This can be seen in the right plot of Fig. 6.14, where Tau/hadron RoI's are also used. The matching criterion in this case is  $R < 0.2$ . But in this case we have to pay attention to timing at L2 because unpacking of these RoI's will take additional processing time.

Fig. 6.15 shows  $\eta$ -dependent efficiency. It is evident that there is a drop-off of efficiency for RoI with  $\eta = 2.95$  - the green cluster in Fig. 5.3. This can be explained by the fact that JET RoI must be a local  $E_T$  maximum - energy of this RoI must be larger than that in the neighbourhood. For that one with  $\eta = 2.95$  it implies that energy of the green cluster must be

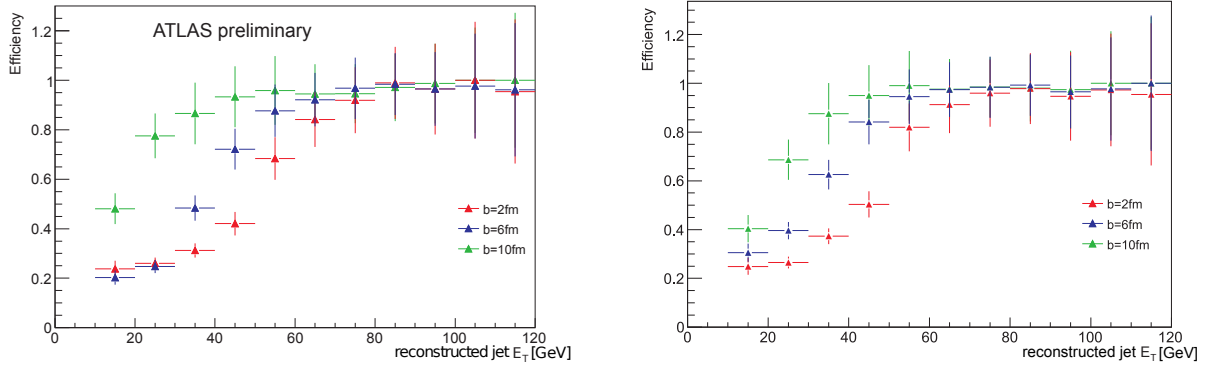


Figure 6.13: *Left*: Jet trigger efficiency without any threshold modifications with respect to the rec. jet energy. *Right*: Jet trigger efficiency with threshold modifications according table 6.2 with respect to the rec. jet energy.

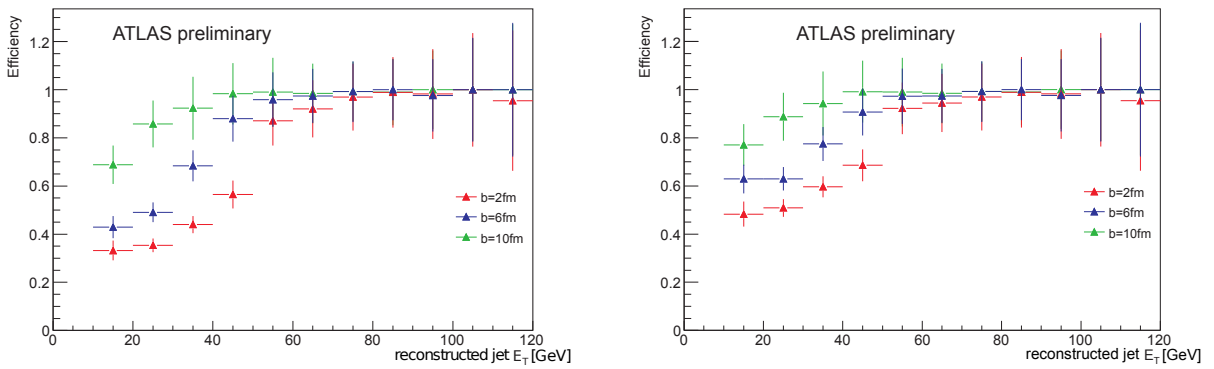


Figure 6.14: Jet trigger efficiency with respect to the rec. jet energy. *Left*: With modified thresholds and if Tau/hadron RoI's are included at L2. *Right*: Tau/hadron and EM RoI's are included as well.

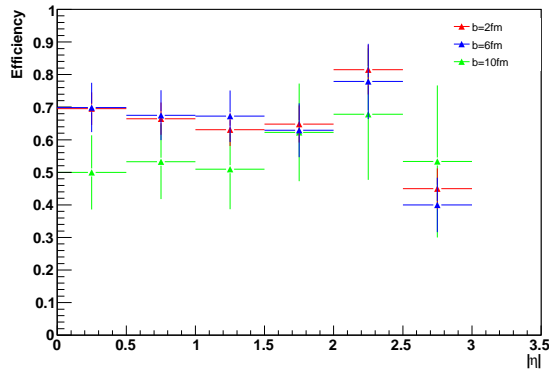


Figure 6.15:  $\eta$ -dependent jet efficiency at L1 for different centralities with respect to the reconstructed jet energy.

Total ET [TeV]	JET threshold [GeV]	EM threshold [GeV]	Tau threshold [GeV]
0-5	18	3	5
5-9	25	6	8
9-13	38	7	10
13-16	50	8	12
> 16	60	9	14

Table 6.2: Proposed modification of trigger thresholds for ATLAS heavy ion running.

larger than energy of blue and red cluster in Fig. 5.3. But the forward JET RoI spans the whole range  $\eta = 3.2-4.9$ , so its area is much larger than other RoI's. We proposed another strategy [51] for forward jet triggering<sup>2</sup> but it have not been tested because our data sample did not contain forward jets:

- We can set higher jet thresholds in FCAL in jet trigger menu. This would help with the RoI multiplicity, but fluctuations in the underlying event might still cause problems. It won't stop "depletion" around  $|\eta|=3$ .
- We can set higher trigger tower noise threshold in the FCAL. This might help with the "depletion" and reducing the forward JET RoI's rate, but suffers same problem with fluctuations in the underlying event.

Nevertheless, this should be tested on real data rather than on Monte Carlo [51].

Fig. 6.16 shows the  $\eta$  (left) and  $\phi$  (right) resolution curves and Fig. 6.17 shows position resolution in  $R$ . These distributions were obtained from the difference between the JET RoI's and the nearest true jet. From left panel of

<sup>2</sup>Our first proposed strategy is to transfer all forward jets directly to L2

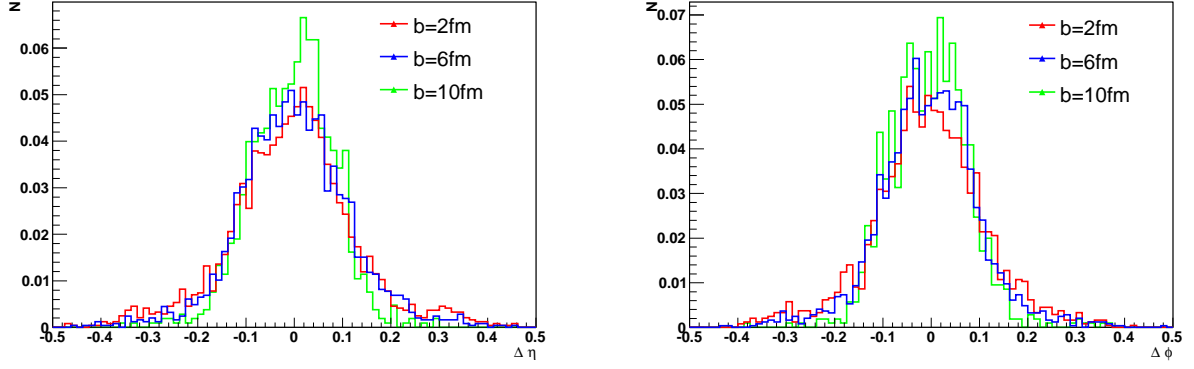


Figure 6.16: *Left*:  $\eta$ -resolution of L1 jets with respect to the rec. jet position. *Right*:  $\phi$ -resolution of L1 jets with respect to the rec. jet position.

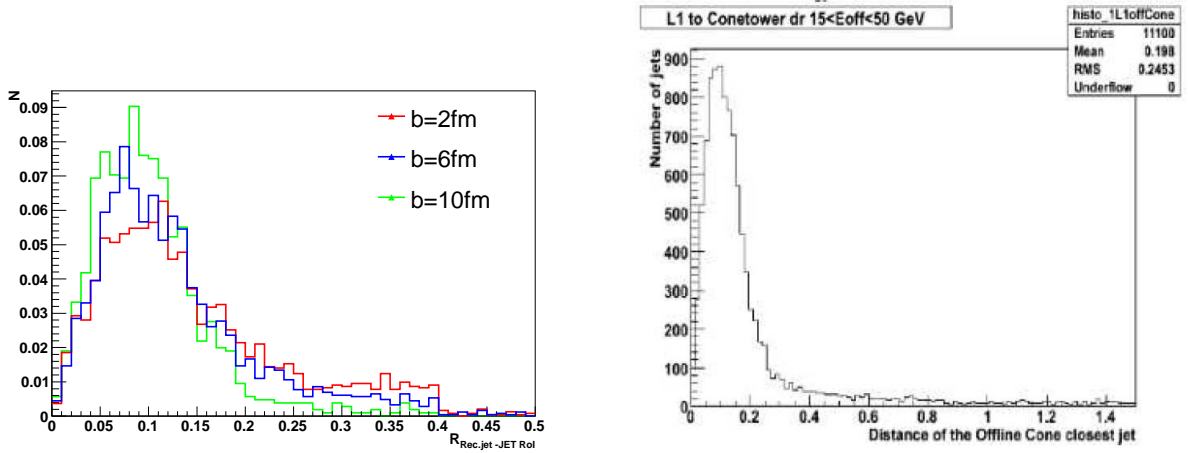


Figure 6.17: *Left*: Distance  $R$  between L1 jets and the rec. jets in Pb+Pb collisions. *Right*: Distance  $R$  between L1 jet and offline reconstructed jets in p+p collisions. Figure taken from [56].

Fig. 6.17 is clear that jet finding algorithm works very well even in the heavy ion collisions because mean of this distribution is less than 0.1 which is a half of minimum step of sliding window. It is also comparable with position resolution in p+p collisions shown in right panel of Fig. 6.17.

### 6.3.2 Limits for Total $E_T$

We want to use L1 total  $E_T$  sum in this strategy to estimate the threshold for an event. However, there are some limits at several stages of the  $E_T$  summation [51]. The global  $E_T$  sum will be treated as saturated (i.e.  $E_T=2^{15}$  GeV  $\approx 32$  TeV) if:

1. single Trigger Tower (TT) (em or had)  $> 255$  GeV
2. jet element layer (2x2 TT, em or had)  $> 511$  GeV
3. jet element (2x2 TT, em + had)  $> 1023$  GeV

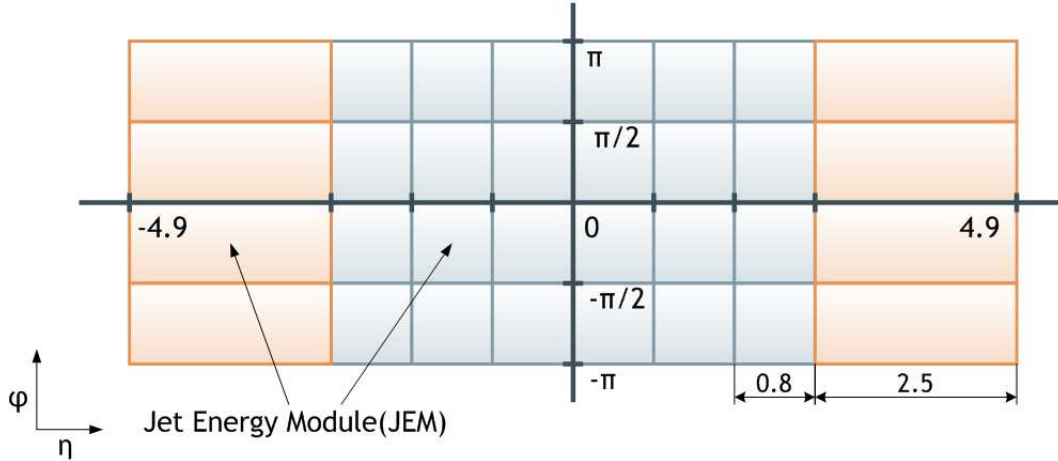


Figure 6.18: Jet/energy modules. There are two kinds of JEMs differ in size

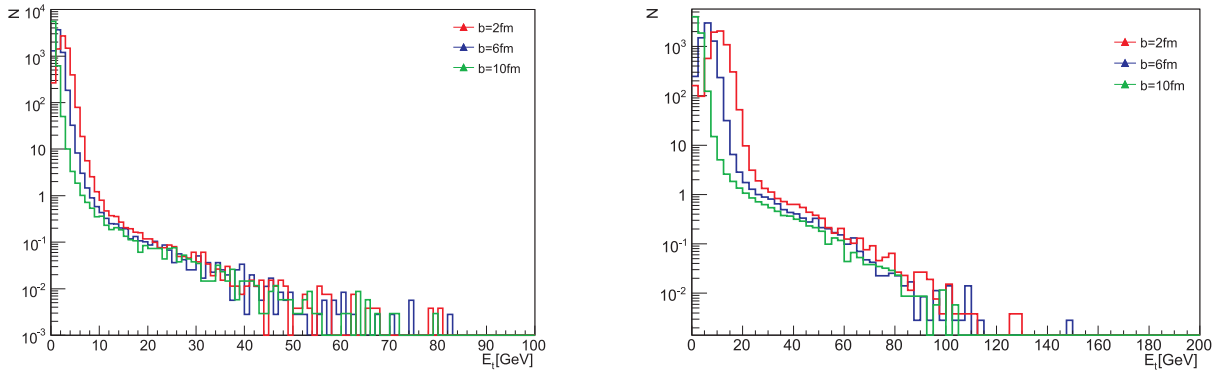


Figure 6.19: *Left*:  $E_T$  distribution of trigger tower clearly under saturation. *Right*:  $E_T$  distribution of jet elements also under saturation.

#### 4. jet/energy module sum (see Fig. 6.18) $> 4031$ GeV

In p+p collisions, saturation begins to become significant (10%) in events with jets above 0.5 TeV. This is dominated by the single tower saturation. Pb+Pb events can be saturated in the same way - by high energy jets, but this is not a problem because in the case of saturation the value of total  $E_T$  will be set up to 32 TeV and then the threshold will be automatically same as for the most central events. Fig. 6.19 presents  $E_T$  distribution of trigger towers (left) and jet elements (right). It is clear from these distributions that a heavy ion event can not be saturated from underlying event at any of the stages 1-3 and the only problematic stage of total  $E_T$  summation could be the JEMs shown in the Fig. 6.18. However, from distribution of JEM's  $E_T$  in Fig. 6.20 it is clear that also JEMs do not mean any problem.

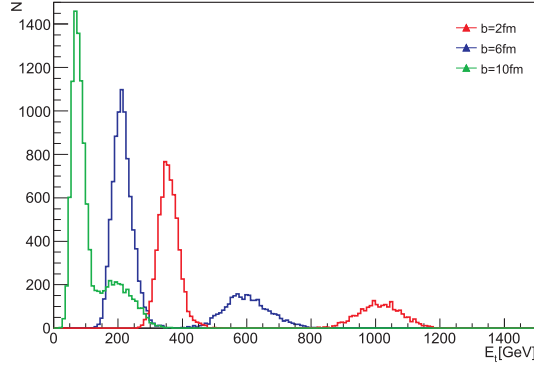


Figure 6.20:  $E_T$  distribution of JEMs. Two peaks are seen with coincidence with two different kinds of JEMs in the Fig. 6.18.

## 6.4 Strategy no.2: Background Subtraction

We can perform a background subtraction already at L1 but it requires significant firmware modifications [51]. The advantage of this method is that the background is determined event-by-event and that it is also  $\eta$  dependent. In previous strategy we used only clusters  $2 \times 2$  of jet elements but the second strategy uses also clusters  $4 \times 4$ .

If we assume that the jet is entirely contained in the  $2 \times 2$  cluster, then in a given event the  $E_T$  in the  $2 \times 2$  cluster is

$$E_T^{2 \times 2} = E_J + E_B, \quad (6.1)$$

where  $E_J$  is jet energy and  $E_B$  is energy of background. While the  $E_J$  in the  $4 \times 4$  cluster is

$$E_T^{4 \times 4} = E_J + 4E_B. \quad (6.2)$$

Thus, we can make the background-subtraction

$$E_J = \frac{1}{3}(4E_T^{2 \times 2} - E_T^{4 \times 4}). \quad (6.3)$$

The assumption that the whole jet  $E_T$  is contained in the  $2 \times 2$  cluster is going to be wrong at some level, but as long as the fraction in the  $2 \times 2$  cluster is large enough the idea still works - the result is still proportional to  $E_J$ , just the constant of proportionality is less than 3. Results of this subtraction are shown in Fig.6.21.

It is evident that subtraction works very well. Distributions for different centralities are very close to each other and we can use only one threshold to be under the saturation limit. This threshold was determined to be 12 GeV.

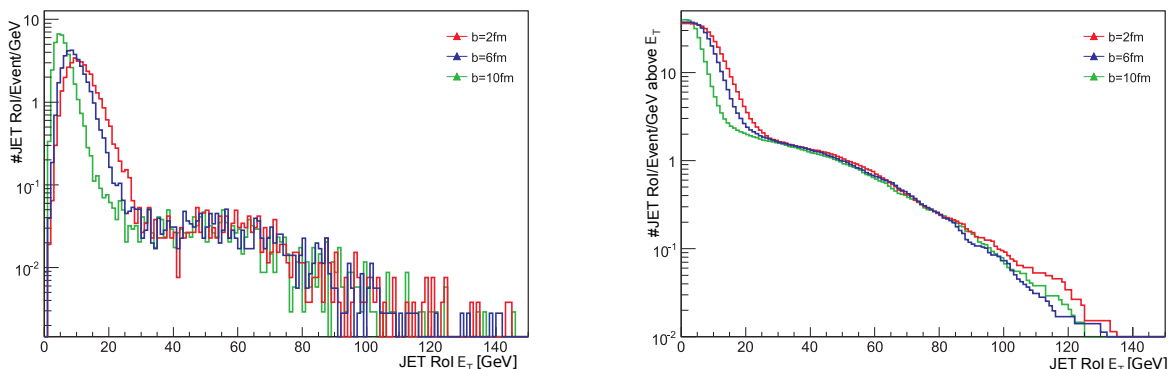


Figure 6.21: *Left*: Differential distribution for Jet RoI's  $E_T$  *Right*: Integral distribution for Jet RoI's  $E_T$ .

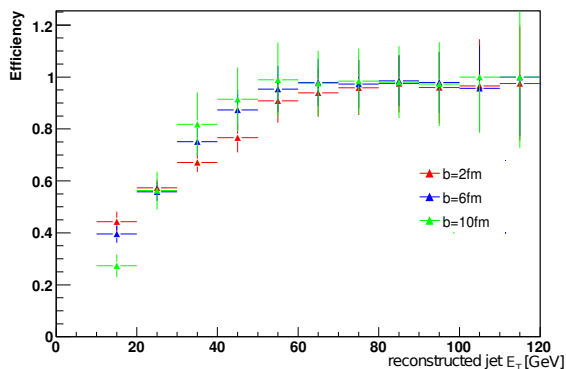


Figure 6.22: Jet trigger efficiency with respect to the reconstructed jet energy.

### 6.4.1 L1 Jet Trigger Performance

We tested performance of this strategy and we compared results with first proposed method as well as with p+p collisions.

The matching criterion was the same as the criterion used in the section 6.3.1, i.e.  $R_{ij} = \sqrt{(\eta_{L1} - \eta_{Rec.})^2 + (\phi_{L1} - \phi_{Rec.})^2} < 0.4$  and 0.5 in end-caps. The crucial trigger parameter - efficiency is shown in Fig. 6.22 and it can be also further improved by running jet-finding algorithms at L2, not only on JET RoI's but also on EM or Tau/hadron RoI's.

The position resolution is the same as in section 6.3.1. Because we subtract background we can compare JET RoI's energy to the true jet energy. The jet energy scale is defined as the ratio between the  $E_T$  of the jet measured in the L1 and the reconstructed jet  $E_T$ . In the left Fig. 6.23, the jet energy scale is shown as a function of the true jet  $E_T$ . The behaviour of jet energy scale is given by combination of two effect. The calorimeter response to hadronic energy is lower than response to electromagnetic energy.

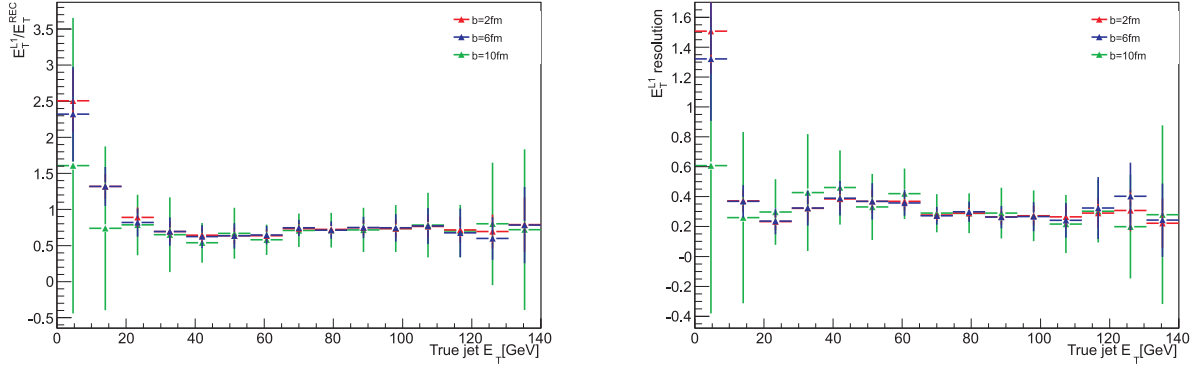


Figure 6.23: *Left*: Jet energy scale as a function of true jet  $E_T$ . *Right*: Jet energy resolution as a function of the true jet  $E_T$ .

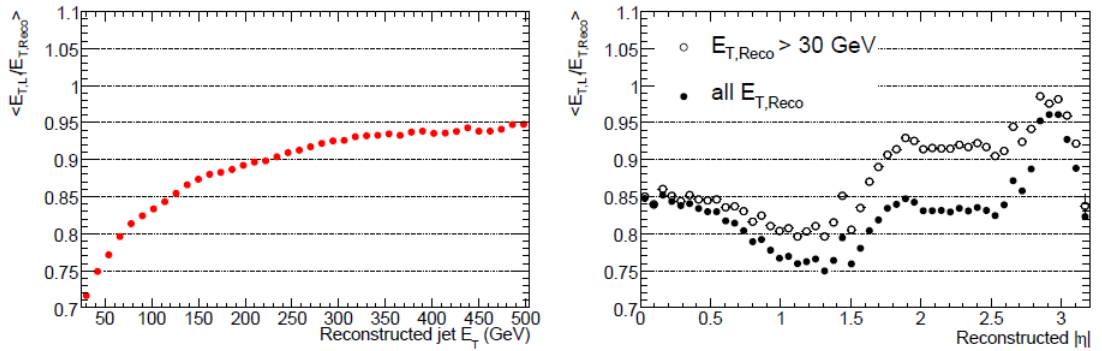


Figure 6.24: *Left*: The L1 jet energy scale as a function of reconstructed offline jet  $E_T$  in p+p collisions. *Right*: The L1 jet energy scale as a function of reconstructed offline jet  $E_T$  in p+p collisions with pile-up. Figures taken from [56].

This is usually balanced by hadronic calibration which is not present at L1. This can cause growing of energy scale above 40 GeV because the fraction of electromagnetic energy deposited by a jet increases with the total energy of the jet [56]. The growth at low energy might be caused by increasing efficiency in each bin of histogram at these low energies and thus selecting more energetic JET RoI's [58].

One can compare jet energy scale in Pb+Pb collisions with those in p+p collisions in left panel of Fig. 6.24 and in p+p collisions with pile-up<sup>3</sup> in right panel of Fig. 6.24.

Next useful parameter is the jet energy resolution defined as  $RMS|E_T^{L1} - E_T^{true}|/E_T^{true}$ . This parameter is shown in the right panel of Fig. 6.23 as a function of the true jet  $E_T$ . The jet energy resolution varies around 30% for

<sup>3</sup>There will be roughly 20 single p+p collisions during one bunch crossing at full luminosity.

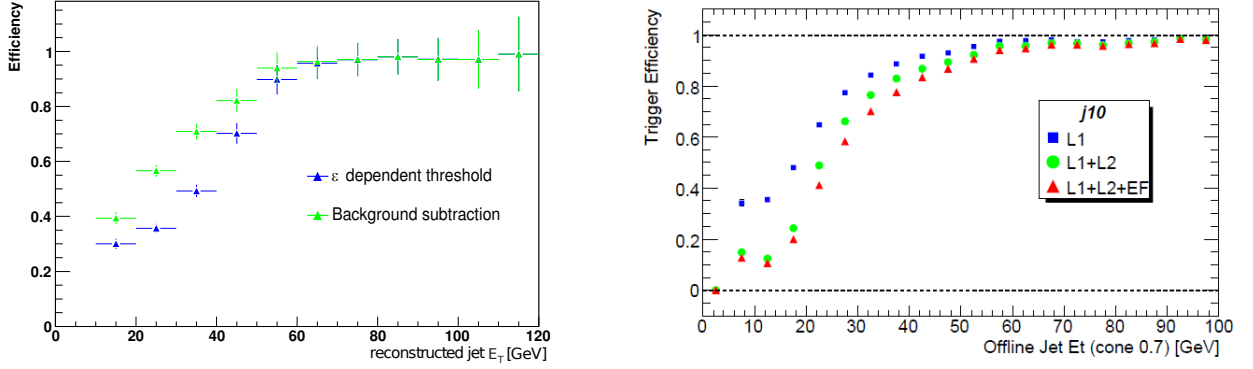


Figure 6.25: *Left*: Comparison efficiencies (with respect to the rec. jet energy) of the first and the second strategy. *Right*: L1, L2 and EF jet trigger efficiency as function of offline reconstructed jet  $E_T$  in p+p collisions with pile-up. Thresholds is 10 GeV at each trigger level. Figures taken from [56].

all jet energies.

Left panel of Fig. 6.25 shows comparison of efficiencies of the first and the second strategy for data sample with a mix of centralities. It is evident that the second strategy gives better results.

It is also interesting and useful to compare efficiency in Pb+Pb collisions with efficiency in p+p collisions. The right panel of Fig. 6.25 shows an efficiency in p+p collisions with pile-up. If we compare efficiency in p+p collisions with pile-up (the right panel of Fig. 6.25) and efficiency in peripheral heavy ion collisions (Fig. 6.13 and Fig. 6.22), we can see that they are very similar.

## 6.4.2 Forward Region

We have already noticed that the size of clusters differ in forward regions. If we make the same assumptions as before, we get

$$E_T^{2 \times 2} = E_J + E_B, \quad (6.4)$$

$$E_T^{4 \times 4} = E_J + 2.2E_B. \quad (6.5)$$

We have to change factor in subtraction and it is tempting to start by considering

$$E_J \approx 2E_T^{4 \times 4} - E_T^{2 \times 2} = E_J - 0.2E_B, \text{ ore more precisely} \quad (6.6)$$

$$E_J = \frac{1}{6}(11E_T^{4 \times 4} - 5E_T^{2 \times 2}). \quad (6.7)$$

This could help with the "depletion" at  $\eta=2.95$  in Fig. 6.15 and also with multiplicity of forward JET RoI's. However, fluctuations in the underlying event might still cause problems in the forward region. These fluctuations are characterized in Fig. 6.26 by width of the peak. This distribution shows

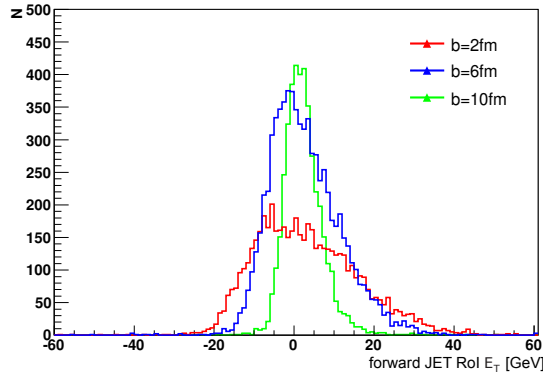


Figure 6.26: Distribution of forward JET RoI's  $E_T$  after subtraction.

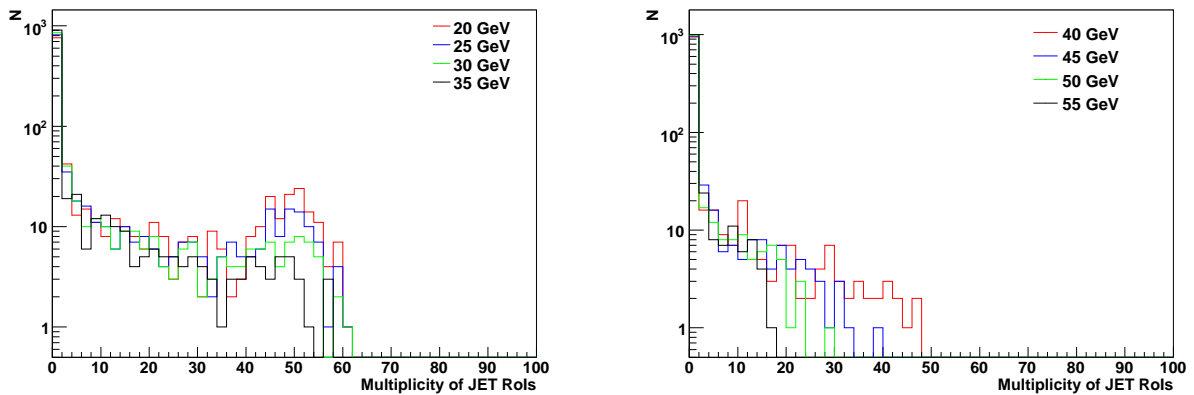


Figure 6.27: Distribution of number of JET RoI's for different L1 thresholds.

energy of forward JET RoI's after background subtraction using the formula 6.7. The data sample did not contain forward jet thus this distribution characterize only background. This energy will be subtracted/added to a jet energy in the forward region if we use this method.

## 6.5 Strategy for the First Heavy Ion Run: Simple Trigger Menu

We are in a situation where different theoretical predictions for particle multiplicity are strongly disagreeing at LHC energy. We expect luminosity to be  $10^{25} \text{cm}^{-2} \text{s}^{-1}$  for the first run which should give rate only  $\sim 80$  Hz. This implies that there will be almost no selection from trigger. Only L1 trigger will be employed, HLT will be in pass-through mode<sup>4</sup>.

We need a simple and flexible strategy to avoid any trigger bias and usable for very first data. A trigger menu build-up from a few simple thresholds

<sup>4</sup>This is the same situation as in p+p trigger at low rates

fulfils the requirements. This menu can be easily changed or prescaled<sup>5</sup>.

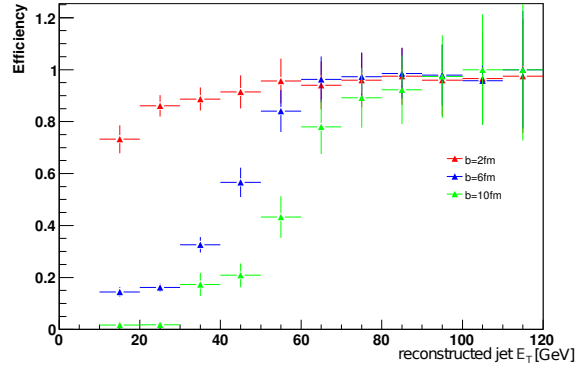


Figure 6.28: Jet trigger efficiency with 45 GeV L1 threshold with respect to the reconstructed jet energy.

We can use plots in Fig. 6.27 as a starting point for construction of this menu. These plots show distribution number of JET RoI's in minimum bias events for eight different threshold. Threshold 45 GeV turns out to provide reasonable efficiency, presented in Fig. 6.28, and timing performance, see chapter 7.3. This threshold is also used as a initial threshold for L2 study.

---

<sup>5</sup>Prescale is used to reduce the amount of events accepted by a certain trigger chain. For instance for a prescale of 10, one event out of 10 events, fulfilling the chain, leads to an accept of the event [59].

# Chapter 7

## Testing the L2 Jet Trigger Algorithm in Simulations

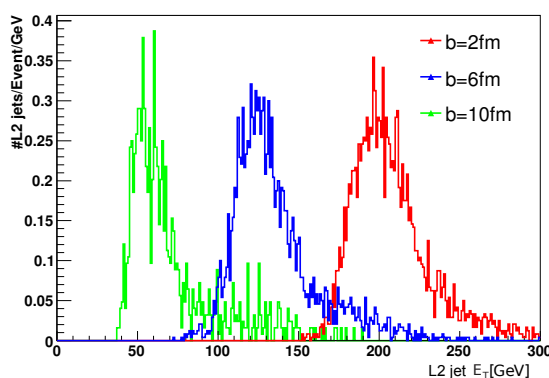


Figure 7.1: Distribution of jet  $E_T$  in L2.

Default p+p jet-finding algorithm at L2 is not adapted for heavy ion collisions. Algorithm does not have an implementation of any background subtraction, although it is absolutely necessary (as well as in the offline analysis). This is evident from Fig. 7.1 which shows the distribution of jet  $E_T$  for different centralities. The input data contained jets with incident parton energy 35 - 70 GeV.

There are two possibilities for L2 trigger, the first approach is based on similar procedure as we present in the chapter 6.3, where threshold depends on centrality characterized by total  $E_T$ . The second approach is based on background subtraction. We have implemented this strategy as a package in ATHENA framework and we show performance of this strategy in next chapters. The analysis of performance was carried out in ATHENA version 14.2.20 except of timing study. However, up to date version of package works well with current ATHENA version 15.6.x.

The default p+p high level jet trigger chain is shown in Fig. 7.2. This chain starts with result of L1 trigger because the available time budget at

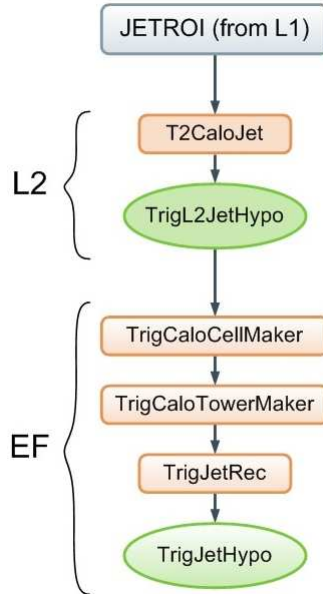


Figure 7.2: HLT jet trigger chain.

L2 of 40 ms per event does not allow unpack data from the full detector. Features (i.e. energy and position) of JET RoI are improved and updated by the Feature EXtraction algorithm (FEX) and then forwarded to a hypothesis algorithm. The hypothesis algorithm for jets is very simple. It retrieves the physics information produced in the FEX (T2CaloJet) and validate hypothesis -  $E_T$  threshold. The default jet FEX algorithm is more complicated and it consists of three parts [56]:

- **Data preparation tool** - L2 jet algorithm has an access to the calorimeter data in a rectangular region centred by L1 RoI with any size. The size is parameter of the algorithm (default is  $1.0 \times 1.0$ ). There are two unpacking methods: cell-based method (T2CaloJetGridFromCells) uses full granularity and front-end board method (T2CaloJetGridFromFEBHeader) uses coarser granularity in electromagnetic calorimeter but still full granularity for Tilecal. Front-End Board (FEB) method turns out to be approximately two times faster than cell based method [56].
- **Jet finding tool** (T2CaloJetConeTool) is a simple cone algorithm with three iterations (parameter) and default cone radius  $R = 0.4$  (it is also a parameter that can be changed) in region  $|\eta| < 3.2$ . Jet finding tool has different parameters in the forward region (a window size  $4.9 > |\eta| > 3$ ) because of the coarser granularity of the L1 forward JET RoI. Different cone size is used for each iteration: the first iteration  $R = 1.0$ , the second iteration  $R = 0.7$  and the third iteration  $R = 0.4$ .

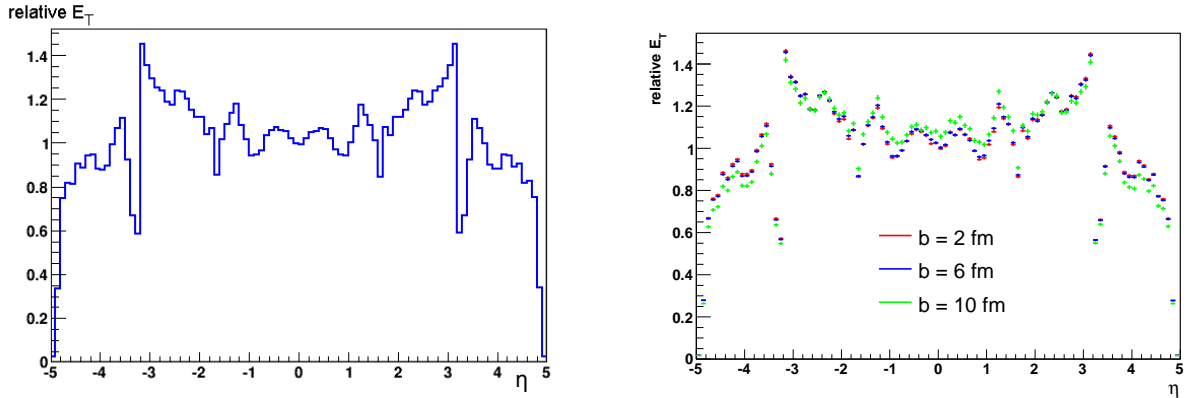


Figure 7.3: *Left:* Relative  $\eta$  distribution of energy of background. *Right:* Relative  $\eta$  distribution of energy of background for different centralities.

- **Calibration tool** (T2CaloJetCalibTool) is used because of different response to the electromagnetic component of a hadron shower and non-electromagnetic component. Weights are applied on EM layer and hadronic layer. Data for calibration are saved in a database and it can be simply changed.

## 7.1 L2 Jet Algorithm for Heavy Ions

This algorithm stems from p+p jet trigger algorithm but it had to be adapted to special condition of heavy ion collision. We use default tools (unpacking, cone tool and calibration) without any modification. We changed the top algorithm<sup>1</sup> and we have total  $E_T$  and all JET RoI's available in the algorithm.

Procedure to deal with background from underlying event is implemented into top algorithm and it is founded on background subtraction. We can't use the "standard" method of background subtraction as in the offline analysis [61] because it is based on subtraction of  $\eta$ -dependent average cell energy from all calorimeter cells but at L2 only small region around RoI is available.

Our implemented strategy is following: We use the standard p+p algorithm and after that we subtract energy from jets as a function of L1 total  $E_T^{L1Sum}$  sum which characterizes the background. The amount of energy for subtraction is directly proportional to the area of a jet  $S_{Jet} = \pi R_{Jet}^2$  and total  $E_T^{L1Sum}$  sum and indirectly proportional to area of the calorimeter  $S_{Cal}$ .

Because the distribution of background is not uniform in whole  $\eta$  range of calorimeter<sup>2</sup> we use  $\eta$ -weighting of background  $W_\eta$ . Calibration weights are applied in  $\eta$  bins of width 0.1. They were obtained by smoothing-up<sup>3</sup> of

<sup>1</sup>We had to change base class from FexAlgo to AllTEAlgo, specifications can be found in [60]

<sup>2</sup>This non uniformity of background is caused not only by  $\eta$  particle distribution but it is also influenced by distribution of dead material in the detector.

<sup>3</sup>Concrete weights were obtained by weighted average (weighted by fraction of area of corresponding jet in this bin) of values in  $\eta$ -bins belonging to jet with given  $\eta$ .

relative  $\eta$  distribution of background shown in left panel of Fig. 7.3. We use the same  $\eta$ -weighting of background for the whole centrality region because the dependence on centrality is very small as can be seen in right Fig. 7.3. Fig. 7.4 shows final weights as they are used in algorithm. These weights will have to be redefined with the real data.

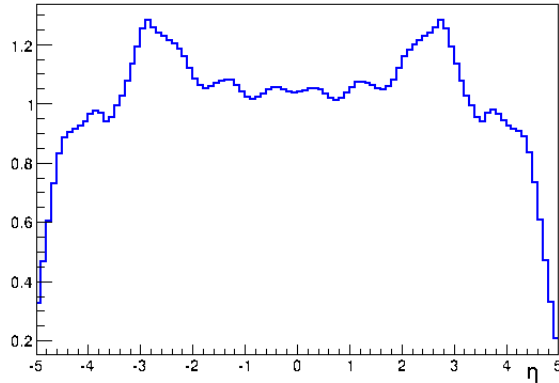


Figure 7.4:  $\eta$ -weights for background calibration.

Complete formula for event-by-event estimation of the jet background  $E_T^B$  is following

$$E_T^B = \frac{E_T^{L1Sum}}{S_{Cal}} S_{Jet} W_\eta. \quad (7.1)$$

Another modification to default algorithm is a protection against saturation in the RoI number or total  $E_T$  sum. If this happens, L2 is bypassed directly to EF, event is accepted and algorithm sends a saturation flag to EF.

Most of default monitoring histograms were not suitable for heavy ions. We modified some of them and added new histograms. A complete overview of monitoring histograms is presented in Appendix 8.

## 7.2 L2 Jet Trigger Performance

Results presented in this chapter were obtained with L2 jet trigger algorithm adapted to heavy ions and with the cell-based unpacking method. Data sample with jets with parton energy of 35 - 140 GeV and events with three impact parameters were used as an input data. Analysis was carried out within ATHENA version 14.2.20. without the application of  $\eta$  weights.  $\eta$  weights were incorporated since version 15.5.3. and they will be tested on new data whose production is ongoing. Thus, we expect better results. L1 jet trigger menu contains only one 45 GeV threshold.

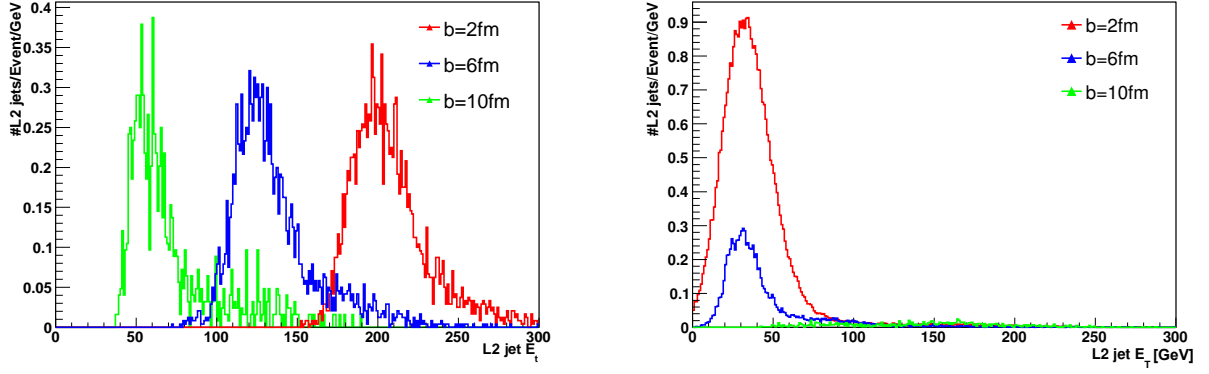


Figure 7.5: *Left*: Distribution of jet  $E_T$  at L2 with default p+p trigger menu for three centrality bins. *Right*: The same distribution after background subtraction at L2. The cut off at 40 GeV for  $b = 10$  fm is caused by L1 45 GeV threshold.

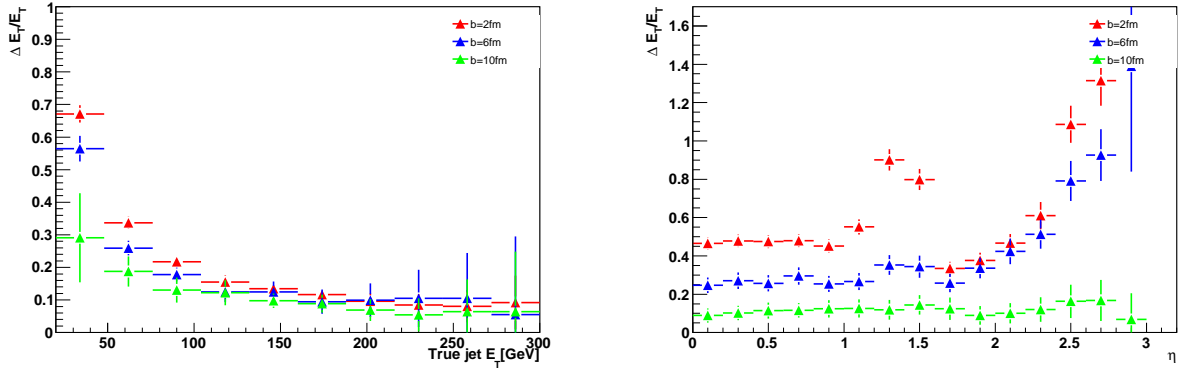


Figure 7.6: *Left*: Jet energy scale as a function of the true jet  $E_T$ . *Right*: Jet energy scale as a function of the true jet  $E_T$ . Two peaks at  $\eta \sim 1.4$  and  $3.0$  are in very nice correlation with peaks in Fig. 7.4 showing calibration weights.

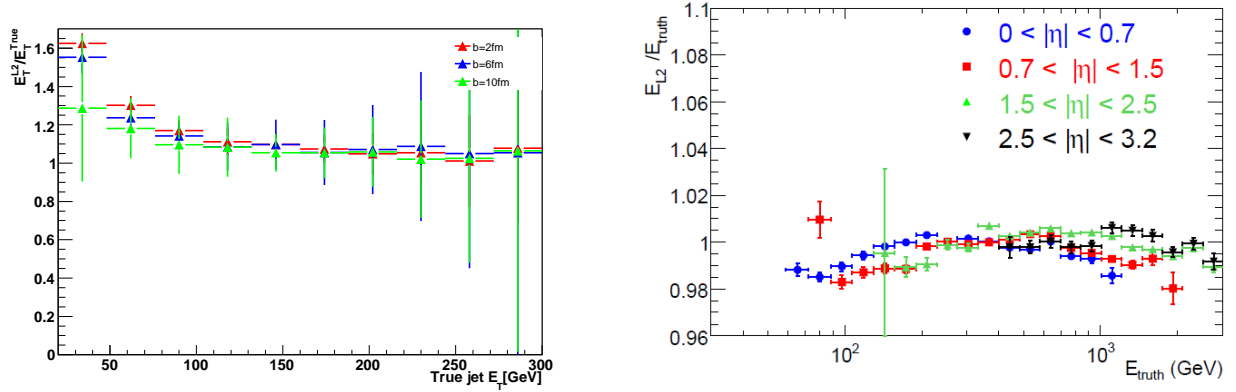


Figure 7.7: *Left*: Jet energy scale for the L2 jets with subtraction as a function of the true jet  $E_T$  for three centrality bins. *Right*: Jet energy scale for the L2 jets as a function of the true jet  $E_T$ , for four different  $\eta$  bins in p+p collisions. Figure taken from [56].

Figures 7.5 present results of subtraction. It is apparent that subtraction is not perfect and there is still large residual background from underlying event mainly in central events (growth of fake jets around 30 GeV). This significant enhancement of fake jets after subtraction originates from the simple fact that L1 requires RoI to be local maximum and it picks up the most energetic parts of background fluctuation<sup>4</sup>. This is confirmed by behaviour of an energy scale for different impact parameters in left panel of Fig. 7.6. The energy of L2 jet is higher than true jet energy mainly at low energies. The energy scale is defined as  $|E_T^{L2} - E_T^{true}|/E_T^{true}$ . The left panel of Fig. 7.6 shows behaviour of jet energy scale on  $\eta$ . It is evident that  $\eta$  weights are absolutely necessary.

We can also compare relative energy scale ( $E_T^{L2}/E_T^{true}$ ) in Pb+Pb collisions with energy scale in p+p collisions. Both distributions can be found in Fig. 7.7. The energy scale is close to unity almost for all the energies (within 10% of unity), thus it is slightly worst comparing to the jet energy scale in p+p collisions (within 2% of unity).

The jet energy resolution at L2 defined as  $RMS(|E_T^{L2} - E_T^{true}|/E_T^{true})$  is shown in left panel of Fig. 7.8 for different impact parameters. The right panel of Fig. 7.8 shows jet energy resolution at L2 in p+p collisions. If we neglect first energy bin with high uncertainty, the energy resolution decreases from  $\sim 30\%$  for the lowest energies below  $\sim 10\%$  for energies above 100 GeV in central collisions. Jet energy resolutions in peripheral collisions and in p+p collisions are comparable, resolution in p+p improves from 12% for the lowest energies to 4% for energies above 1000 GeV.

We also investigated the position resolution of L2 jets despite the fact

<sup>4</sup>Our HIJING settings of sizes of fluctuation is expected to be higher than in real collisions and thus algorithm performance should be better.

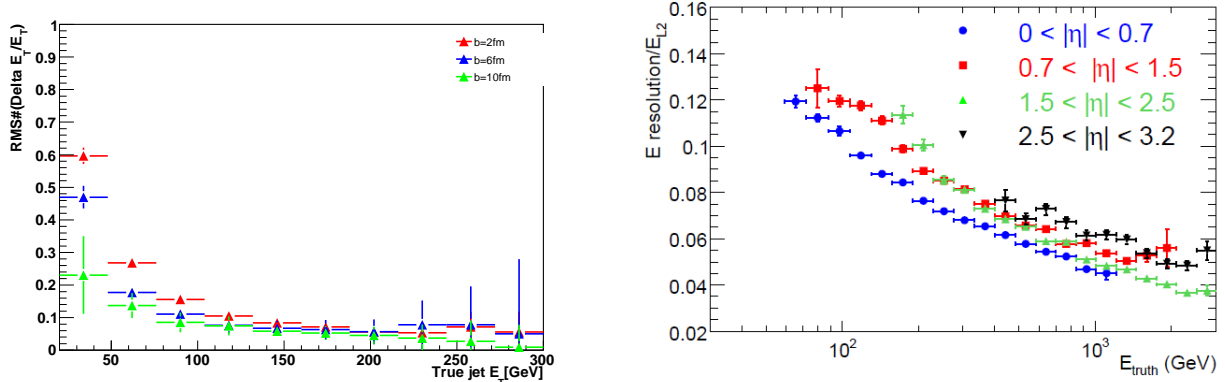


Figure 7.8: *Left*: Jet energy resolution as a function of the true jet  $E_T$  in Pb+Pb collisions *Right*: Jet energy resolution for the L2 jets as a function of the true jet  $E_T$ , for four different  $\eta$  bins in p+p collisions. Figure taken from [56].

collision parameter	$\eta$ sigma of a Gaussian fit	$\phi$ sigma of a Gaussian fit
Pb+Pb, b= 2 fm	0.08	0.06
Pb+Pb, b= 6 fm	0.07	0.04
Pb+Pb, b= 10 fm	0.02	0.01
p+p	0.0006	0.01

Table 7.1: Position resolution of L2 jet trigger.

that it is not such crucial parameter for trigger as energy resolution or efficiency. Distributions in Fig. 7.9 and left panel of Fig. 7.11 were obtained from the difference between the position of L2 jet and its the nearest true jet and it can be compared with resolution in p+p in Fig. 7.10. The standard deviations of Gaussian fit are well-arranged and compared in Tab. 7.1. We can see that peripheral Pb+Pb collisions are comparable to p+p collisions.

The L2 trigger efficiency is limited by the L1 efficiency (the maximal theoretical L2 efficiency is L1 efficiency) thus L2 efficiency without any thresholds is the same as the corresponding L1 efficiency. Because at this moment we have several possibilities for L1 trigger and we need a rejection at L2 it is essential to study the L2 trigger efficiency for some high thresholds. Although the jet trigger menu at L2 is unknown at this moment and it has to be discussed by whole ATLAS HI group, we illustrate the L2 trigger efficiency for threshold 70, 100 and 150 GeV in left panel of Fig. 7.12. These thresholds were chosen because they are significantly higher than L1 threshold 45 GeV which was used for this analysis to avoid an overlapping of effect from two trigger levels. The left panel of Fig. 7.12 shows efficiency for thresholds 35, 42, 70 and 100 GeV in p+p collisions without pile-up<sup>5</sup>.

The limited jet energy resolution and energy scale of the L2 system affects

<sup>5</sup>Analysis of jet trigger in p+p collisions with pile-up is not available

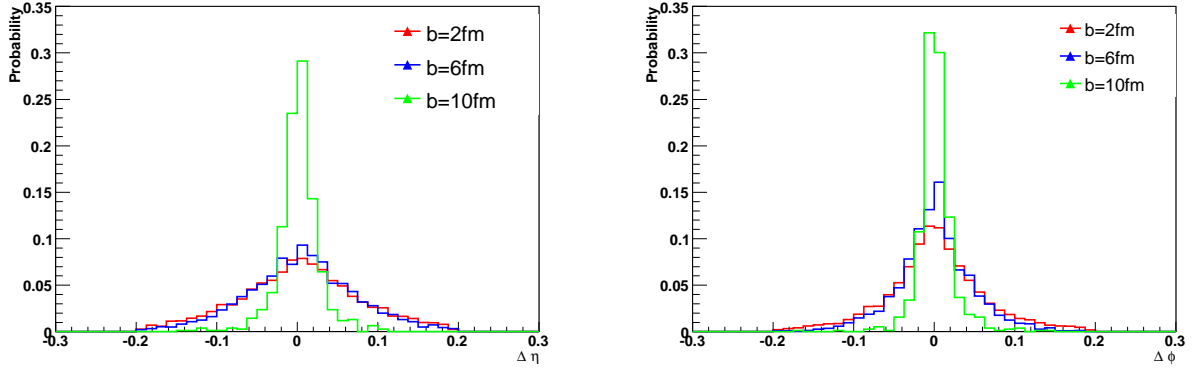


Figure 7.9: *Left*:  $\eta$ -resolution of L2 jets with respect to the true jet position. *Right*:  $\phi$ -resolution of L2 jets with respect to the true jet position.

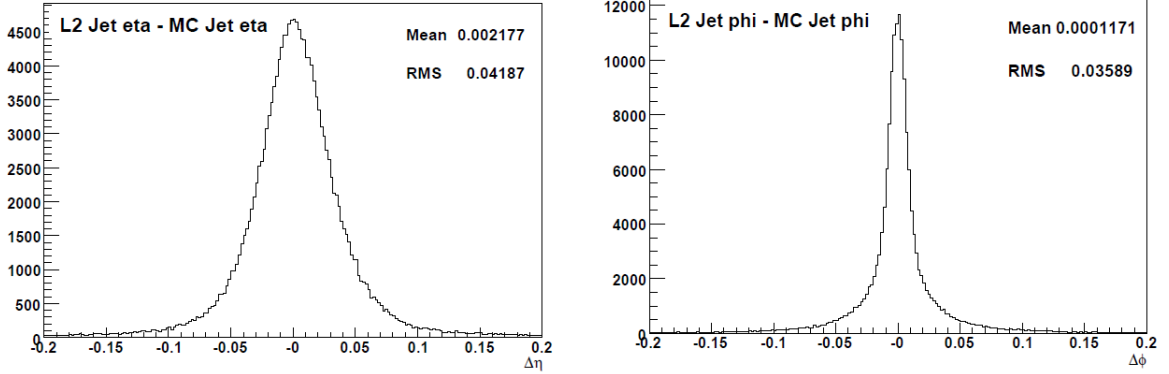


Figure 7.10: *Left*:  $\eta$ -resolution of L2 jets with respect to the true jet position in p+p collisions. *Right*:  $\phi$ -resolution of L2 jets with respect to the true jet position in p+p collisions. Figures taken from [56].

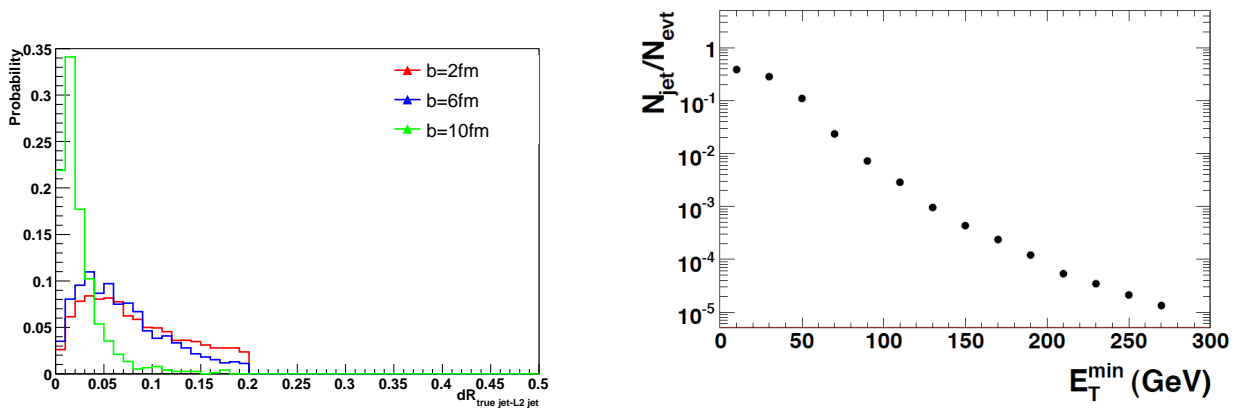


Figure 7.11: *Left*: Distance  $dR$  between L2 jets and the true jets in Pb+Pb collisions. *Right*: Expected jet rate per event in minimum bias Pb+Pb collisions. Figure taken from [38].

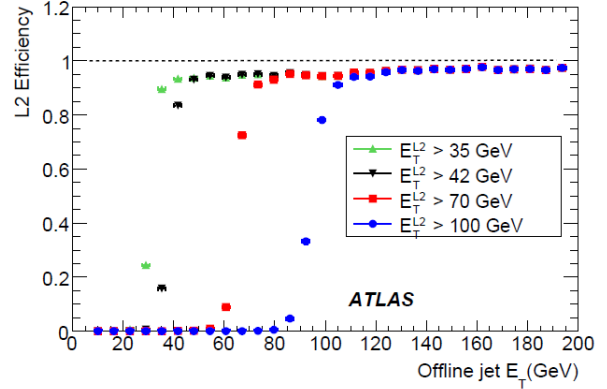
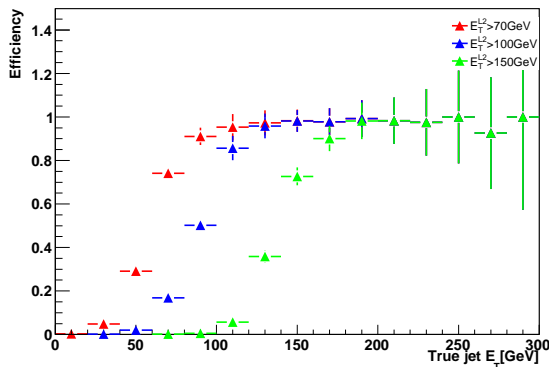


Figure 7.12: *Left*: L2 trigger efficiency with respect to the true jet  $E_T$  for three thresholds in Pb+Pb collisions. *Right*: L2 trigger efficiency with respect to the true jet  $E_T$  for different thresholds in p+p collisions.

the L2 energy thresholds. This causes an earlier initial slope of these efficiency curves in Fig. 7.12. According to Fig. 7.8 the energy of L2 jets is higher than the energy of true jets and true jets correspond to L2 jets thus have lower energy. It causes that some true jets under the L2 threshold can pass.

Effect of downgraded efficiency curves without any thresholds (i.e. maximal L2 efficiency) can be reduced by proper prescale setting in the case of good knowledge of efficiency curve. The jet rate as it is presented in Fig. 7.11 is too high at low energies to accept all events with these jets but we can use downgrade of efficiency instead of prescale.

### 7.3 Timing Performance of L2 Jet Trigger

Latency limit of L2 is 40 ms per event. Although relationship between particular algorithms timing and the average time is not simple thanks to algorithms parallelisation average time for individual algorithms is approximately limited by 40 ms.

The results of timing study in p+p collisions in [56] and comparison of timing in different algorithm steps as we present in Appendix C in Fig. 11 and 12 unambiguously show that total processing time is dominated ( $\sim 90\%$ ) by data unpacking. For this reason we use window with size  $1.0 \times 1.0$  to unpack data around RoI position which gives significant reduction of processing time with only slight impact on algorithm performance, for details see [56].

We tested our heavy ion L2 jet trigger algorithm on 10 000 minimum bias events as well as on HIJING events with embedded jets and defined centrality. Although there is a minimum number of real jets in minimum bias events, they can be well used for timing study because the contribution to processing time from jet is much smaller than contribution from underlying event especially in central collisions. Minimum bias events also embody proper distribution of impact parameter which is presented in Fig. 7.13. This

distribution was obtained by the Phobos [57] Glauber MC simulator with the inelastic nucleon-nucleon cross section  $\sigma_{NN}=72$  mb was used. Its integral distribution is also presented (the red curve).

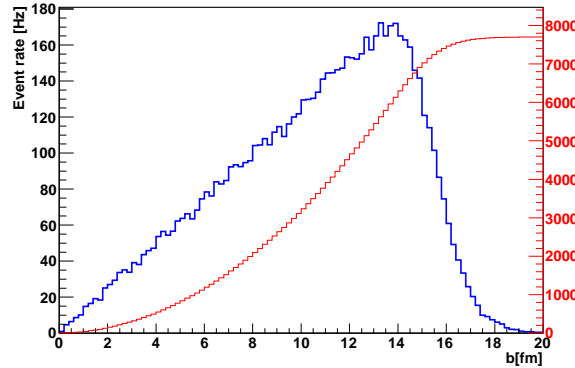


Figure 7.13: The blue curve: Differential distribution of event rate as a function of impact parameter. The red curve: Integral distribution of event rate as a function of impact parameter.

The distribution of total precessing time for minimum bias events is shown in left panel of Fig. 7.14 for two unpacking methods. FEB based method with mean value 16 ms is almost two times faster than cell-based method with mean 34 ms. The results of timing study are only approximative because they were carried out on unknown machines in BNL and during reconstruction from Raw Data Object (RDO) files. We should use Byte Stream (BS) files for proper study but it takes a lot of CPU time and it is in progress. Reconstruction from RDO does not take in to account data collection time from the detector Read Out System (ROS) that is approximately 30% of processing time for the cell-based and 50% for FEB based method.

We can compare these results with timing performance in p+p collisions with jets without pileup<sup>6</sup> that is presented in the right panel of Fig. 7.14 for two unpacking methods. Mean values in heavy ions with correction for collection time from ROS are 32 and 49 ms for FEB and cell-based method and particularly timing performance of FEB method is similar to cell-based method in p+p collisions which gives mean value 22 ms. It is important that average processing time in heavy ions is under the target limit for L2 trigger algorithm.

Algorithm execution time depending on centrality is shown in Fig. 7.15 for both methods. It is evident that long tail at distributions in left panel of Fig. 7.14 is caused by central events.

---

<sup>6</sup>Study with pileup is ongoing.

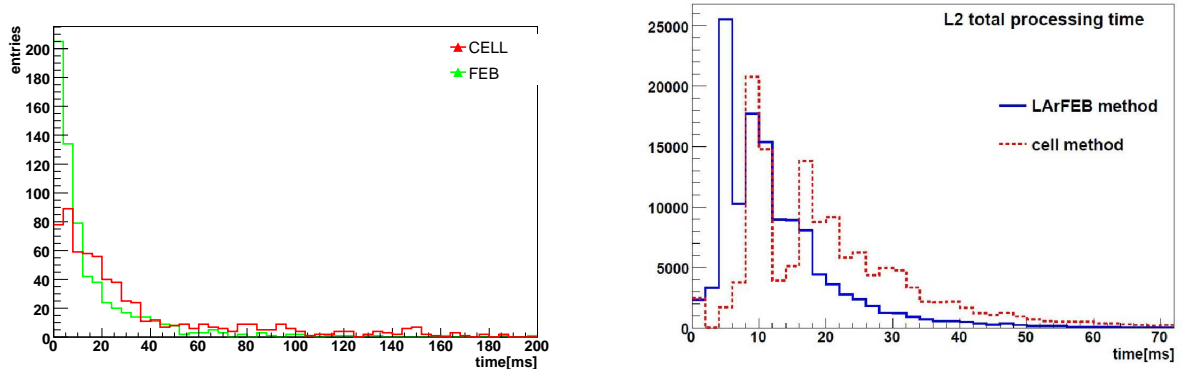


Figure 7.14: *Left*: Total processing time per event of L2 jet algorithm in minimum bias Pb+Pb collisions for two unpacking methods. *Right*: Total processing time per event for L2 jet algorithm in p+p collisions for two unpacking methods. Figure taken from [56].

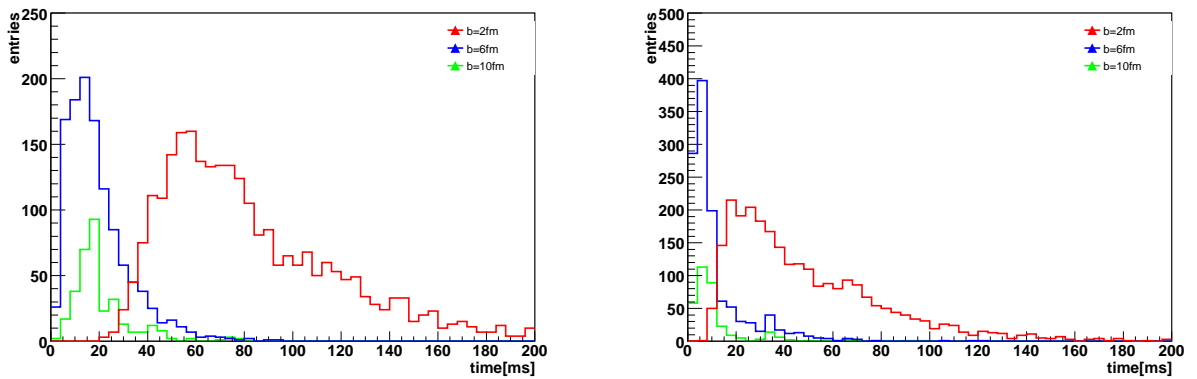


Figure 7.15: *Left*: L2 trigger efficiency with respect to the true jet  $E_T$  for three thresholds in Pb+Pb collisions. *Right*: L2 trigger efficiency with respect to the true jet  $E_T$  for different thresholds in p+p collisions.

# Chapter 8

## Conclusion

The ATLAS trigger is designed to cope with p+p collisions at 1 GHz. We have proposed modest changes to adapt it to heavy ion collisions. We designed two different strategies for L1 trigger adapted to heavy ions where we can have almost 100% efficiency for jets with  $E_T > 60$  GeV and 50% efficiency down to 30 GeV in the most central HIJING events, see Fig. 6.13, 6.14 and 6.22 for centrality dependent efficiencies and Fig. 6.25 where comparison of these two strategies is presented. The proposed L1 trigger menu for the first strategy can be found in Tables 6.1 and 6.2. The second strategy uses background subtraction and only one threshold 12 GeV is needed. The performance of each of these strategies was also presented.

For the first heavy ion run at low luminosity we proposed simple and flexible strategy based on a trigger menu consisting of a few thresholds, see Fig.6.27 . We study trigger behaviour for one 45 GeV threshold that produce a reasonable number of RoI's to reach target timing requirement (see chapter 7.3) with keeping reasonable efficiency that can be found in Fig. 6.28.

However, the strategy with background subtraction gives the best results, but it requires significant firmware modifications. Therefore, the strategy selection for HI trigger is question for future discussion in ATLAS HI group and with trigger experts.

We also studied the performance of the L2 trigger. Default L2 jet algorithm can not be used within heavy ion environment and adaptation to specific characteristics of heavy ion collisions was absolutely necessary.

We implemented background subtraction into the ATHENA framework tested its behaviour in heavy ion collisions. This method subtract background calculated event-by-event from total  $E_T$ . We have implementation of  $\eta$  calibration and some other features. Running of algorithm is monitored by several histograms that can be found in Appendix C. Performance of this algorithm in peripheral Pb+Pb collisions is similar to performance in p+p collisions, more details can be found in chapter 7.1.

It is worth mentioning that real heavy ion collisions and especially their background can differ significantly from simulations. Overall, we can con-

clude that the ATLAS trigger is capable of use in heavy ion collisions.

The partial results of this thesis were presented at conference "High-pT physics at LHC 09" as an oral presentation, at conference "Quark Matter 2009" as a poster and they are used in upcoming paper "Heavy Ion Physics with the ATLAS Detector at the LHC".

# Bibliography

- [1] Particle Data Group, Particle Physics Booklet, 2002, <http://pdg.lbl.gov/>
- [2] Hořejší J., Fundamentals of electroweak theory, The Karolinum Press, Charles University in Prague, 2002
- [3] Wikipedia - Standard model, [http://en.wikipedia.org/wiki/Standard\\_Model](http://en.wikipedia.org/wiki/Standard_Model)
- [4] T. R. Klassen, Phys. Rev. D51 5130., 1995
- [5] B. Povh, K. Rith, C. Scholz and F. Zetsche, Particles and Nuclei, 4th edition, Springer-Verlag.
- [6] J. Dolejší, O. Kotrbová, Standardní model, [http://www-ucjf.troja.mff.cuni.cz/~dolejsi/textbook/particle\\_textbook\\_CZ.htm](http://www-ucjf.troja.mff.cuni.cz/~dolejsi/textbook/particle_textbook_CZ.htm)
- [7] J. Chýla, Quarks, partons and Quantum Chromodynamics, [www-hep2.fzu.cz/Theory/notes/text.pdf](http://www-hep2.fzu.cz/Theory/notes/text.pdf)
- [8] J.I. Kapusta, Finite Temperature Field Theory, Cambridge Univ. Press, 1989
- [9] C. O. E. Jorgensen, Charged Particle Production in Au+Au Collisions at  $\sqrt{s_{NN}}=130$  GeV, Master thesis, University of Copenhagen, 2001.
- [10] S. B. Ruester, V. Werth, M. Buballa, I. A. Shovkovy, D. H. Rischke, The phase diagram of neutral quark matter: Self-consistent treatment of quark masses, arXiv:hep-ph/0503184v2, 2005
- [11] A. Chodos et al. New extended model of hadrons. Phys. Rev. D, 9:34713500, 1974.
- [12] B. Muller. The Physics of the Quark-Gluon Plasma. Springer-Verlag, Berlin, Lecture Notes in Physics, 225, 1985.
- [13] K. Yagi, T. Hatsuda, Y. Miake, Quark-Gluon plasma: from big bang to little bang, Cambridge University Press, 2005
- [14] L.P. Csernai. Introduction to Relativistic Heavy Ion Collisions. John Wiley & Son, Chichester, 1994

- [15] F. Karsch, Lattice QCD at High Temperature and Density, arXiv:hep-lat/0106019v2, 2001
- [16] J. D. Bjorken, Highly relativistic nucleus-nucleus collisions: The central rapidity region, Phys.Rev.D27 140 (1983)
- [17] HIJING:X.-N. Wang and M. Gyulassy, A Monte Carlo model for multiple jet production in p+p, p+A and A+A collisions, Phys. Rev. D44, 3501 (1991).
- [18] T. Kosek, Master thesis: Jet modification in heavy ion collisions, 2009
- [19] Cheuk-Yin Wong, Introduction to High-Energy Heavy-Ion Collisions, World Scientific, 1994
- [20] L. D. Landau, Izv. Akad. Nauk. SSSR Ser. Fiz. 17, 51-54, 1953.
- [21] R. J. Glauber, Phys. Rev. 100, 242 (1955); in Lectures in Theoretical Physics, edited by W. E. Brittin et al. (Interscience, New York, 1959), Vol. 1, p. 315.
- [22] P. Shukla, Glauber model for heavy ion collisions from low energies to high energies, arXiv:nucl-th/0112039v1, 2001
- [23] B. Sahlmueller, Diagnosing energy loss: PHENIX results on high- $p_T$  hadron spectra, the PHENIX Collaboration, Phys. G: Nucl. Part. Phys. 34 S969, 2007
- [24] BRAHMS Collaboration, Transverse-Momentum Spectra in Au+Au and d +Au Collisions at  $\sqrt{s_{NN}}=200$  GeV and the Pseudorapidity Dependence of High- $p_T$  Suppression, arXiv:nucl-ex/0307003v1, 2003
- [25] PHENIX Collaboration, Elliptic Flow of Identified Hadrons in Au+Au Collisions at  $\sqrt{s_{NN}}=200$  GeV, arXiv:nucl-ex/0305013v2, 2003
- [26] R. Lacey, Soft Physics - Flow and bulk properties, talk at Quark Matter 2009, 2009
- [27] PHENIX Collaboration, Scaling Properties of Azimuthal Anisotropy in Au+Au and Cu+Cu Collisions at  $\sqrt{s_{NN}}=200$  GeV, Physical review letters 98(16):162301, 2007
- [28] S.D. Drell and T.-M.Yan, Phys. Rev. Lett. 25, 316 (1970); Erratum ibid. 25 902, 1970
- [29] L. Grandchamp, R. Rapp, Charmonium Suppression and Regeneration from SPS to RHIC, arXiv:hep-ph/0205305v1, 2002
- [30] Y. Akiba, Presentation: Results from PHENIX experiment at RHIC

- [31] T. Peitzmann, M. H. Thoma, Direct Photons from Relativistic Heavy-Ion Collisions, arXiv:hep-ph/0111114v2, 2002
- [32] H. van Hees, R. Rapp, Dileptons in Heavy-Ion Collisions, arXiv:0901.2316v2, 2009
- [33] F. Videbaek and O. Hansen, Phys. Rev. C52, 2684, 1995
- [34] J. Alvarez-Muñiz, R. Conceição, J. Dias de Deus, M.C. Espírito Santo, J. G. Milhano, M. Pimenta A model for net-baryon rapidity distribution, arXiv:0903.0957v2, 2009
- [35] I.C. Arsene et al., Nuclear stopping and rapidity loss in Au+Au collisions at  $\sqrt{s_{NN}}=62.4$  GeV, 2008
- [36] B. R. Webber, Fragmentation and Hadronization, arXiv:hep-ph/9912292v1, 1999
- [37] M. H. Seymour, Jet Phenomenology, 1997, arXiv:hep-ph/9707349v3
- [38] ATLAS Collaboration, Heavy Ion Physics with the ATLAS Detector, Letter of Intent, CERN/LHC/2004-009, LHCC I-013
- [39] A. Angerami, B. Cole, R. Debbe, J. Dolejsi, N. Grau, W. Holzmann, M. Leltchouck, M. Spousta, The HIJetRec Package for Jet Reconstruction in a Heavy Ion Environment in ATLAS, ATL-PHYS-INT-2008-039, CERN, 2008
- [40] M. Spousta, Jet Profiles, 2005,  
<http://ipnp00.troja.mff.cuni.cz/~spousta/thesis.pdf>
- [41] G. Sterman, QCD and Jets, arXiv:hep-ph/0412013 v1, 2004
- [42] G. C. Blazey, J. R. Dittman, S. D. Ellis, V. D. Elvira, K. Frame, S. Grinstein, R. Hirosky, R. Piegaina, H. Schellman, R. Snihur, V. Sorin, D. Zeppenfeld, Run II Jet Physics, hep-ex/0005012, 2000
- [43] R. Mehdiyev, Z. Metreveli, P. Nevski, D. Salihagic, Test of the Sliding Window Algorithm for Jets Reconstruction in ATLAS Hadronic Calorimeters, ATL-CAL-99-002
- [44] STAR Collaboration: J. Adams, et al, Experimental and Theoretical Challenges in the Search for the Quark Gluon Plasma: The STAR Collaboration's Critical Assessment of the Evidence from RHIC Collisions, arXiv:nucl-ex/0501009v3, 2005
- [45] D. d'Enterria, Jet quenching, arXiv:0902.2011v2, 2009
- [46] J. W. Cronin et al., Production of hadrons at large transverse momentum at 200, 300, and 400 GeV, 10.1103/PhysRevD.19.764, 1979

- [47] L. McLerrau, The Color Glass Condensate and Small  $x$  Physics, 4 Lectures, arXiv:hep-ph/0104285v2, 2001
- [48] ATLAS Collaboration, G. Aad et al., The ATLAS experiment at the CERN Large Hadron Collider, 2008, JINST-3-S08003
- [49] ATLAS Collaboration: ATLAS Level-1 Trigger, Technical Design Report, ATLAS TDR-12, CERN, Geneva, 1998
- [50] ATLAS L1Calo Group: ATLAS Level-1 Calorimeter Trigger Algorithms, CERN, Geneva, 2008
- [51] A. Watson, private discussion
- [52] ATLAS Collaboration: ATLAS High-Level Trigger, Data Acquisition and Controls, Technical Design Report, ATLAS TDR-12, CERN, Geneva, 2002
- [53] T. Sjöstrand, S. Mrenna, P. Skands: Pythia 6.4 Physics and Manual, hep-ph/0603175, LU TP 06-13, FERMILAB-PUB-06-052-CD-T, 2006
- [54] ATLAS Offline software pages, <http://atlas-computing.web.cern.ch/atlas-computing/computing.php>
- [55] T Bold, Trigger Menu: default\_14.2.20, [http://tbold.web.cern.ch/tbold//view\\_menu.php?name=default\\_14.2.20](http://tbold.web.cern.ch/tbold//view_menu.php?name=default_14.2.20)
- [56] C. S. Ríos, P. C. Muíno, B. Vachon, Overview and Performance Studies of Jet Identification in the ATLAS Trigger System, 2008
- [57] B.Alver, M.Baker, C.Loizides, P.Steinberg, The PHOBOS Glauber Monte Carlo, arXiv:0805.4411v1, 2008
- [58] M. Spousta, private discussion
- [59] ATLAS Collaboration: TriggerGlossary, <https://twiki.cern.ch/twiki/bin/view/Atlas/TriggerGlossary>
- [60] ATLAS Collaboration: HLT Steering - guide for algorithm developers, <https://twiki.cern.ch/twiki/bin/view/Atlas/MigratingToNewSteering>
- [61] A. Ajitanand, A. Angerami, M.D. Baker, S. Bathe, P. Chung, B. Cole, R. Debye, N. Grau, J. Hill, J. Jia, W. Holzmann, R. Lacey, A. Lebedev, M. Rosati, P. Steinberg, F. Videbaek, S. White, Heavy Ion Physics with the ATLAS Detector, 2008

# Appendix A

This Appendix contains kinematic variables and definitions which are fundamental to heavy ion physics. The coordinate system is centered around the collision point with z axis in a beam direction. In whole high energy physics is useful to use variables that transform simply when changing the reference frame. Particles are characterized by four-momentum

$$P^\mu = (E, \vec{p}) \quad (1)$$

whose square gives invariant mass

$$P^2 = E^2 - \vec{p} \cdot \vec{p} \quad (2)$$

Very often used variables are Mandelstam invariants, like  $s$ ;  $\sqrt{s}$  determines center of mass energy

$$\sqrt{s} = \sqrt{P_1^2 + P_2^2} \quad (3)$$

We need only transformation along beam axis it is useful to define transverse momentum  $p_T$  and longitudinal momentum  $p_{||}$

$$p_T = \sqrt{p_x^2 + p_y^2}, \quad (4)$$

$$p_{||} = p_z, \quad (5)$$

or if we use polar angle (see Fig. 1) we can rewrite formulas for  $p_T$  and  $p_{||}$  as

$$p_T = p \sin \vartheta, \quad (6)$$

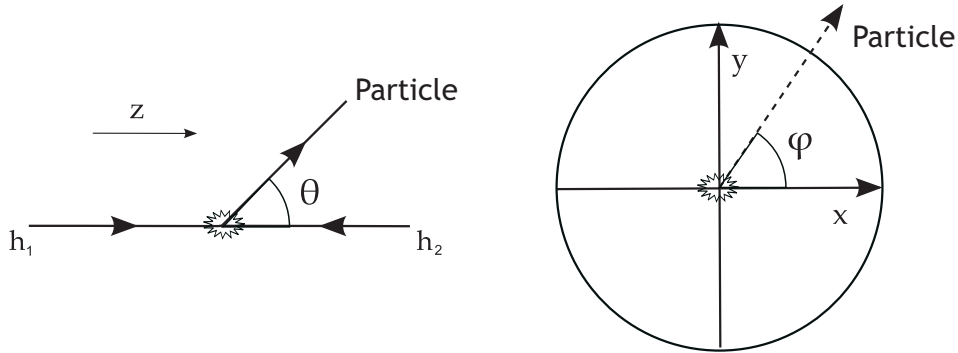


Figure 1: Illustration of a coordinate system

$$p_{\parallel} = p \cos \vartheta \quad (7)$$

and transformation along z axis is then given by

$$\begin{pmatrix} E^* \\ p_{\parallel}^* \\ p_T^* \end{pmatrix} = \begin{pmatrix} \gamma_f & -\gamma_f \beta_f & 0 \\ -\gamma_f \beta_f & \gamma_f & 0 \\ 0 & 0 & 1 \end{pmatrix} \begin{pmatrix} E \\ p_{\parallel} \\ p_T \end{pmatrix} \quad (8)$$

where  $\gamma$  is Lorentz factor defined as

$$\gamma_f = (1 - \beta_f^2)^{-1/2} \text{ or} \quad (9)$$

$$\gamma_f = \frac{E_f}{m}, \quad (10)$$

where  $m$  is invariant mass of system and  $E_f = \sum E_i$  (summation is over all particles in the system).  $\beta$  is particle velocity that can be defined as

$$\vec{\beta}_f = \frac{\vec{p}_f}{E_f}, \quad (11)$$

where  $\vec{p}_f = \sum \vec{p}_i$  and summation is again over all particle in the system.

Similarly the transverse mass is defined as

$$m_T = \sqrt{m^2 + p_T^2}. \quad (12)$$

Transverse momentum  $p_T$  is invariant under Lorentz transformation while longitudinal momentum  $p_{\parallel}$  not. Thus instead using longitudinal momentum  $p_{\parallel}$  it is common to use variable rapidity  $y$  defined as

$$y = \frac{1}{2} \ln \left( \frac{E + p_z}{E - p_z} \right) = \frac{1}{2} \ln \left( \frac{1 + \beta}{1 - \beta} \right) \quad (13)$$

The rapidity is transformed under a boost along x axis from central mass system (CMS) to laboratory system (LAB) (see Fig. 2) as

$$y = y^* + \tanh^{-1} \beta_{CMS} \quad (14)$$

Now the four-momentum of a particle can be rewritten in terms of transverse momentum  $p_T$ , rapidity  $y$ , transverse mass  $m_T$  an azimuthal angle  $\phi$  as

$$E = m_T \cosh y \quad (15)$$

$$p_x = p_T \cos \phi \quad (16)$$

$$p_y = p_T \sin \phi \quad (17)$$

$$p_z = m_T \sinh y \quad (18)$$

Next, we defined pseudorapidity  $\eta$  which is very useful because it depends only on the polar angle  $\vartheta$ :

$$\eta = -\ln [\tan (\theta/2)]. \quad (19)$$

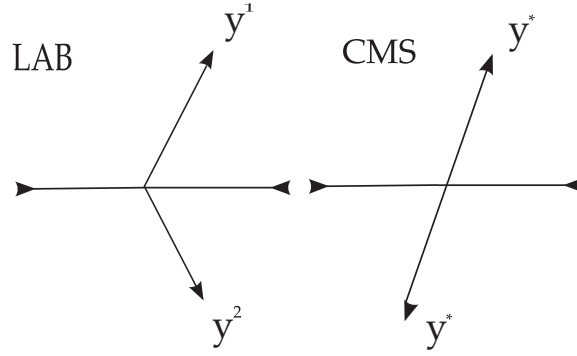


Figure 2: CMS and LAB system. This collision represents an example of fix-target experiment.

For this reason it is easier to use the pseudorapidity than the rapidity or polar angle. In the limit  $|p| \gg m$  rapidity equals the pseudorapidity:

$$y \xrightarrow{|p| \gg m} \eta = \frac{1}{2} \ln \left( \frac{p + p_z}{p - p_z} \right) = \frac{1}{2} \ln \left( \frac{1 + \cos \theta}{1 - \cos \theta} \right) = -\ln [\tan (\theta/2)]. \quad (20)$$

# Appendix B

This Appendix contains calorimeter part of L1 trigger thresholds available for p+p run.

- 4 total Et threshold available: 150, 250, 360, 650 GeV
- 8 threshold for JET RoIs (for 4x4, 6x6 and 8x8 tower cluster ): 5, 10, 18, 23, 35, 42, 70, 120 GeV
- 4 threshold for Front JET RoIs: 18, 35, 70, 120 GeV
- 8 threshold for EM RoIs (1x2 tower cluster ): 3, 7, 13, 13<sup>I</sup>, 18, 18I, 23I, 100 GeV
- 8 threshold for TAU RoIs (1x2 tower cluster ): 5, 6, 9I, 11I, 16I, 25, 25I, 40 GeV
- 8 threshold for Missing Et : 15, 25, 30, 40, 50, 70, 80 GeV
- 4 threshold for total energy from jets: 120, 220, 280, 340 GeV

For more precise information see [55].

---

<sup>1</sup>I means isolation

# Appendix C

This Appendix contains an complete overview of histograms monitoring L2 jet algorithm. Plots presented in this appendix were obtained by reconstruction  $\sim 2000$  minimum bias events in ATHENA version 15.5.3.

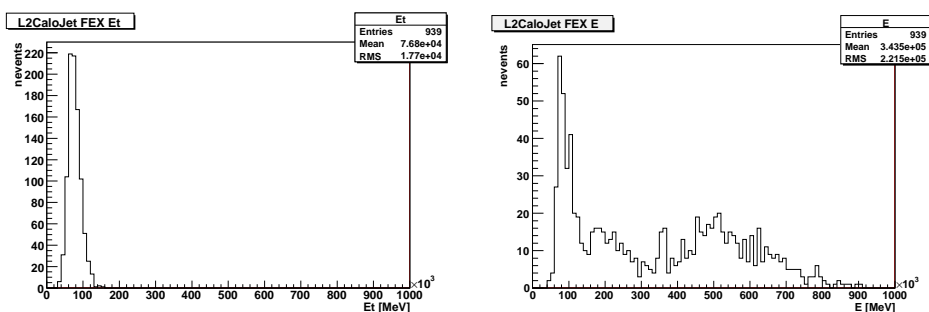


Figure 3: *Left*: Jet transverse energy distribution. *Right*: Jet energy distribution.

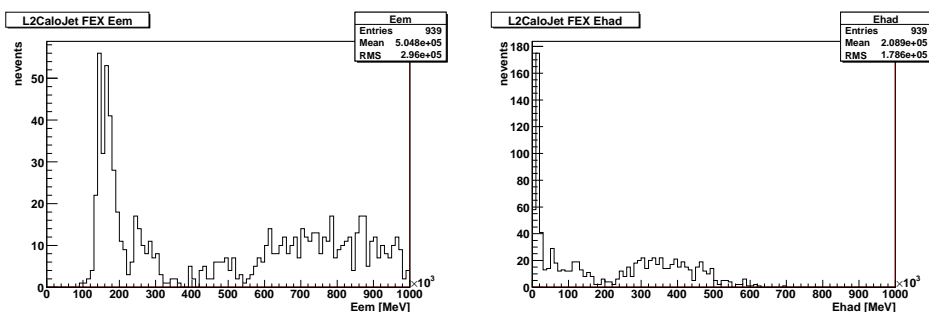


Figure 4: *Left*: Distribution of jet energy in hadronic calorimeter. *Right*: Distribution of jet energy in electromagnetic calorimeter.

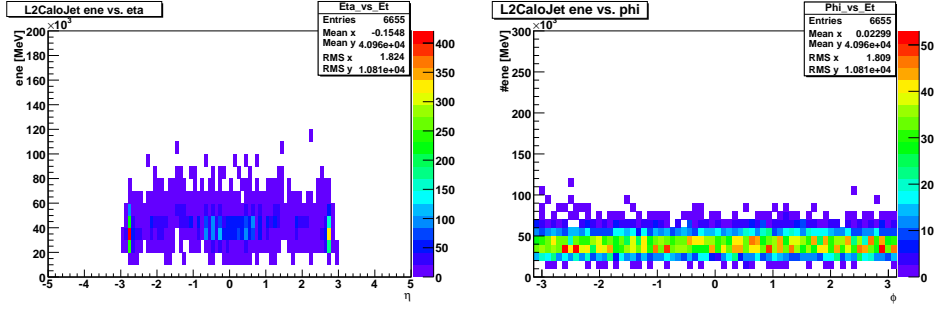


Figure 5: *Left*: Jet transverse energy versus  $\eta$  distribution. *Right*: Jet transverse energy versus  $\phi$  distribution.

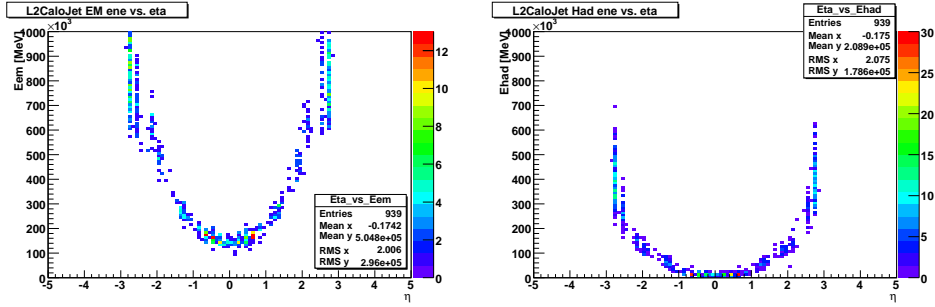


Figure 6: *Left*: Jet energy in hadronic calorimeter versus  $\eta$  distribution. *Right*: Jet energy in electromagnetic calorimeter versus  $\eta$  distribution.

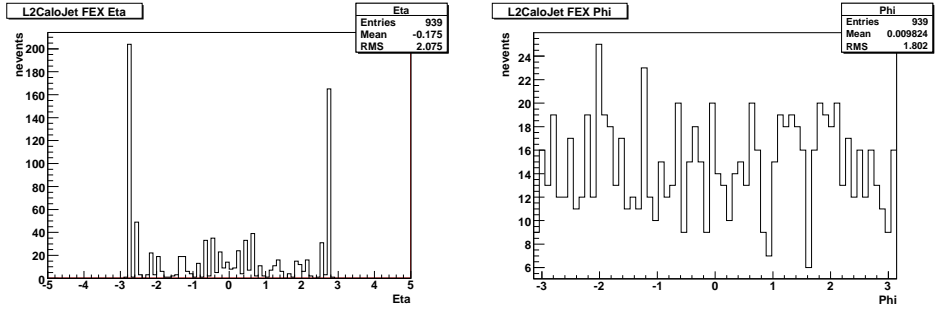


Figure 7: *Left*: Jet  $\eta$  distribution. *Right*: Jet  $\phi$  distribution.

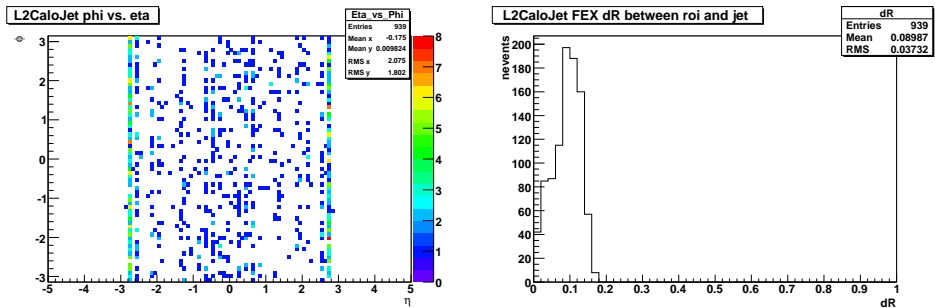


Figure 8: *Left*: Jet  $\eta$  versus  $\phi$  distribution. *Right*: Distance  $dR$  between L1 JET RoI and L2 jet.

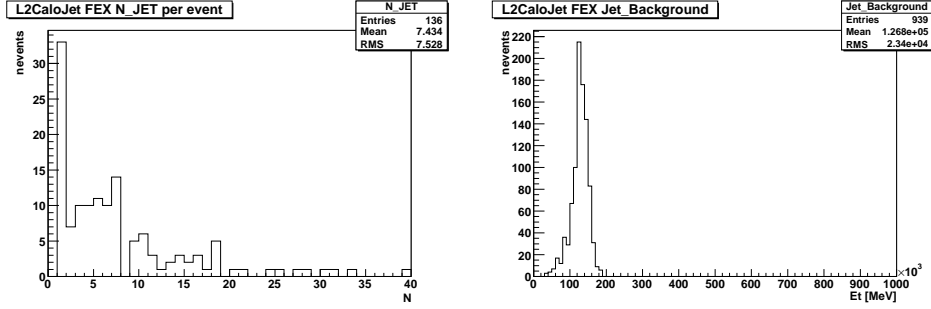


Figure 9: *Left*: Distribution of number of jets. *Right*: Transverse energy distribution of subtracted background.

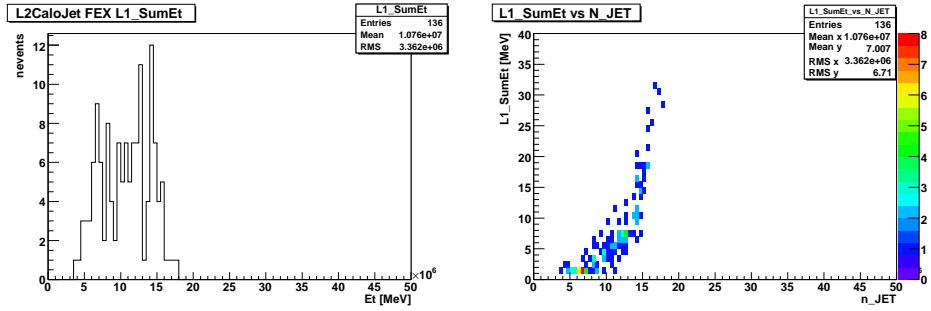


Figure 10: *Left*: Total  $E_T$  sum distribution. *Right*: Total  $E_T$  sum versus number of jets distribution.

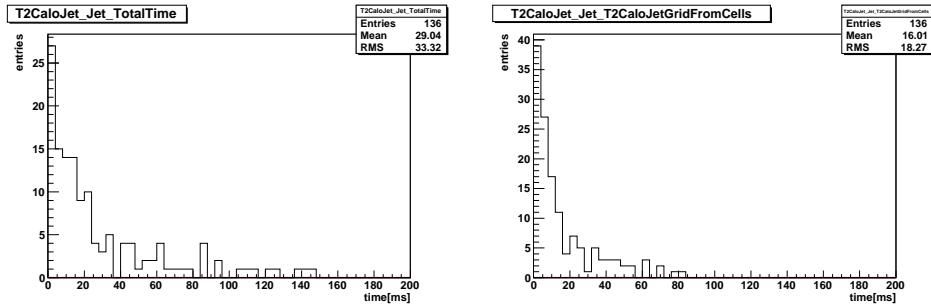


Figure 11: *Left*: Total processing time for the L2 jet algorithm. *Right*: Unpacking time (cell based method) for the L2 jet algorithm.

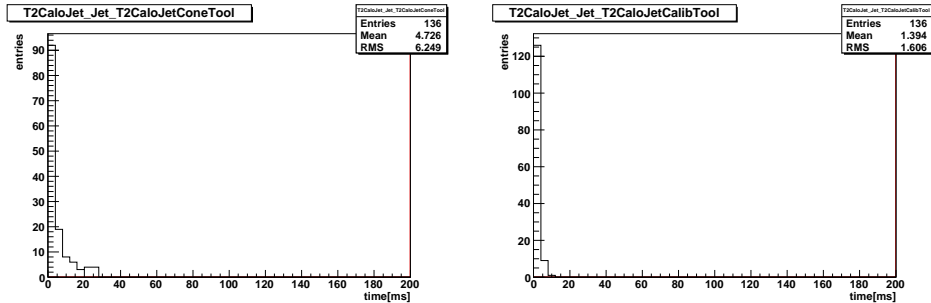


Figure 12: *Left*: Cone tool timing for the L2 jet algorithm. *Right*: Calibration tool timing for the L2 jet algorithm.

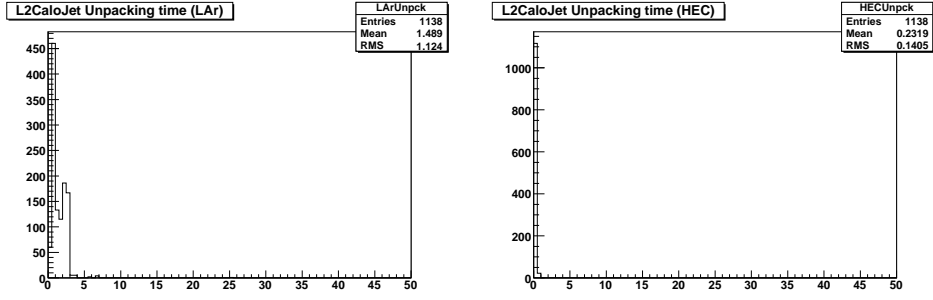


Figure 13: *Left*: Unpacking time (cell based method) of electromagnetic calorimeter for the L2 jet algorithm. *Right*: Unpacking time (cell based method) of hadronic calorimeter for the L2 jet algorithm.

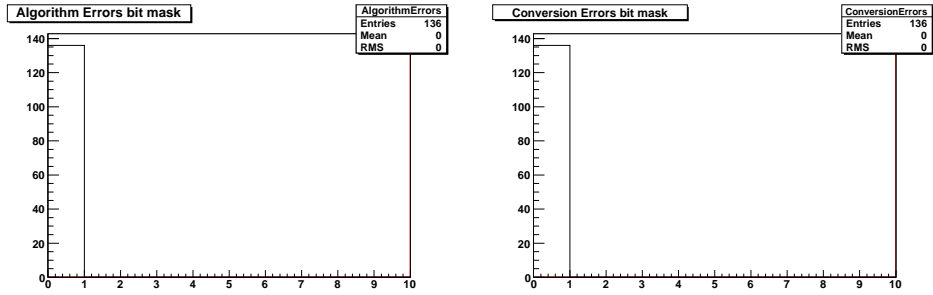


Figure 14: *Left*: Algorithm errors. *Right*: Conversion errors

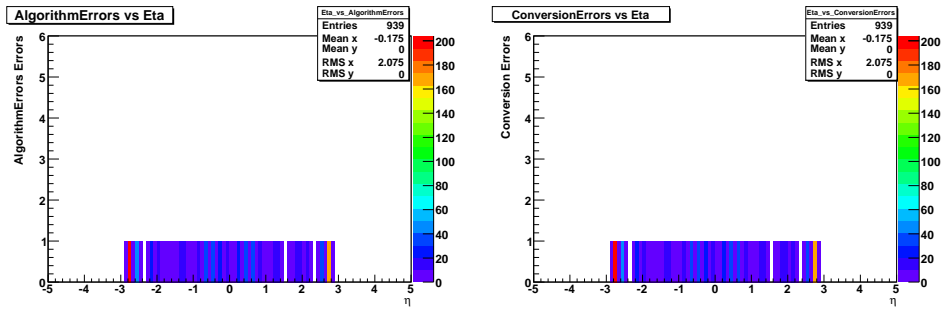


Figure 15: *Left*: Algorithm errors versus  $\eta$ . *Right*: Conversion errors versus  $\eta$ .

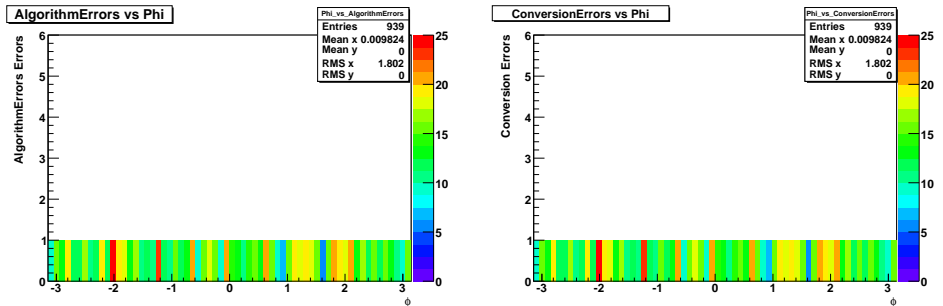


Figure 16: *Left*: Algorithm errors versus  $\phi$ . *Right*: Conversion errors versus  $\phi$ .